Ricardo Miguel Caixa Mineiro

Desenvolvimento de compósitos de PcBN através da Sinterização Assistida por Campo Elétrico

Development of PcBN composites by Spark Plasma Sintering

Universidade de Aveiro
2022

Ricardo Miguel Caixa Mineiro

Desenvolvimento de compositos de PcBN através da Sinterização Assistida por Campo Eletrico

Development of PcBN composites by Spark Plasma Sintering technique

Tese apresentada à Universidade de Aveiro para cumprimento dos requisitos necessários à obtenção do grau de Mestre em Engenharia de Materiais, realizada sob a orientação científica da Doutora Ana Maria de Oliveira e Rocha Senos, professora associada do Departamento de Engenharia de Materiais e Cerâmica da Universidade de Aveiro, a coorientação do Doutor Eduardo Luís Trindade da Silva, professor adjunto da Escola Superior Aveiro Norte e a supervisão da Doutora Cristina Maria da Silva Fernandes, responsável de desenvolvimento de materiais da empresa Palbit S.A.

o júri

Presidente   Filipe José Alves de Oliveira
Investigador Principal do Departamento de Engenharia de Materiais e Cerâmica, Universidade de Aveiro

Vogais   Maria do Rosário Teixeira Soares
Técnico Superior do Laboratório Central de Análises, Universidade de Aveiro

Ana Maria de Oliveira e Rocha Senos
professor Associado do Departamento de Engenharia de Materiais e Cerâmica, Universidade de Aveiro

| **palavras-chave** | Sinterização por Aplicação de Campo Elétrico, Nitreto de Boro cúbico policristalino (PcBN), compósito de cBN-TiCN, Niquel |

Resumo

O PcBN ("*Polycrystalline cubic Boron Nitride*") é um material densificado por técnicas HPHT e possui um elevado custo económico. Neste trabalho pretendeu-se estudar o comportamento durante a sinterização de cBN-TiCN-Ni e a possibilidade de densificação pela técnica de Sinterização Assistida por Campo Elétrico (SPS – "*Spark Plasma Sintering*", disponibilidade do equipamento por parte do Instituto de Cerâmica e Vidro – ICV). Adicionalmente, também foi estudada a dispersão dos constituintes por duas técnicas diferentes: moagem com corpos moentes e processamento coloidal.

Com este propósito foram utilizados dois tipos de pós de cBN: um pó de cBN com tamanho de partícula de 57 µm (D_{50}) e revestimento de Ti_2N, e outro com tamanho de partícula de 1,5 µm (D_{50}) e sem revestimento. Para cada pó foram preparadas 2 composições com TiCN e variado a incorporação de 5% volume de Ni de modo a ver o seu efeito durante a sinterização do compósito.

Foi também implementada a utilização de ferramentas termodinâmicas, nomeadamente o software Thermocalc, para prever quais as fases obtidas para o compósito e assim ajustar este de modo a se tentar obter propriedades mais interessantes para a aplicação pretendida.

As amostras sinterizadas foram caraterizadas estruturalmente por Difração de Raios-X (DRX) e por Espectroscopia de Raman, microstruturalmente por Microscopia Eletrónica de Varrimento (SEM), quimicamente por Espectroscopia Dispersiva de Energia Raio-X (EDS) e fisicamente pelo princípio de Arquimedes.

Para estes sistemas, observou-se que a adição de Ni aumentou a densificação do compósito ("*Liquid Phase Sintering*") e que este possui reatividade com o Ni tendo levado à formação da fase Ni_3B. A transformação de fase do BN de cubico para hexagonal ocorreu durante todo o intervalo de temperatura de 1400 – 2000 °C, tendo sido completa aos 1700 °C para um tamanho de partícula mais grosseira (57 µm) enquanto ainda se verifica fase cubica aos 1800 °C para um tamanho de partícula mais fina (1,2 µm) embora em reduzidas quantidades. Para a composição com o cBN grosseiro revestido (69% volume) só foi alcançada uma porosidade aberta de 0% aos 1700 °C, onde a expansão volúmica do BN devido à transformação de fase favoreceu a remoção da porosidade. Para a composição com o cBN mais fino (50% volume) também se verificou 0% de porosidade aberta, mas também uma extensa transformação de fase do BN. Verificou-se que o cBN mais fino não tem tendência a aglomerar para pH entre 2- 12 e que o uso de dispersante (PEI) é eficaz a 0,5% (% m/m) tanto para a forma "*Short*" como para a "*Long*". Nas condições utilizadas, quer a moagem por corpos moentes quer o processamento coloidal não foram capazes de alcançar uma boa homogeneização, resultando em uma microestrutura com vários defeitos.

keywords   Spark Plasma Sintering, Polycrystaline cubic Boron Nitride (PcBN), cBN-TiCN composites, Nickel

abstract   PcBN (Polycrystalline cubic Boron Nitride) is a material densified by HPHT techniques and processes a high economic cost. In this work it was intended to study the behavior during sintering of the cBN-TiCN-Ni and the possibility of densification by Spark Plasma Sintering technique (kindly made available by the Institute of Ceramic and Glass – ICV). Additionally, the dispersion of constituents was studies by two mixing techniques: ball milling and colloidal processing.

With this purpose it was used two types of cBN powder: a cBN powder with particle size of 57 µm (D_{50}) and a coating of Ti_2N, and another with particle size of 1,5 µm (D_{50}) without coating. For each powder it was prepared 2 compositions with TiCN and variated the addition of 5% vol. of Ni to see its effect in the sintering of the composite.

Additionally, it was implemented the use of thermodynamic tools, namely Thermocalc, to help predicting the resulting phases for the composite and therefor adjust this one to try to obtain more interesting properties for the desired application.

The sintered samples where structurally characterized by X-Ray Diffraction Technique (XRD) and Raman Spectroscopy, microstructurally characterized by Scanning Electron Microscopy (SEM), chemically characterized by Energy-Dispersive X-ray Spectroscopy (EDS), and physically by the Archimedes principle.

For these systems it was observed that the addition of Ni increased the densification of the composite (Liquid Phase Sintering) and that this one is reactive with BN which led to the formation of Ni_3B phase. The BN phase transformation from cubic to hexagonal occurred during all the sintering temperature range of 1400 – 2000 °C, having completely transformed at 1700 °C for the coarser particles (57 µm) while it was still verified the presence of cubic phase at 1800 °C for a finer particle size (1,2 µm) although in reduced amount. For the composition with the course coated cBN (69% vol.) an open porosity of 0% was only obtained at 1700 °C, where the BN volume expansion from the transformation favoured the removal of porosity. For the composition with the finer cBN (50% vol.) it was also achieved 0% of open porosity but with an expensive BN phase transformation. It was verified that the finer cBN powder does not have a tendency to agglomerate for pH in the 2 – 12 interval and that the use of dispersant (PEI) is effective at 0,5% (%m/m) both for the Short form and Long form. With the mixing conditions used, both the ball milling and the colloidal processing were not capable of achieving a good homogenization, resulting in a microstructure containing several defects.

Index

Figures index

Table index

Chapter 1 - Introduction

Cutting tools materials acquired their modern definition during the industrial revolution in the 19th century and ever since the industry is progressing by the synthesis, development, and production of increasingly harder materials [1]. Initially, the production of cutting tools were all based on carbon steels materials and the discovery of highspeed steels (HSS) initiated a change in the industry. With the development of technology, new materials were introduced for the production of cutting tools, namely carbides and other ceramics, which offered greater hardness [1]. Later, cubic boron nitride and diamond were also developed, with the former being the hardest known material with industrial application [1,2]. Figure 1 depicts a hardness comparison including all previously mentioned materials, showing that metal-based materials have lower hardness and higher toughness than the ceramic-based ones.
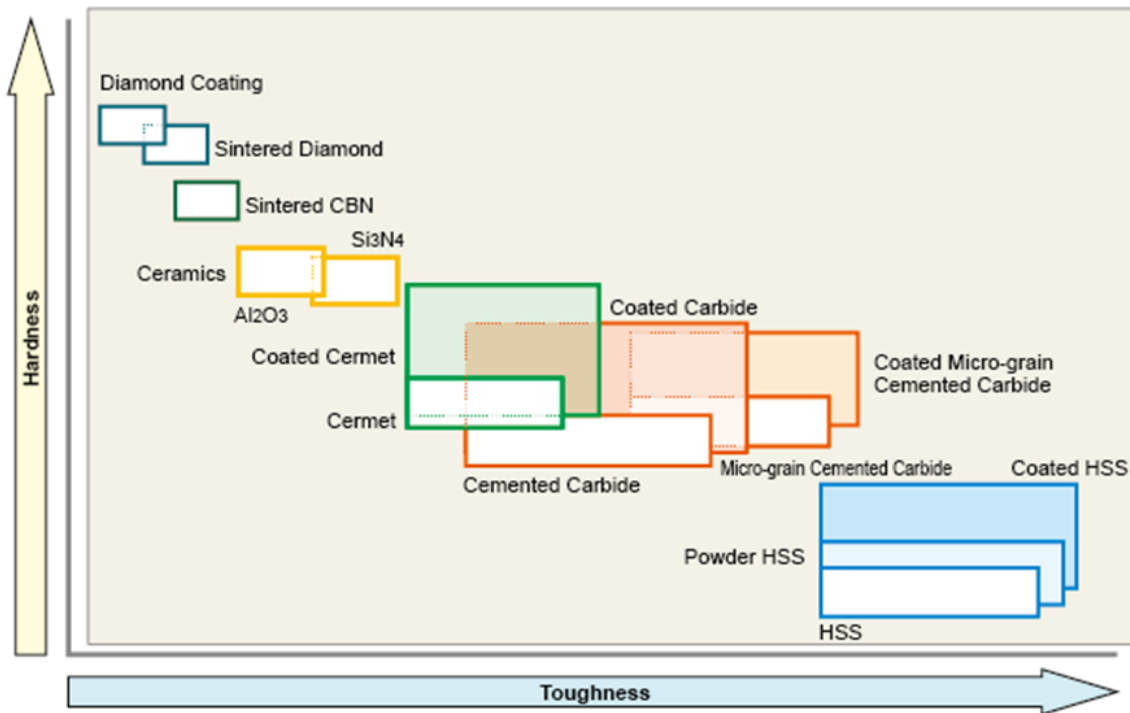
Figure 1- Comparison of hardness vs toughness of the various group materials for cutting tools application [1].

The selection of a cutting tool material for the machining of a specific piece depends on, among other properties, its hardness that should be greater than the piece, and its reactivity. Although diamond is the hardest cutting material, it has limited application towards ferrous alloys due to its thermal instability at temperatures above 600 °C, and chemical instability leading to the formation of carbides with metallic alloys containing Fe, Co, Mg and Ni, among other elements [3–5]. Albeit not as hard, cubic boron nitride (cBN) is also one of the hardest materials, but since it cannot be used by itself in cutting tools due to preferential mechanical cleavage and its sintering being throw impractical intensive conditions, it is produced with metallic and/or ceramic binders to increase its mechanical resistance and densification [4,6–10]. These ones are designated as PcBN (Polycrystalline cubic Boron Nitride).

PcBN cutting tools are classified in two groups according to the volume amount of cBN incorporated: "High cBN" for 70 – 95% with metallic binders; and "Low cBN" for 40 – 70% with mostly ceramic binders [11–13]. These are used in three different forms: "Full PcBN" where all the cutting tool body is made of PcBN; "Full Face PcBN", where the PcBN is cut in thinner parts and brazed on a substrate forming one of the faces of

the cutting tool; and "Tip PcBN" where the PcBN is also cutted in small pieces and brazed on the substrate but just to form the tip of the cutting tool, all three shown in Figure 2 [9,14]. There is also the possibility to coat the PCBN tools with TiN, TiAlN or TiCN in order to decrease the tool wear [9,12,15].

Full PcBN   Full Face PcBN   Tip PcBN

Figure 2- Examples of PcBN cutting tools (from left to right): Full PcBN, Full Face PcBN and Tip PcBN [14].

PcBN is processed by techniques capable of applying high pressure and high temperature (HPHT), due to cBN high covalent bonding which originates low diffusion coefficients for matter transport and is, therefore, a hard-to-densify material. For this reason, high temperatures (1200 – 1500 ºC) and high pressures (4 – 6 GPa) are employed, in order to densify the composite and keep the system in the BN cubic phase stability zone [3,9,16]. But these techniques, besides using intense sintering conditions, have the disadvantages of a reduced amount of material produced for each sintering cycle, and a complex and time-consuming task of mounting the equipment between each sintering step, making PcBN a high processing cost material [17,18].

As an alternative technique for sintering PcBN the use of Spark Plasma Sintering (SPS) has been investigated. This technique applies pressures of up to 100 MPa and utilizes electric fields to generate heating rates up to 1000 ºC/min [19]. This high heating rate allows to significatively decrease the heating time which in turn may help to minimize phenomena like the BN phase transformation from cubic to hexagonal phase, which being a soft phase will drastically decrease the PcBN hardness. Although SPS still has some general drawbacks like limitations in geometry of the piece and a high equipment cost [20], it opens the possibility of a more economically way to process PcBN by applying less extreme temperatures and pressure conditions, together with a shorted sintering time, which should be more investigated.

In this work, the densification of cBN+TiCN+Ni composites processed by SPS will be investigated. The PCBN compositions selected for investigation belong to the category of low cBN (< 70%) with a ceramic binder as matrix (TiCN), plus a Ni binder, and the aims of the work will be focused on studying the thermal reactivity during the SPS process, particularly the phase transformation from cBN to hBN. Additionally, considering the importance of the constituents' homogeneity in the material to be sintered, it will also be investigated the colloidal processing route comparatively to the mechanical mixture of the constituents.

This work was developed in partnership with Palbit S.A., which as an interest in knowing and developing new and improved cutting tools solutions. Were, the focus was in new production techniques and composite materials of PcBN cutting tools, for which already exists machining applications.

Chapter 2- State of the art

2.1 Boron Nitride

Boron nitride is a chemically processed industrial ceramic, produced since the 1950´s [21]. It was discovered for the first time in nature in 2009 in its cubic form as some 50 – 200 nm incrustations in minerals, which are estimated to be formed over 300 km deep inside the earth where pressures are estimated to exceed 10 GPa [22,23]. It possesses various crystallographic structures, being stable or metastable depending on the temperature and pressure conditions which is submitted. The hexagonal and cubic phases are the most used in technical applications [24–26].

2.1.1 Boron nitride polymorphs

BN has four main crystallographic structures: cubic, hexagonal, wurtzitic, and rhombohedral, which occur due to the hybridization of the chemical bound B – N between the sp^2 and sp^3 states [24–28]. The hexagonal (sp^2) and cubic (sp^3) phases are the most thermodynamically stable and well-known, due to their similarity in terms of properties with the two allotropic forms of carbon: graphite and diamond respectively [16,29,30].

Hexagonal boron nitride (also designated as h-BN, α-BN, g-BN and white graphite) was produced for the first time in 1842 and become the first known phase of BN [21,27]. Today it is produced at an industrial scale using boron oxide and a compound containing nitrogen by techniques like solid state reaction [21,31,32]. The crystallographic structure of hBN is similar to graphite, in the sense that the atoms form three covalent bondings (sp^2), constructing B_3N_3 hexagons placed side by side across the plane (also designated polytype 1H), being the positions of B and N atoms alternated across the plane, Figure 3 and Figure 4 [33]. The same alternating succession of atoms occurs between adjacent planes, exhibiting a layer sequence of the AA´AA´ type, differentiating from the AB type of graphite, and are bounded by weak Van der Walls forces, leading to the low hardness of the material (Table 1) , and low friction coefficient [33,34]. The high electronegativity of N brings the valence electrons of the Van der Walls bonding closer to the atom, restraining their movement and leading to low electric conductivity (Table 1) [33]. Being a material with high oxidation resistance, thermal shock resistance and high thermal stability, it is used as refractory material, a high temperature lubricant, as die coating for castings and heat dissipator for electronic components [21,32,35].
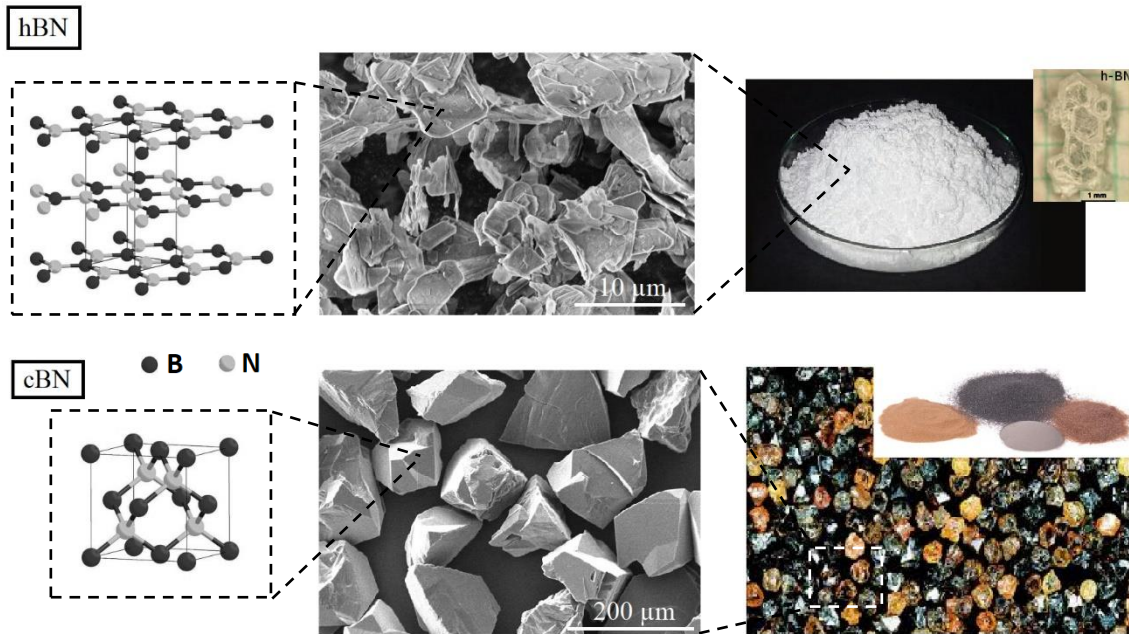
Figure 3- Structural, microstructural, and macroscopic characteristics of BN particles forming the hexagonal and cubic phases [36–38].

Cubic boron nitride (also designated as c-BN, z-BN, β-BN, zinc blend, spharelite and inorganic diamond, and some commercial names such as Borazon, Kubonit, Kiborit, Belbor, Elbor and Amborit) was synthetised for the first time in 1957 from compounds containing boron and nitrogen with application of high pressure and high temperature (HPHT) [3–5,27]. Today it is industrially produced with HPHT techniques by phase transformation from hexagonal to cubic using solvent – catalysts [24,39]. The crystallographic structure of cBN is similar to diamond, where the atoms form 4 covalent chemical bonds (sp^3) rearranging to form a tetrahedron shape and are displaced in the structure in an alternating pattern of B and N, Figure 3 and Figure 4 [33]. Due to all valance electrons participating in the covalent bonding B–N, with a small ionic character because of the electronegativity difference between B and N, there is no available electrons to form weak Van der Walls bonding's leading to the high hardness of this phase, placing it between the hardest known materials with a monocrystal Vickers hardness of 62 GPa (Figure 5), while typically having a Vickers hardness between 40 – 50 GPa for a micrometric grain size polycrystal [33,40]. It is a stable material, starting to oxidize at temperatures of 1000 ºC when exposed to oxygen and chemically reacts with various metals for temperatures over 1000 ºC at various atmospheres [4,7].

Comparing the properties of BN cubic and hexagonal phases (Table 1), they have different densities (3.5 and 2.2 g/cm^3 respectively) due to the crystallographic characteristics of each, and differ in all properties except electrical (high electrical resistivity of 10^{10} $\Omega^{-1}.m^{-1}$) and some degradative ones. Cubic form has much greater mechanical properties that hexagonal from, namely hardness (40 – 50 compared to 0,1 GPa), young modulus (700 – 900 compared to 43 – 47 GPa), bulk modulus (369 – 400 compared to 36 GPa) and compressive strength (4.15 – 5.33 compared to 0,08 – 0.09 GPa). Being the thermal properties of the hexagonal phase strongly dependent on the crystallographic orientation at which they are measured, its thermal expansion coefficient is quite different (-2.72 parallel and 37.7 10^{-6} k^{-1} perpendicular to the crystallographic plane at 25 ºC) from the cubic phase (1.15 10^{-6} k^{-1} at 25 ºC), while having lower thermal conductivity (1.5 – 13 compared to 0.03 – 5.5 W/cm.k at room temperature). In relation

to degradative properties, both phases possess oxidation resistance for temperatures over 1000 ℃ in air, but eventually cBN suffers a phase transformation to hBN at high temperature while hBN has stability in vacuum (> 4000 ℃) or inert atmospheres (2850 ℃) even at very high temperatures. Cubic BN shows to possess reactivity with metals for temperatures above 1000 ℃.

The other two crystallographic phases of BN: rhombohedral and wurtzite, are considered metastable phases [16]. Due to its difficulty to produce in a pure state or obtain grain sizes with large enough dimensions to be experimentally measured, most of their properties are unknown or usually determined by calculations with mathematical models [24,41,42]. Considering their characteristics, hBN and rBN are usually described as low-density, low hardness polymorphs with a bidimensional (2D) crystallographic structure, while cBN and wBN are high density and high hardness polymorphs with a tridimensional (3D) crystallographic structure, Figure 4 and Table 1 [33].
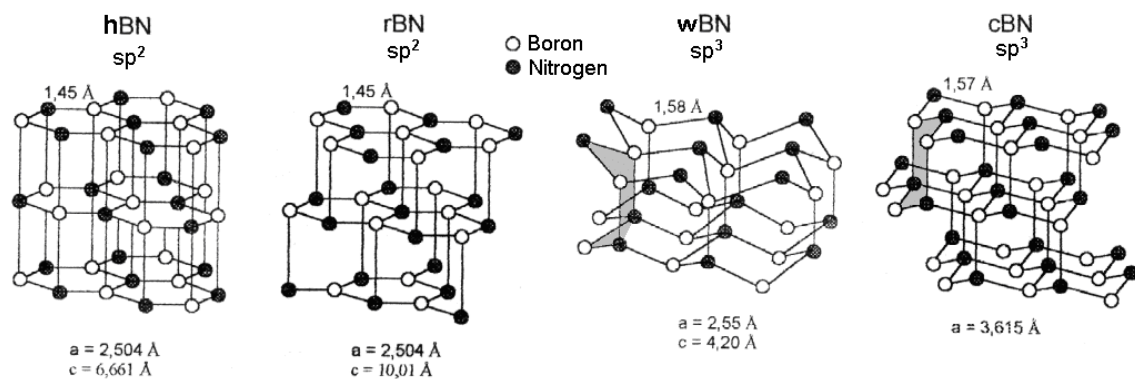
Figure 4- Comparison between the crystallographic structures of the 4 main polymorphs of BN [33].

Besides the already mentioned ones, other less common crystallographic phases of BN are known to exist: turbostratic BN, pyrolytic BN and amorphous BN, being these ones more characteristic of the techniques used to obtained them, such as Chemical Vapor Deposition at High Temperature, or its physical form such as films and coatings [33,41,43–46]. Some theoretical phases such as monoclinic BN and orthorhombic BN are also predicted to exist [47–50].

Table 1- Crystallographic characteristics and properties of the 4 polymorphs of BN: rhombohedral, hexagonal, cubic and wurtzite [3,4,8,24,27,33,35,51].

Material	rBN	hBN	cBN	wBN
Crystallographic characteristics				
Crystallographic group	R3m	$P6_3/mmc$	$F\bar{4}3m$	$P6_3mc$
Hybridization state	Sp^2	Sp^2	Sp^3	Sp^3
Energy bond (eV) covalent Van der Walls	3.25 0.052	3.25 0.052	1.52 -	1.52 -
Minimum interatomic distance of covalent bond (Å)	1.4500	1.4457	1.5670	1.5760
Coordination number (Z)	3	3	4	4
Unit cell parameters (Å) a c	2.504 10.010	2.504 6.661	3.615 -	2.550 4.230
Interplanar distance (d_{002})	3.34	3.3306	-	2.20
Density (g/cm^3)	2.29	2.29	3.51	3.50
Mechanical properties				
Hardness Mohs scale HV (GPa)		1.5 0.131	9.5 - 10 40 - 50	10
Young modulus (GPa)		43 - 47	700 - 900	
Bulk modulus (GPa)	33	36.5	369 - 400	370 - 400
Compressive strength (GPa)		∥ 0,081 ⊥ 0,096	4.15 - 5.33	
Thermal properties				
Thermal conductivity (W/cm.k) 25 ºC. calculated 25 ºC		∥ 5.5 ⊥ 0.03	13 1.5 - 13	
Thermal expansion coefficient (10^{-6} k^{-1}) 25 ºC 20 – 300 ºC 900 ºC		∥ -2.72 ⊥ 37.7 ∥ 2.0 ⊥ 4.1	1.15 5.60	∥ 2.7 ⊥ 2.3
Electrical properties				
Resistivity (Ω.m)		∥ 10^{10} - 10^{14} ⊥ 10^{10} - 10^{14}	10^{10}	
Degradative properties				
Oxidation resistance air		> 1000 ºC	> 1000 ºC	
Decomposition (normal pressure) air vacuum inert atmosphere		> 1000 ºC > 4000 ºC 2850 ºC	> 1000 ºC*	
Chemical reaction with metals (air. vacuum)			> 1000 ºC	

*Occurs phase transformation to hBN
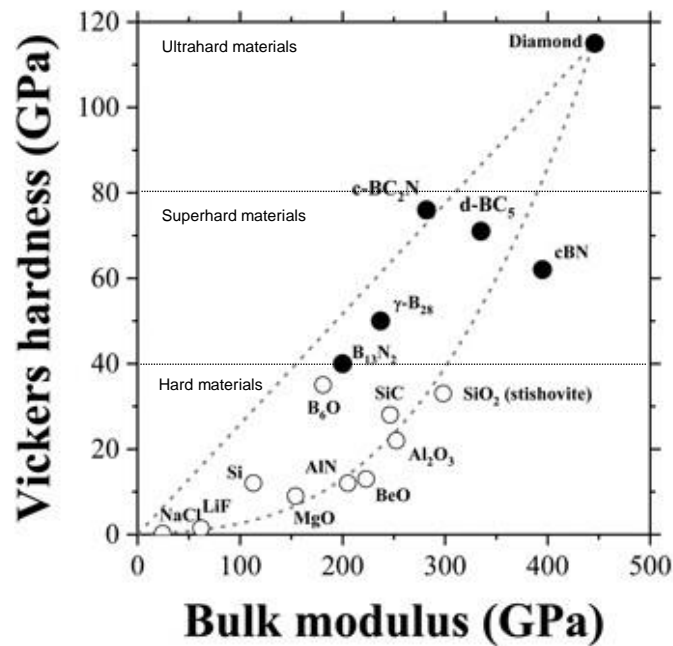
Figure 5- Vickers Hardness (HV) vs bulk modulus (B_0) of various materials. Materials marked with black belong to the B-N-C-O system; dashed lines are visual indicators of the relations HV~B_0 and HV~B_0^3 [2]. The cBN hardness shown corresponds to a monocrystal [52].

Since the discovery of a second form of BN in 1957, there was interest in drawing its phase diagram [16,53]. Between 1963 and 2000 the phase diagram was progressively redrawn based on experimental results of the phase transformations, analogies to the carbon phase diagram, and later by thermodynamic calculations based on experimental measurements [16,54,55]. From the most recent one in 1999 comes the thermodynamically stable phase diagram of BN, mostly accepted today, despite some recalculations in 2000 to account for the uncertainties arrived from the experimental part [16,56]. An increase in studies occurred in the beginning of the years 1990´s were the stability of phases and the phase diagram of BN were drawn by computational calculations (a scientific area called Computational Chemistry [57]) [36,47]. At the present time, no definitive answer can be given about the stable phase at room P-T conditions and the right position of the hBN → hBN phase line, since these results greatly depend on the physical model used and often lead to contradictory results [36,47]. For this reason, cBN is the phase considered stable at normal P-T conditions [47,55]

The phase diagram of Figure 6 shows the stable phases and physical states of BN in function of the temperature (1000 – 4000 K) and pressure (10^0 – 10^{10} Pa). The stable phase at room pressure and temperature is cubic, and the phase transformation to hexagonal occurs at 1615 $\pm$15 K (1342 $\pm$15 ºC) [16]. This was later recalculated to 1593 $\pm$380 K (1320 $\pm$380 ºC) [56].

Even though the phase diagram indicates that hBN is a high temperature phase, it exists at room pressure and temperature conditions [18,32]. When cBN is heated up to the hexagonal stability zone (P < 1GPa) it transforms to hBN, but when cooled down to the cubic phase stability zone the BN remains in the hexagonal form (room P-T conditions). This can be explained by the transformation mechanisms that occur in the material: the application of pressure (static or dynamic) forces the physical approximation of the BN stacking layers, promoting diffusionless mechanisms and leading to the phase

transformation (i. e. hBN → wBN). Regarding temperature, the supply of energy to the system allows the action of diffusion mechanisms that cause the phase transformation (i. e. wBN → hBN, cBN → hBN, rBN → hBN) [58]. For the case of hBN → cBN transformation, both temperature and pressure are necessary to allow the phase transformation since both a physical and an energetical barrier are needed to be overcome to allow the transformation between these two phases [54,59]. Additionally, it was concluded that the hBN ↔ cBN phase transformation occur as a direct transformation, indirect transformation through one of the metastable phases, or through an unknown phase depending on external factors (i. e. catalysts) [28,60,61].

.
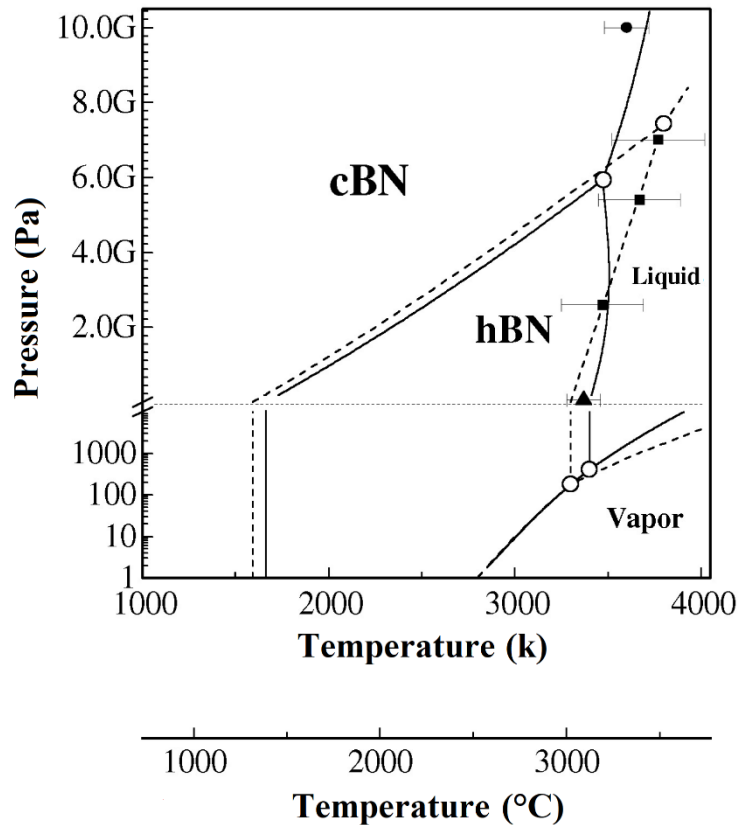
Figure 6- Most recent and accepted thermodynamically stable phase diagram of boron nitride [62] (dashed lines – phase diagram of 1988 [63]; solid line – refined phase diagram of 1999 [16]; black squares represent the fusion temperature of hBN according to Wentorf [64], black triangle represent the fusion temperature of hBN at 50 MPa [65], black circle represents the fusion temperature of cBN at 10 GPa [66], white circles represent the triple points positions.

It is experimentally verified that the phase transformations of BN are strongly influenced by a wide variety of reasons, namely, the material processing (time, temperature, pressure), and the material intrinsic (number of defects, grain size) or extrinsic characteristics (binders – retardants or accelerators – catalysts and impurities like H_2O, B_2O_3 and O_2) [27,28,51,54,59,67–70].

2.2 PcBN compositions for cutting tools

The sintering of cBN without binders (also known as binderless PcBN or BcBN [71]) is only achieved by using HPHT techniques and conditions usually above 7 GPa and 1500 – 2600 ºC, due to the low atomic diffusion coefficients caused by the high energy bonding of B–N, and to maintain the conditions on the cubic phase stability zone [6,17,72,73]. The sintering is predicted to occur in the solid state, since the conditions are much lower than the BN fusion temperature of +3000 K (Figure 6). To be more feasible, materials that act like binders were introduced to decrease the severity of the conditions and facilitate its processability, forming ceramic, metallic or cermet (metal + ceramic) matrixes [7].

2.2.1 High and Low PcBN

Despite having other characteristics (i. e. particle size, particle shape, binders), PcBN tools are broadly classified as High or Low PcBN based on the volume amount of cBN incorporated, as was indicated in the Introductory section. High PcBN (> 70 vol% cBN) possesses higher mechanical and thermal shock resistance, which makes them more indicated for interrupted machining, whether roughing or finishing of cast irons. Low PcBN has higher amount of binder which allows a greater control of the tool's properties, depending on the type of incorporated binders, and is more indicated for continuous machining to achieve a finishing cut of hardened steels, cast irons and superalloys [4, 9]. Together, PcBN cutting tools are used for the machining of a great variety of materials, such as steels, stainless steels, hardened steels, cast irons, high temperature alloys, and nonferrous materials such as aluminium and copper alloys.

To produce PcBN, any element of groups 4, 5 or 6 of periodic table, or ceramic compounds containing these elements (carbides, nitrides, borides, or silicides) can be used to form a matrix, being also used Al, Co, Ni, Be, Re, Mn, Cu or ceramic compounds containing these elements such as Al_2O_3 and BeO [3,74]. Some properties of some of these elements/compounds are shown in Table 2.

Table 2- Properties of some commonly used material as binders to produce PcBN [3,75,76].

Material	Ti	Al	TiN	TiC	TiB_2	AlN	AlB_2	Al_2O_3
Crystalline structure	Hexagonal	cubic	cubic	cubic	Hexagonal	Hexagonal	Hexagonal	Hexagonal
Density (g/cm³)	4.51	2.70	5.22 – 5.44	4.92	4.52	3.26	3.19	3.96
Melting point (ºC)	1670	660	2930	3065	3197	2300	> 920 decomposes	2050
Young modulus (GPa)	106	69	370	450	435 - 540	318	-	427
Thermal expansion coefficient (10^{-6} k^{-1})	8.4	23	8	8.6	8.1	3.9	-	8.1
Thermal conductivity (W/cm.k)	0.17	2.03	0.25	0.33 – 0.43	0.8	2	-	0.14

The use of metallic elements has the purpose of taking advantage of the lower melting point of metals, compared to cBN, allowing the formation of a liquid phase which fills the voids between cBN particles and making possible the densification at lower temperatures and pressures [77]. These metallic binders also increases the toughness of the material, at the expense of lower hardness in comparison to ceramic matrixes. Simultaneously, there is a tendency of cBN to react with metals forming borides and nitrides such as TiB_2, AlN, AlB_2, and WB_2, as shown in Figure 7 [3,9,77,78]. Particularly, Ti, Al, or compounds containing these elements are the most commonly used binders

for sintering PcBN, due to the capability of reacting chemically with BN. They also form compounds (AlN, TiB_2 and TiN) that have high mechanical resistance and hardness [18,77]. Additionally, Al is also used as an oxygen capturer by forming Al_2O_3 [79].
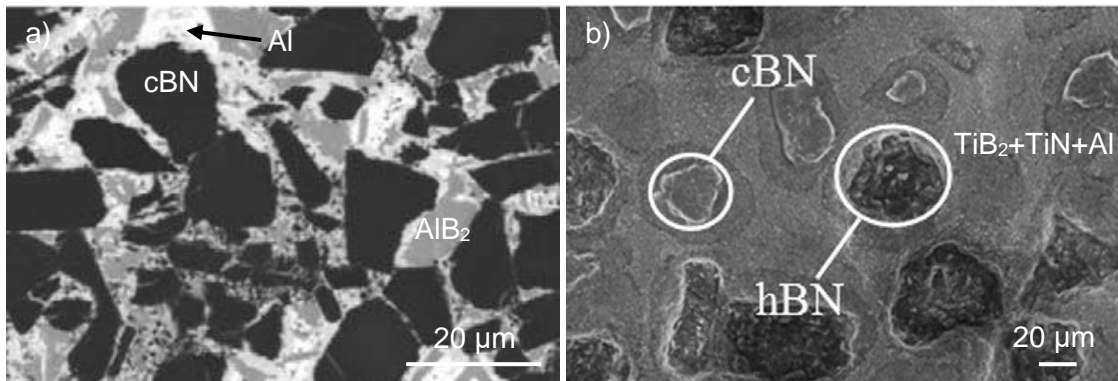
Figure 7- Sintered PcBN microstructures containing metallic phases: (a) 75% cBN + 25% Al and (b) 45% cBN + 35% Ti + 20% Al, all in volume % [18,80].

Conversely, ceramic matrixes in PcBN lead to greater hardness, as well as wear and oxidation resistance, in comparison to metal binders, at the expense of toughness [77]. Being more refractory than metals, ceramics enable less formation of reaction phases and sintering occurs in a solid state (Figure 8). The most commonly used ceramic components are TiC, TiN and TiCN [81].
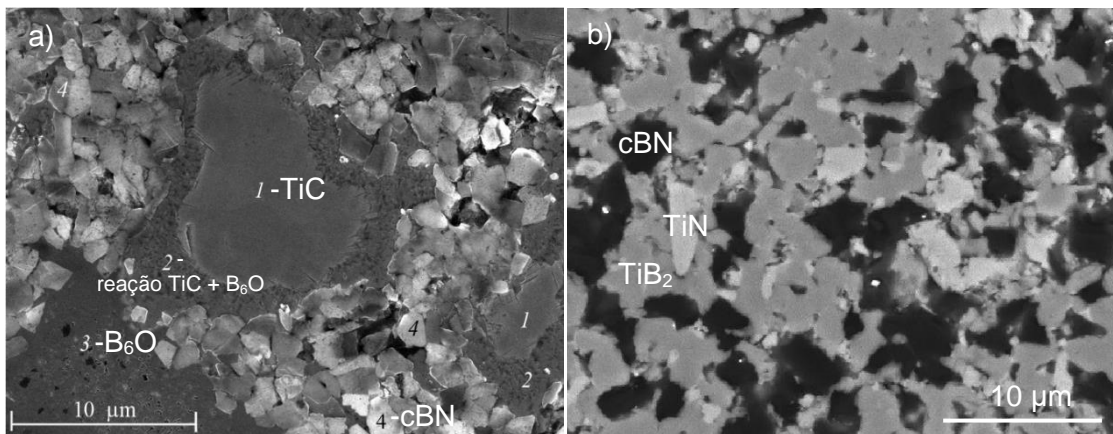
Figure 8- Sintered PcBN microstructures containing ceramic phases: (a) 60% cBN + 20% B_6O + 20% TiC and (b) 30% cBN + 42% TiB_2 + 18% TiN, all in volume % [82,83].

Another possibility is to use both metallic and ceramic binders simultaneously in the cermet matrix to try the attainment of the best properties of each type of matrix with compensation of the individual disadvantages (Figure 9) [77].
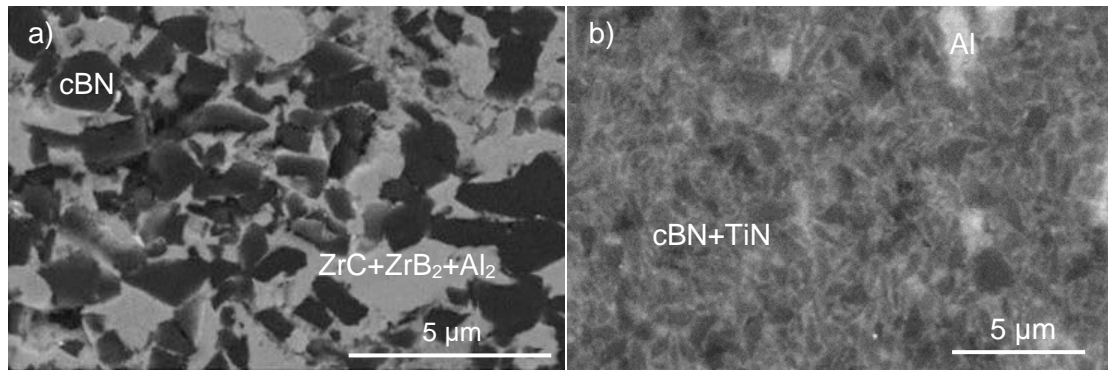
Figure 9- Sintered PcBN microstructures containing metallic and ceramic phases: (a) 60% cBN + 35% ZrC + 5% Al and (b) 74% cBN (coated with 10% TiN) + 16% Al, all in volume % [81,84].

Additionally, the binders have an accelerator/retardant effect in the temperature at which the transformation from cubic to hexagonal phase starts to occur (T_{cBN}). Not being a transformation that immediately occurs when a specific threshold of temperature is reached, it can prolong for long periods of time [85]. The temperature at which hBN starts to form was experimentally observed (Figure 10), and determined that WC-Co, Al_2O_3-Ni and Al_2O_3 worked as accelerators, with the latter having a smaller effect. While TiN did not show any effect, for SiAlON, mullite and SiO_2 was observed a retardant effect, with the former having a smaller effect [70].
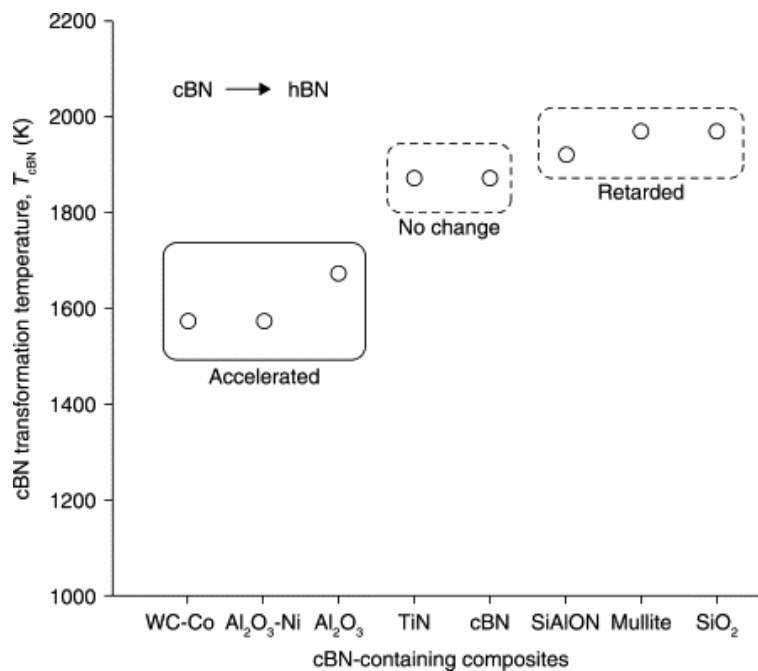
Figure 10- Effect of various materials in the transformation temperature of BN from cubic to hexagonal phase [70].

2.2.2 PcBN by High Pressure High Temperature techniques

Using HPHT techniques it is possible to sinter PcBN by applying pressures of 4 – 6 GPa and temperatures of 1200 – 1500 ºC, making use of intense pressures to

prevent the h-BN phase transformation and achieving high densification values [3]. The HPHT compositions presented in Table 3 belong, with the exception of one composition, to High PcBN category (cBN>70 vol%), were metallic binders are generally used but in some cases ceramic compounds were also added [86]. Yang et al. [87] reported the sintering of PcBN with (59 – 90%) cBN and Ti, Al binders, variated the binders amount. The phases formed after HPHT were, besides cBN, TiN, TiB_2, AlN for cBN >80% and Al_3Ti for cBN <70%. Despite the high densification achieved, a reduced hardness with the decrease of cBN amount was noticed, i. e. 39 HV for 90% cBN and 20 HV for 59% cBN (Table 3). Liqiang et al. [77] has prepared PcBN compositions with (83 – 89%) cBN and AlN, Al, Ni as binders, variating the binders amount and sintering temperature. In all cases it was verified the complete reaction of the metallic phases to form AlB_2, AlNi and AlN compounds (ZrB2 and ZrN phases resulted from contaminations during powders ball milling). High densification values were achieved in all compositions and temperatures (1350 – 1500 ºC), with hardness values between 43 – 48 GPa, reaching a maximum with the second highest cBN amount (87%), sintered at 1500 ºC. Ziling et al. [88] studied the sintering of cBN using Al and Ti_3AlC_2 as binders, variating the sintering temperature (1200 – 1500 ºC). Reaction between phases occurred during the sintering which led to the formation of TiC, AlN, TiB_2, while the Ti_3AlC_2 phase completely disappeared for T > 1300 ºC. It was achieved high densifications for the highest sintering temperatures, and the hardness did not significantly increase for temperatures above 1300 ºC. Huanli et al. [89] has varied the cBN content, between 74 and 79%, and used TiN, Al, Co, TiB_2 as binders. Sintering the compositions resulted in the formation of AlN, AlCo phases, besides the already existing ones and ZrO_2 phase resulting from the milling contamination. Near full densification was observed, and full densification was achieved for the composition containing 76% cBN, while also reaching a hardness of 50 GPa.

Table 3- PcBN compositions, sintering conditions by HPHT, and mechanical properties.

Initial cBN powder	Composition (vol. %)	Sintering conditions	Temperature (ºC)	Final phases	Densification (%)	HV (GPa)	Fracture thoughness (MPa.m$^{-1/2}$)	Bending strength (MPa)	Ref.
cBN (4 – 8 µm)	90% cBN – 4% Ti – 7% Al	5.5 GPa 10 min	1400 ºC	cBN+TiB$_2$+TiN+AlN	96	39	-	~725	[87]
	79% cBN – 7% Ti – 13% Al			cBN+TiB$_2$+TiN+AlN+Ti$_2$AlN	97	35	-	~912	
	74% cBN – 9% Ti – 17% Al			cBN+TiB$_2$+TiN+AlN+Ti$_2$AlN+Al$_3$Ti	97	33	-	~890	
	59% cBN – 14% Ti – 27% Al			cBN+TiB$_2$+TiN+AlN+Al$_3$Ti	96	20	-	~740	
cBN (0.5 – 12 µm)	89% cBN – 7% AlN – 3% Al – 1% Ni	5.5 GPa 90 s	1350	cBN+AlN+AlB$_2$+AlNi+ZrB$_2$^{a}+ZrN^a	97	-	-	~450	[77]
			1500		99	46	6	~540	
	87% cBN – 8% AlN – 3% Al – 1% Ni		1350		97	-	-	~450	
			1500		99	48	6.6	~550	
	85% cBN – 10% AlN – 4% Al – 1% Ni		1350		98	43	5.8	~450	
			1500		99	47	7	~575	
	83% cBN – 11% AlN – 4% Al – 1% Ni		1350		99	-	-	~525	
			1500		99	44	7.2	~640	
cBN (2.5 – 12 µm)	cBN – Al – Ti$_3$AlC$_2$	5.5 GPa 90 s	1200	cBN+TiC+AlN+TiB$_2$+Ti$_3$AlC$_2$	94	41	5.8	~380	[88]
			1300	cBN+TiC+AlN+TiB$_2$+Ti$_3$AlC$_2$	97	47	7.2	~500	
			1350	cBN+TiC+AlN+TiB$_2$	98	47	7.0	~500	
			1500	cBN+TiC+AlN+TiB$_2$	99	48	6.6	~520	
cBN (2.5 – 20 µm)	79% cBN – 7% TiN – 13% Al – 1% Co	5.5 GPa 1550 ºC 90 s	1550	cBN+TiN+AlN+TiB$_2$+AlCo+ZrO$_2$^{a}	98	47	5.9	~600	[89]
	76% cBN – 6% TiN – 13% Al – 1% Co – 4% TiB$_2$				100	50	7.4	~735	
	74% cBN – 6% TiN – 12% Al – 1% Co – 6% TiB$_2$				99	48	7.3	~680	

^{a}Zr contaminations from mixture by ball milling

2.2.3 PcBN by Spark Plasma Sintering technique

PcBN cutting tools with low amount of cBN can be sintered with lower sintering conditions techniques than HPHT ones, such as pressureless sintering (PS), hydrothermal hot pressing (HHP) and hot isostatic pressing (HIP) [70]. Among these, Spark Plasma Sintering (SPS) enables the sintering of PcBN with temperatures up to around 2000 ºC and pressures as high as 100 MPa with a shorter sintering cycle, being commonly used pressures of 50 – 100 MPa and temperatures of 800 – 1900 ºC (table 4). Yang et al. [18] reported the sintering of PcBN (40 – 60%) with Ti, Al as binders, variating the binders amount and sintering temperature. Phases resulting from the chemical reaction of the constituents were identified, namely TiN, TiB_2 and AlN, while the presence of hBN was identified together with cBN at 1500 ºC, with this last one disappearing completely at 1600 ºC. High densification values were achieved, and a decrease in hardness was observed with increasing amount of hBN present. Rong et al. [90] prepared PcBN composites with 30 – 50% cBN and Ni binder by variating the binders amount and sintering temperature. The authors observed that increasing the cBN amount did not lead to an increase in the PcBN hardness, which could be attributed to the formation of hBN, but no phase identifications were done. Hotta et al. [91] studied a PcBN composite of (30 – 50%) cBN with TiN as a binder by variating the binders amount and sintering temperature. Compared with the previously mentioned study, which used the same cBN powder amount with equivalent grain size but a metallic binder [92], it was necessary to use higher temperatures. Although slightly lower densifications were obtained, hardness values one order of magnitude higher were achieved. Zhang et al. [92] used a Ni coated cBN to produce (30%) PcBN material with Al_2O_3 as binder. Near full densification was achieved, and the presence of hBN was identified as a secondary phase, resulting in the highest hardness reported (HV of 24 GPa) for Low PcBN produced by SPS in Table 4. Jiang Feng et al. [93] used (40 – 60%) cBN with different coating materials (Ni, SiO_2) to produce a PcBN-SiO_2 composite, while also variating the binder amount and sintering temperature. The addition of a coating to the cBN particles improved the densification, where the ceramic coated cBN presented a slightly increase in hardness compared to the metallic coated one. Besides, the increase in the cBN amount did not lead to an increase hardness, and raised the required sintering temperature, yielding lower densifications. Bo Wang et al. [94] prepared a PcBN with (30%) cBN using WC, Co, Ni, P as binders, where it variated the particle size of the cBN and sintering temperature. No significant differences were observed in the sintering and mechanical properties of different grain sized cBN composites, both achieving high densifications and similar hardness values, probably due to the particle sizes not being that different (~2,5 μm and ~12 μm).

Concluding, high densifications could be obtained from sintering PcBN composites by SPS, but only Low PcBN with cBN amounts lower than the ones obtained with HPHT techniques (<70 vol%) were produced and, therefore, the respective achieved hardness values are limited to a maximum of HV = 24 GPa.

Table 4- PcBN compositions, sintering conditions by SPS and mechanical properties.

Initial cBN powder	Composition (vol. %)	Sintering conditions	Temperature (°C)	Final phases	Densification (%)	HV (GPa)	Fracture toughness (MPa.m$^{-1/2}$)	Bending strength (MPa)	Ref.
cBN (30 – 40 µm)	40% cBN – 40% Ti – 20% Al	Argon 50 MPa Heating rate of 100 °C/min 600s	1400	-	97	-	-	238	[18]
	45% cBN – 35% Ti – 20% Al		1200	-	91	8	2	~200	
			1400	cBN+TiN+TiB$_2$+AlN	99	14	7.5	391	
			1500	**cBN**+hBN+TiN+TiB$_2$+AlN	97	12	4.5	~275	
			1600	hBN+TiN+TiB$_2$+AlN	93	8	3.5	~225	
			1700	-	91	5	2.5	~200	
	50% cBN – 30% Ti – 20% Al		1400	-	97	-	-	262	
	55% cBN – 25% Ti – 20% Al		1400	-	98	-	-	221	
	60% cBN – 20% Ti – 20% Al		1400	-	94	-	-	181	
cBN (2 – 4 µm)	30% cBN – 70% Ni	- 100 MPa Heating rate of 100 °C/min 600 s	900	-	94	2.5	-	-	[90]
			1200	-	99	3.5	-	-	
	50% cBN – 50% Ni		900	-	89	0.75	-	-	
			1200	-	91	1.5	-	-	
cBN (2.8 µm)	30% cBN – 70% TiN	Vacuum (- Pa) 100 MPa Heating rate of 100 °C/min 600 s	1600	-	92	16	-	-	[91]
			1800	-	88	4	-	-	
	50% cBN – 50% TiN		1600	-	82	-	-	-	
			1800	-	86	-	-	-	
cBN (2 – 4 µm)	30% cBN/Ni^a – 70% Al$_2$O$_3$	- 100 MPa Heating rate of 100 °C/min 600s	1200	**cBN**+hBN+Ni+Al$_2$O$_3$	99	24	-	-	[92]
cBN (2 – 4 µm)	40% cBN – 60% SiO$_2$	- 100 MPa Heating rate of 100 °C/min 600 s	1200	-	93	4	-	-	[93]
			1400	-	95	10	-	-	
			1600	-	91	10	-	-	
	40% cBN/Ni^b – 60% SiO$_2$		1200	-	99	10	-	-	
			1400	-	97	9	-	-	
			1600	-	90	9	-	-	
	40% cBN/SiO$_2$^{c} – 60% SiO$_2$		1200	-	97	10	-	-	
			1400	-	100	13	-	-	
	60% cBN – 40% SiO$_2$		1500	-	74	1	-	-	
			1700	-	79	3	-	-	
			1800	-	73	2	-	-	
	60% cBN/Ni^b – 40% SiO$_2$		1500	-	87	7	-	-	
			1700	-	80	6	-	-	
	60% cBN/SiO$_2$^{c} – 40% SiO$_2$		1500	-	87	8	-	-	
			1700	-	83	7	-	-	
cBN (2 – 3 µm)	30% cBN - 55% WC – 11% Co – 3% Ni – 2% P	Vacuum (- Pa) 50 MPa Heating rate variable 600 s	1000	-	91	11.5	14	-	[94]
			1200	-	98	15.5	13	-	
cBN (10 – 14 µm)			1000	-	97	12	16	-	
			1200	-	99	18	13	-	

^{a}cBN particles coated with 1.7% mass of Ni; ^{b}cBN particles coated with 1% mass of Ni; ^{c}cBN particles coated with 1.9% mass of SiO$_2$.

The difficulty of sintering PcBN with these methods relies in achieving total densification while incorporating low amounts of binders and applying less intense conditions as possible, since less binder leads to an increase in hardness (Figure 11), but also an increase in sintering conditions to more extreme values, while high temperatures will promote phase transformation from cBN to hBN resulting in a drastic decrease in hardness of the final material.
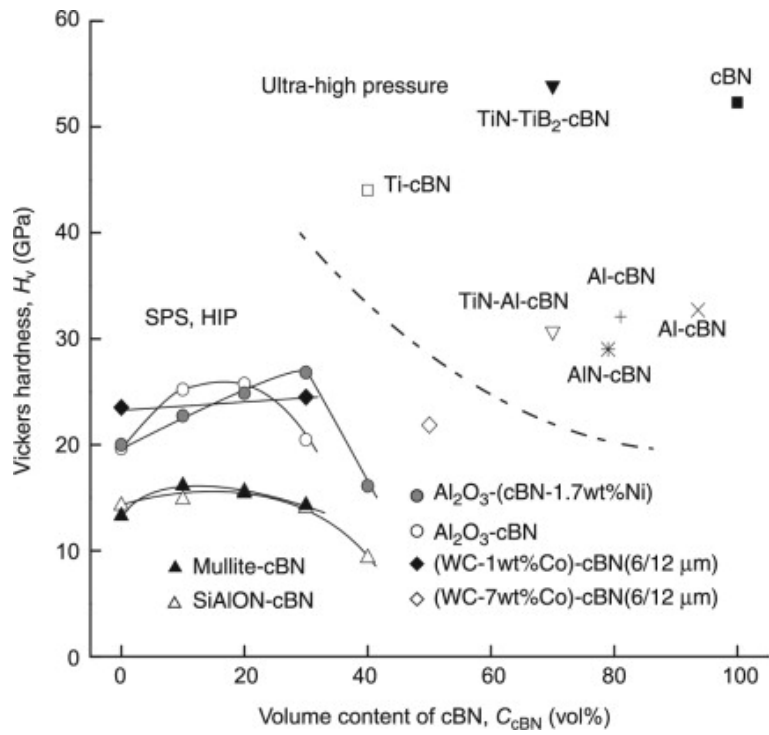
Figure 11- Comparison of hardness vs cBN volume incorporation of PcBN composites achieved by ultra-high pressure techniques (in the order of GPa) and by less intense techniques like SPS and HIP [70].

Chapter 3- Experimental Procedure

3.1 Selected constituents

In this work the commercial powders indicated in Table 5 along with some initial characteristics indicated by the suppliers were used.

Table 5- Information of the initial powders used in this work.

Designation	Supplier	Information according to suppliers		Experimentally verified					
		Chemical composition	Particle size (µm)	Chemical composition	-	Density (g/cm³)	Elements composition		
							-	Atomic (%)	Mass (%)
cBN 510	Hyperion	cBN coated with 17% Ti (wt.%)	44	cBN coated with 17% Ti$_2$N (wt.%)	cBN	3.5	B	50	44
							N	50	56
					Ti$_2$N	4.8	Ti	33	87
							N	66	13
cBN	Ceratónia	cBN	1 – 2	cBN		3.5	B	50	44
							N	50	56
TiCN	Treibacher	Ti(C,N)	1.65	Ti(C,N)		5.2	Ti	50	78
							C	25	12
							N	25	10
mNi	Ampere	Ni	2.2 – 2.6	Ni		8.9	Ni	100	100

3.2 compositions

3.2.1 Phase Diagrams simulation

Phase diagrams for the cBN-TiCN/Ni systems were simulated by performing thermodynamic calculations using the Thermo-cal software, version 2021b, with TCFE11 Steels/FE-alloys database [95]. To define the systems composition were considered as constituents BN, Ti, C, N and Ni when present.

3.2.1 Compositions preparation

Four different compositions were prepared with different methods as indicated in Table 6: mechanical mixture (MM), ball milling (BM), and colloidal processing (CP).

Table 6- Compositions characteristics and used preparation method.

	Vol. %				Wt. %				Preparation method
	cBN	Ti$_2$N	TiCN	mNi	cBN	Ti$_2$N	TiCN	mNi	
Composition 1	73	10	17	-	65	13	22	-	MM
Composition 2	69	10	16	5	58	12	20	10	MM
Composition 3	53	-	47	-	43	-	57	-	CP
Composition 4	50	-	45	5	39	-	51	10	BM or CP

The mechanical mixture method (MM) consisted in the agitation of the powders in dry medium for 1 h 30 min using a 3D powder mixture in a Turbula equipment (Aveiro).

The ball milling method (BM) consisted in the milling and homogenization of the powders in ethanol by roller agitation using Teflon spheres as grinding bodies. With the container filled to around 1/6 of its volume, it was added polyethylene spheres and let

the medium in agitation for 15 h at 33 rpm. After, the mixture was dried in an oven at 110 ºC.

The colloidal processing method (CP) consisted in adding a dispersant to the colloid, followed by ball milling in a liquid medium. For its preparation it was decided to make a mixture containing 45 vol% of solid phase, and a dispersant amount corresponding to 0.5 wt% for cBN, 0.5 wt% for TiCN, and 7 wt% for Ni powder [96,97]. As an example, when preparing 20 g of composition 4 it necessary to used 7.8 g of cBN, 10.2 g of TiCN, 2 g of Ni, a total of 0,46 g of long PEI (see section 3.4 for the commercial characteristics of the dispersants used) and 5,23 g of distilled water. The total dispersant amount was added in distilled water, followed by mechanical mixture for 5 min at 350 rpm. Maintaining the mechanical agitation of 350 rpm, the powders were slowly added one by one, with 5 minutes of mixture and application of ultrasounds for 30 sec between each. This was done following the order: water, dispersant, Ni powder, TiCN powder, cBN powder, to allow the polymer to immediately adsorb on the powders' surface and minimize the exposure time to water and consequent oxidation (particularly for the Ni powder), while also allowing an easier dispersion of the minor phases in the main ones. The ph was checked again and corrected to around 9, if necessary. The prepared colloid was homogenised by ball milling for 1 h at 90 rpm, using SiC spheres with two different diameters (3 and 5 mm) as grinding bodies and an air:colloid:grinding bodies proportion of 1:1:1 in relation to the holding container. After, the grinding bodies were removed, and the colloid was dried by rotary evaporation at 50 ºC and 75 rpm with gradual increase of the vacuum down to 100 mbar. The resulting powder was sieved to break agglomerates.

3.4 Colloidal characterization of cBN

When a powder is added to a liquid, charges are formed on the particles' surface which interact with its surroundings [99,100]. This interaction results in a behaviour that is dictated by the total potential energy of the system according to (1) [100,101]:

$$V_T = V_{vdW} + V_{eletronic} + V_{Stern} + V_{structural} \qquad (1)$$

Where V_T is the total potential energy of the system, V_{vdW} is the potential energy form the van der Walls interaction between the particles, $V_{eletronic}$ is the potential energy of the electrostatic repulsion generated by equally charged particles, V_{stern} is the potential energy of the interaction of polymer adsorbed particles (steric interactions), and $V_{structural}$ the potential energy of unabsorbed species in the liquid medium. The system reaches an equilibrium when the repulsive and attractive forces create an energy barrier at which repulsive forces are greater, illustrated in Figure 12 [99].
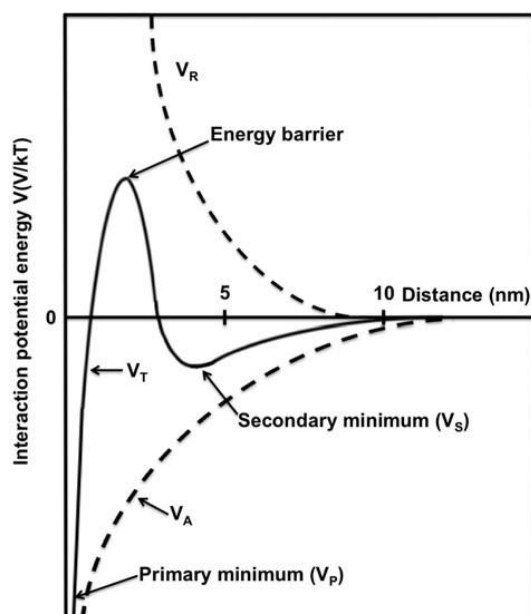
Figure 12- Graphical representation of the attractive (V_A) and repulsive (V_R) forces interaction in function of distance between particles described by the DLVO theory [102].

To achieve a stable homogeneous mixture in time with deagglomerated particles it is necessary to apply a mixture process according to the particles size [99,101]. For nanometric size particles one possibility is the colloidal processing route. Colloidal processing consists in obtaining a uniform and deflocculated mixture of a solid phase in a liquid by manipulation of potential energy of the system using chemical and/or mechanical methods. In the solution is applied a dispersant, generally a polymer, with will adsorb to the particles surface and repel each other, followed by ball milling to homogenize the solution and physically break the agglomerates to expose all the particles surface, allowing the polymer to adsorb to it [99]. It is important to use a correct amount of polymer for separating particles, since insufficient amount will not prevent the formation of agglomerates and in excess amount the polymer chains will interlock and form bridges between particles, essentially forming agglomerates. It is also point out that the adsorption capability of the polymer is influenced by ph and temperature of the system [99,103].

Colloidal characterization was performed on the cBN powder by measuring the zeta potential of the colloidal and grain size in an aqueous medium where the ph was variated and two different dispersants (polyelectrolytes) were used.

To measure the zeta potential of cBN in function of pH it was made different pH colloids using distilled water, KCl salts (Fisher scientific), hydrochloric acid (37%, Sigma-Aldrich) and tetramethylammonium hydroxide (25% in water, Merch KGaA). Applying the KCl salts in distilled water in a concentration of 10^{-2} g/L, followed by the cBN powder in a concentration of 0,1 g/L, six samples were subjected to ultrasounds for 20 sec. After, the acid and base solutions were added to the samples to obtain different ph solutions across the 1 to 14 pH scale. The samples were subjected to 1 h of agitation to stabilize the ph of the medium and to prevent sedimentation of the powder. The zeta potential and grain size of the colloids were measured in the equipment Zetasizer nano series, Malvern brand (Madrid), with 120 sec of stabilization and a material refraction index of 2.1 [104].

Distilled water was used for the colloidal characterization of the cBN powder and two varieties of Polyethylenimine (PEI), designated as short PEI (50% in water, average molecular weight of ~2000 g/mol, Aldrich Chemistry) and long PEI (with ramifications, average molecular weight of ~25000 g/mol, Aldrich Chemistry). For both cases, seven samples of distilled water with a cBN concentration of 0.1 g/L were prepared, and dispersant in the amounts 0, 0.25, 1, 2, 4 and 6 wt% t in relation to the cBN powder. The constituents were added in the order: water, dispersant, cBN powder, followed by application of ultrasounds for 20 se. After 4 h of agitation, for homogenising and preventing powder sedimentation, the pH and zeta potential were measured using the same equipment mentioned above. The pH of the colloids was adjusted to around 9, if necessary.

3.5 Spark Plasma Sintering of the samples

Spark Plasma Sintering (SPS) is a sintering technique capable of applying simultaneously pressure and temperature (by electrical heating) to a powder to sinter it. The equipment consists of graphite punches and die, where the powder is deposited, which are placed between the machine punches capable of applying pressures up to 100 MPa and closes the electrical circuit, allowing the application of electric current of 1 - 10 kA that by Joule effect can reach heating rates up to 1000 ºC/min. These parts are all located inside a closed chamber that allows the use of different atmospheres or vacuum of 1 – 10 Pa, illustrated in Figure 13 [19].
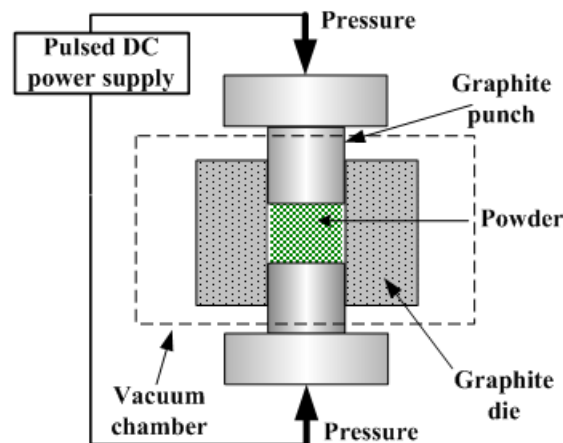
Figure 13- Schematic representation of a SPS equipment [105].

Inside the equipment, an electric field is applied to the circuit and by Joule effect the graphite die which being a thermal conductive material transmits the generated heat to the powder by thermal conduction. Despite the sample being very good or bad electrical conductor, most of the heat is generated by the graphite die. A second mechanism is theorized to occur which allows the densification of the sample, named micro-spark/plasma theory, but its occurrence inside the sample is still to be confirmed [19,106].

The sintering of the samples was performed in the Spark Plasma Sintering equipment Fuji Electronic Co, model Dr Sinter SPS-510CE (Madrid), using graphite punches with 10 mm in diameter. The investigated SPS conditions were applied according to Table 7, and the cooling was done at a rate of 100 ºC/min down to 500 ºC, at point where the equipment was turn off and let the samples cooling naturally inside

the chamber. During the sintering process, the punches displacement, vacuum, pressure, and temperature were recorded every second. Taking the recorded punches displacement and temperature in situ, dilatometric curves could be represented.

Table 7- Sintering conditions applied to each sample.

Composition	Sample	Heating rate (ºC/min)	Pressure (MPa)	Temperature (ºC)	Dwell time (min)
Composition 1	2000 ºC			2000	
Composition 2	1400 ºC			1400	
	1500 ºC			1500	
	1600 ºC			1600	
	1700 ºC			1700	
	2000 ºC	100	60	2000	10
Composition 3	2000 ºC – CP			2000	
Composition 4	1700 ºC – BM			1700	
	1800 ºC – BM			1800	
	1700 ºC – CP			1700	
	1800 ºC – CP			1800	

3.6 Powder and Composites Characterizations

3.6.1 Particle size distributions

The particle size distribution of the powders was measured using the laser diffraction technique, which measures the equivalent spherical diameter of the particles suspended in a liquid medium. It was used the equipment Coulter model LS230, with water as the liquid medium and no dispersant was added.

3.6.2 Chemical, microstructural and morphology characterization

The morphology and microstructural characterization were performed by Scanning Electron Microscopy (SEM) and the chemical characterization was performed by Energy-dispersive x-ray Spectroscopy (EDS) using the following equipment's (when not mentioned, the results were acquired using the SEM Hitachi model SU-70):

- SEM Hitachi model S-4700 with an attached EDS microanalysis system – Institute of Ceramic and Glass (Madrid);
- SEM Hitachi model SU-70 with an attached Bruker EDS microanalysis system, model Quantax 400 – Department of Materials and Ceramic Engineering (Aveiro);
- SEM Hitachi model SU-4100 with an attached Rontec EDS microanalysis system – Department of Materials and Ceramic Engineering (Aveiro);
- SEM Phenom Pro (G5) with an attached Phenom silicon drift detector (SDD) – Palbit S.A (Aveiro)

The powders were placed in carbon tape. The bulk samples preparation consisted in cutting the samples cylinders into discs using a diamond coating disc saw, followed by polishing of the surface with magnetic diamond polishing discs of 54 and 18 µm granulometry, as well as polishing clothes with diamond paste of 9, 6, 3 and 1 µm granulometries, while applying ethylene glycol as lubricant. Afterwards, the samples

were placed on sample holder using conductive carbon tape. The surface was made electrically conductive by applying a carbon or gold coating.

3.6.3 Crystallographic structure characterization

3.6.3.1 X-ray Powder Diffractometry

The X-ray Powder Diffractometry (XRD) technique was used to determine the phase content. This was performed in the equipment's Panalytical (Almelo, Netherlands) model X´Pert PRO[3], and Bruker D8 Advance, both using a Bragg-Brentano configuration and a copper ampoule. The materials were analysed in powder or bulk form and using the conditions indicated in Table 8. For the samples reduced to a powder form, they were crushed using a steel pestle and mortar and sieved (75 µm mesh).

Table 8- Experimental conditions used for the XRD analysis.

		Physical form	Interval (2θ)	Step size (2θ)	Step time (s)
Powders	cBN 510	Powder		0.0260º	96
	cBN	powder		0.0260º	96
	mNi	powder		0.0260º	96
Compositions	Composition 2	powder		0.0260º	96
	Composition 3	powder		0.0260º	96
	Composition 4	powder		0.0260º	96
Samples	Composition 1 - 2000 ºC	bulk		0.0490º	153
	Composition 2 – 1400 ºC	powder		0.0260º	96
	Composition 2 – 1500 ºC	powder	20º - 60º	0.0260º	1
	Composition 2 – 1600 ºC	bulk		0.0490º	197
	Composition 2 – 1700 ºC	powder		0.0490º	197
	Composition 2 – 2000 ºC	powder		0.0260º	96
	Composition 3 – CP – 2000 ºC	bulk		0.0260º	96
	Composition 4 – BM – 1700 ºC	powder		0.0260º	96
	Composition 4 – BM – 1800 ºC	Bulk		0.0260º	96
	Composition 4 – CP – 1700 ºC	powder		0.0260º	96
	Composition 4 – CP – 1800 ºC	powder		0.0260º	96

The phases indexation process was done using the PDF-4+ 2022 database from ICDD (International Centre for Diffraction Data) and the HighScore Plus program, the XRD analysis software from Malvern Panalytical [107,108].

3.6.3.2 Rietveld refinement

To quantify the amount of each phase indexed from the XRD of composition 2 samples, sintered at 1500 and 1700 ºC, it was followed the Rietveld refinement method [109]. The analysis was performed in the equipment's Panalytical (Almelo, Netherlands) model X´Pert PRO[3](Aveiro), and PANalytical Empyrean diffractometer (Aveiro). The samples were firstly worn off in all the surface to remove traces of graphite from the sintering die, then grinded using a steel pestle and mortar, and finally sieved with a 75 µm mesh size. The samples were analysed using the conditions indicated in Table 9.

Table 9- Experimental conditions used for the XRD analysis.

Composition	Temperature (ºC)	Physical form	Interval (2θ)	Step size (2θ)	Step time (s)
Composition 2	1500	powder	20º a 95º	0.026º	96
	1700	powder	20º a 95º	0.013º	3998

For the application of the Rietveld refinement method to the XRD diffractograms of the samples it was used the HighScore Plus program, the XRD analysis software from Malvern Panalytical, and considered the phases indicated in Table 10 along with respective ICCD PDF file and theoretical density.

Table 10- Theoretical densities, retrieved from the respective ICDD PDF file, for each considered phase used in Rietveld analysis.

Phase	Theoretical density (g/cm^3)	ICDD PDF file
cBN	3.5	04-008-4847
hBN	2.3	04-013-1175
TiCN	5.2	04-011-9013
TiB$_2$	4.5	04-010-8470
Ni$_3$B	8.2	04-003-1948

3.6.3.3 Raman Spectroscopy

For complementing the phases identification, it was used the Raman Spectroscopy technique. Using an optical microscope, at a total lenses ampliation of 500x, a green laser of 514 µm wavelength was focused at 100 % power in individual BN grains of the samples and the resulting signal was processed on a inVia Raman Microscopy, Renishaw, (Madrid) with accumulation of 10 individual measurements. The data treatment was done in the LabSpec v5 program.

3.6.4 Physical characterization

The physical characterization of the samples consisted in determining the apparent density and open porosity using the Archimedes principle by following the standard ASTM C20-00 (Water Absorption , Apparent Specific Gravity , and Bulk Density of Burned Refractory Brick and Shapes by Boiling Water), but applying vacumm instead of boilling the samples. First, the samples were completely dry in a oven at 110 ºC and weighted (m_{dry}). Then, they were submerged in water inside a container and applied vacuum for a few minutes, followed by breaking the vacuum. The samples were then submerged in water again, 1 cm under the surface, and weighted (m_{imerse}). Finally, the surface of the samples was dried and weighted (m_{wet}). Each sample was measured 5 times and the apparent density and open porosity was determined using (1) and (2), respectively [110].

$$Apparent\ density = \frac{m_{dry} \times D_{H_2O\ at\ 25\ ºC}}{m_{dry} - m_{imerse}} \qquad (1)$$

$$\% \, Open \, porosity = \frac{m_{wet} - m_{dry}}{m_{wet} - m_{imerse}} \times 100 \qquad (2)$$

Chapter 4- Results and Discussion

Two different studies were performed in this work: i) the study of the thermal reactivity of cBN-TiCN-Ni based composites sintered by SPS using a coated cBN powder with a coarse particle size, where it was focus particularly on the phase transformation from cBN to hBN; and ii) a study of the densification of cBN-TiCN-Ni based composites with a uncoated cBN powder having a smaller particle size, during which the effect of the powder dispersion on the microstructure of the composite was studied alongside using two different methods: ball miling (BM) and colloidal processing (CP).

4.1 Thermal reactivity of cBN-TiCN-Ni based composites by SPS

4.1.1 Initial powders characterization

cBN 510, TiCN and mNi, powders were used, with the initial characteristics indicated in Table 6. The cBN510 powder was significantly coarser than the TiCN and Ni powders (Figure 14 and Figure 15). The cBN particles have an angular shape and are uniformly coated with Ti (Figure 14-b). The TiCN and Ni particles are rounder and are agglomerated, as oppose to the cBN510 ones, which are looser. The grain size distribution of the cBN 510 is very uniform, with an average grain size (D_{50}) of 57 µm (Figure 16-a), and are in fact coated with a titanium compound in a nitride phase (Ti_2N) (Figure 16-b), while no metallic Ti had been detected. The BN phase is in the cubic structure cBN (Figure 16-b).
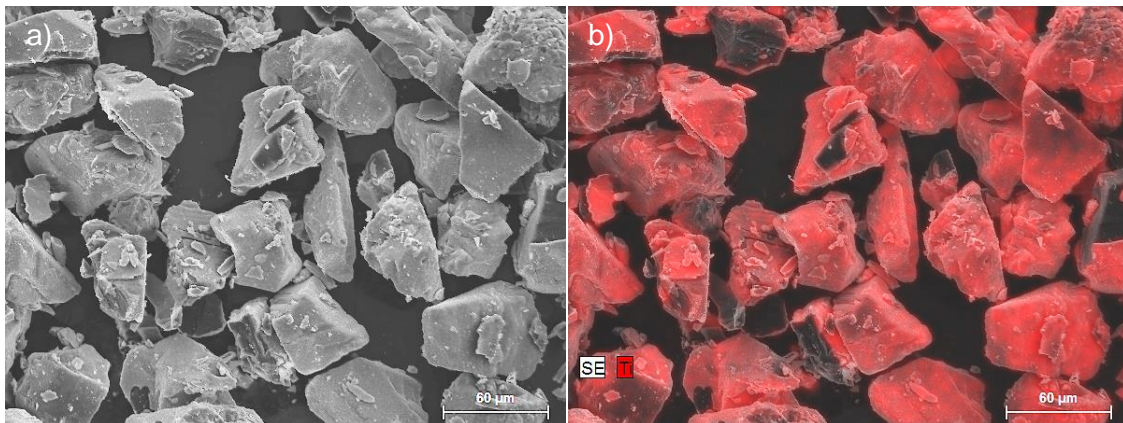
Figure 14- Morphology of the cBN 510 particles by (a) SEM, and a (b) EDS of the titanium coating.
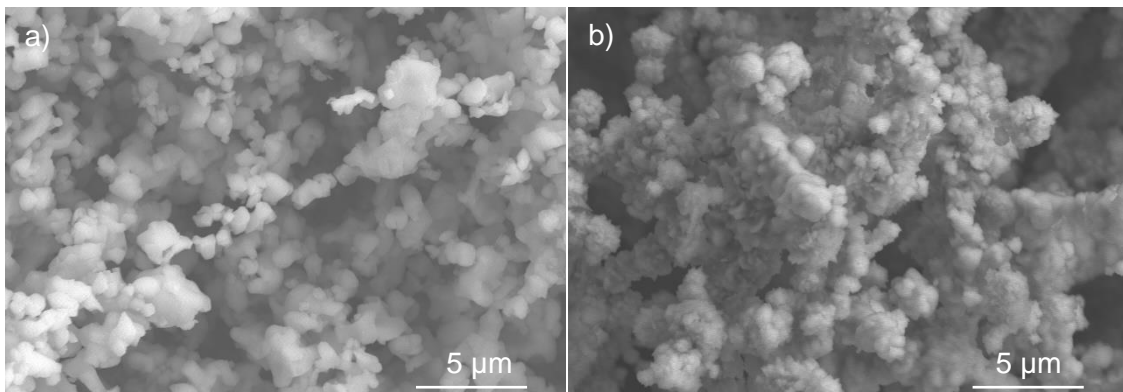
Figure 15- Morphology of the (a) TiCN and (b) mNi particles (acquired using the SEM Hitachi model S-4700).

a)   b)
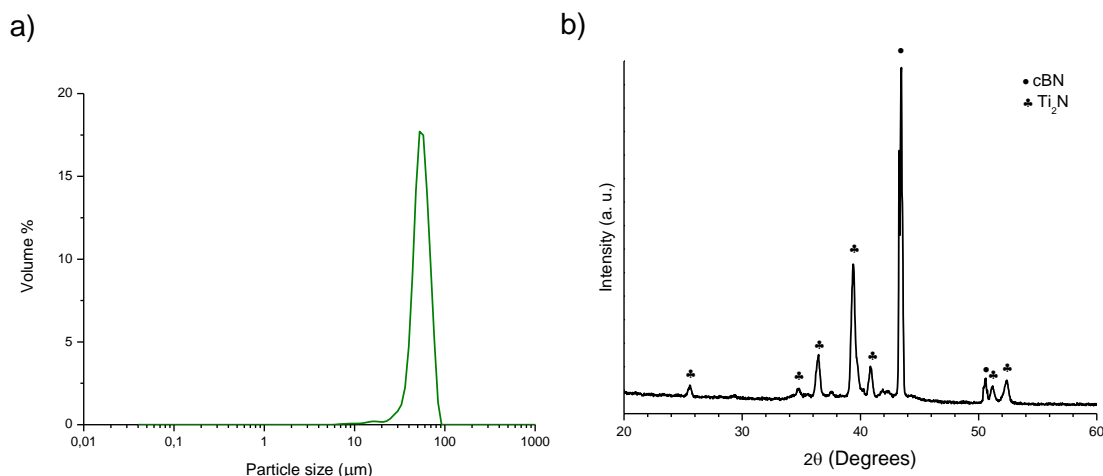
Figure 16- (a) Grain size distribution and (b) XRD pattern of the cBN510 powder.

4.1.2 Thermodynamic calculations of BN-TiCN phase diagrams with addition of Ni

The system of both compositions was defined using the constituents BN, Ti, C, N and Ni (If present) in mass amount (% m/m), with a pressure of 60 MPa. Due to the limitation in the TCFE11 database, where only the hexagonal phase was included, the calculations were done considering a stable hBN in all the temperature range.

The phases diagrams obtained from the thermodynamic calculations of the BN-TiCN and BN-TiCN-Ni systems are shown in Figure 17 and Figure 18 respectively. A temperature scale of 800 to 2100 ℃ was used, although it is generally accepted that equilibrium conditions are only attained for temperatures higher than 1000 ℃. Based on the phase diagrams in Figure 17 and Figure 18, the respective compositions 1 and 2, Table 6, were chosen to be inside regions where no graphite is formed at ~1000 ℃ (represented as red lines).

According to Figure 17 and Figure 18, and considering the initial phases of the powders used, it is expected that the TiB_2 phase will form and become stable in the system, while the Ti_2N phase, detected by XRD diffractogram of the cBN510 powder (Figure 16-b), will decompose from the system since is not indicated as stable. The formation of a TiB_2 phase for these types of systems was already predicted and experimentally confirmed by existing works [111–113]. With the addition of Ni, it is predicted to form a liquid phase at 967 ℃ which will be present up to 1736 ℃, and when cooled will lead to the formation of a stable Ni_3B phase. The formation of this phase indicates that metallic Ni will react with BN.
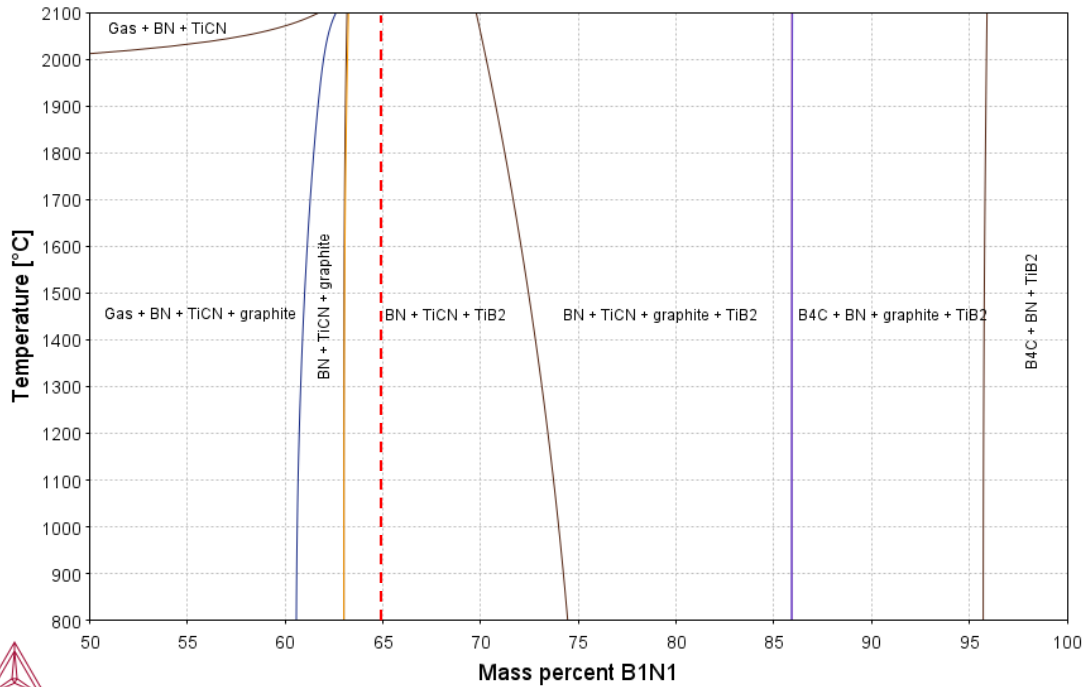
Figure 17- Predicted phase diagram for the BN-TiCN system. The dashed line corresponds to composition 1.
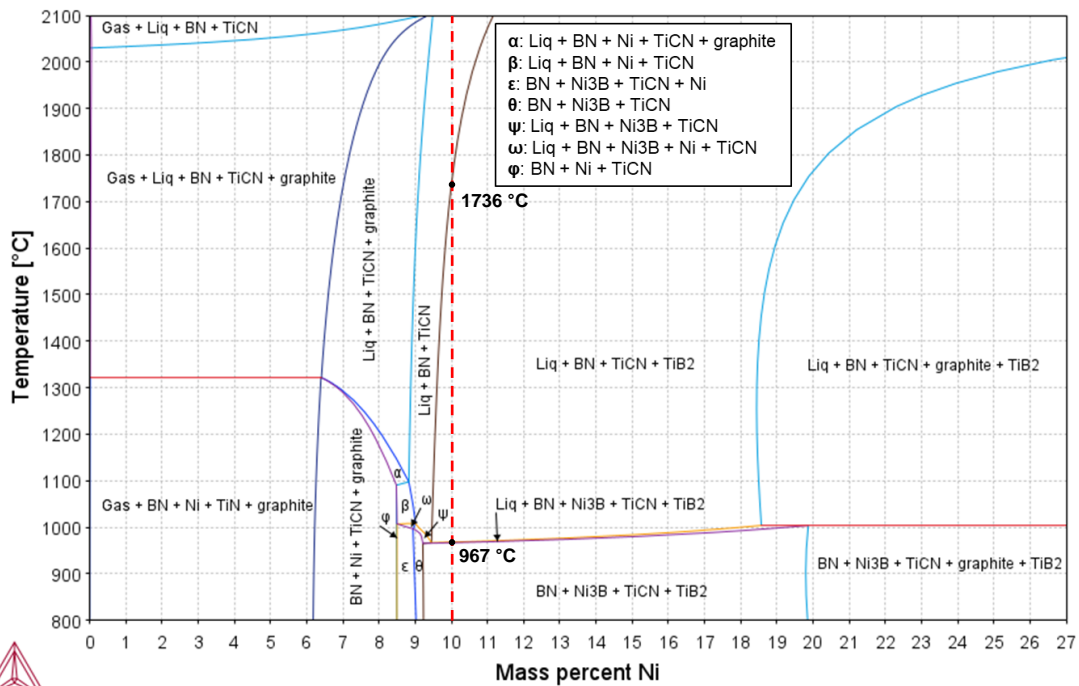
Figure 18- Predicted phase diagram for the BN-TiCN)-Ni system. The dashed line corresponds to composition 2.

4.1.3 Initial characterization of the compositions

Figure 19 shows the morphology of compositions 1 and 2 after mixing. The cBN510 and TiCN particles are easily distinguished in composition 1, due to the much

larger size of the former. This is not the case for composition 2, since the TiCN and Ni particles exhibit a similar mean particle size. In both cases, no clear heterogeneities are observed. An XRD analysis of the composition 2 is shown in Figure 20, indicating the presence of the cBN, TiCN, Ni and Ti_2N phases. As shown above, the cBN and Ti_2N phases come from the cBN510 powder (Figure 16-b).
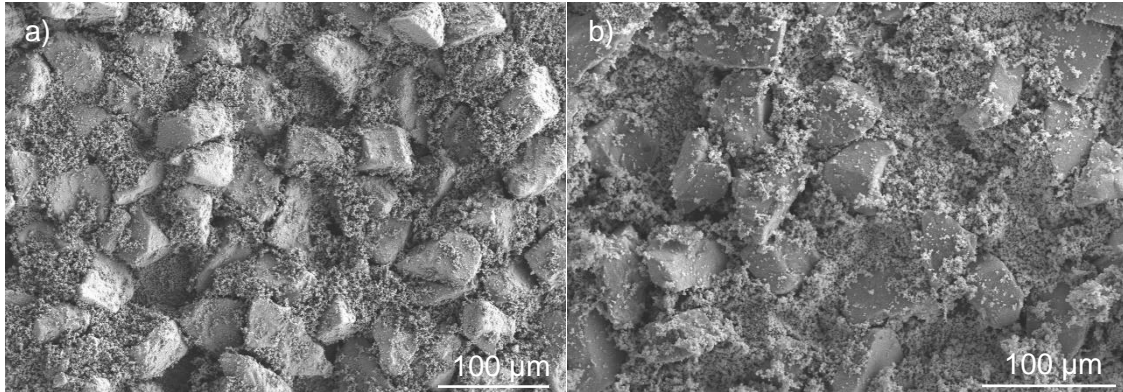
Figure 19- Microstructure of the two prepared compositions: a) composition 1 and b) composition 2 (acquired using the SEM Hitachi model S-4700).
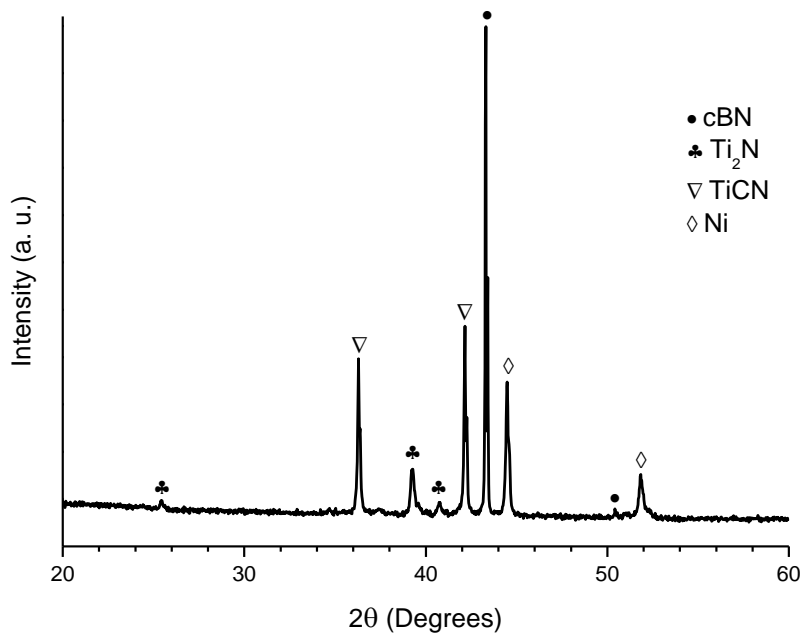
Figure 20- XRD diffractogram of the mixed composition 2.

4.1.4 SPS: Effect of nickel addition to cBN-TiCN

The sintering behavior was determined by dilatometric analysis during the SPS heating stage, as shown in Figure 21 for the compositions 1 and 2, without and with Ni respectively (Table 6). Figure 21-a depicts the dependence between shrinkage and temperature for both compositions and Figure 21-b the respective shrinkage rate curve. Different stages can be observed from the beginning of the densification process, ~600ºC up to 2000ºC. For both compositions, an initial faster shrinkage stage, stage I, is observed, originating a maximum shrinkage rate at ~1020ºC for composition 1. For composition 2, with Ni, the maximum shrinkage rate occurs at ~1170ºC. At this stage, the shrinkage rate of composition 2 became larger than that of composition 1 when T

approaches 1000°C, in close agreement with the appearance of the liquid phase at ~967 °C predicted in the phase diagram (Figure 18). In stage II, for T> ~1300°C, both compositions present equivalent and reduced shrinkage rates up to ~1700 °C. Above that temperature, a sudden expansion is observed in stage III, resulting in relevant peaks in the shrinkage rate graphs at ~1800°C and ~1760°C of composition 1 and composition 2, respectively, which should be associated to the phase transformation cBN-hBN. The starting transformation temperature of ~1700°C in this work is on the upper limit range of calculated temperature (1320 ± 380 °C) in the literature for the cubic to the hexagonal BN form transformation, but it should also be noted that the SPS conditions are far from equilibrium conditions [56]. The addition of Ni, as reported in the literature, slightly fasten the transformation and resulted in a larger shrinkage, as observed in Figure 21 [70,90]. After the expansion stage III, there is yet a final stage IV where the shrinkage rate is near constant and similar to that of stage II, for both compositions.
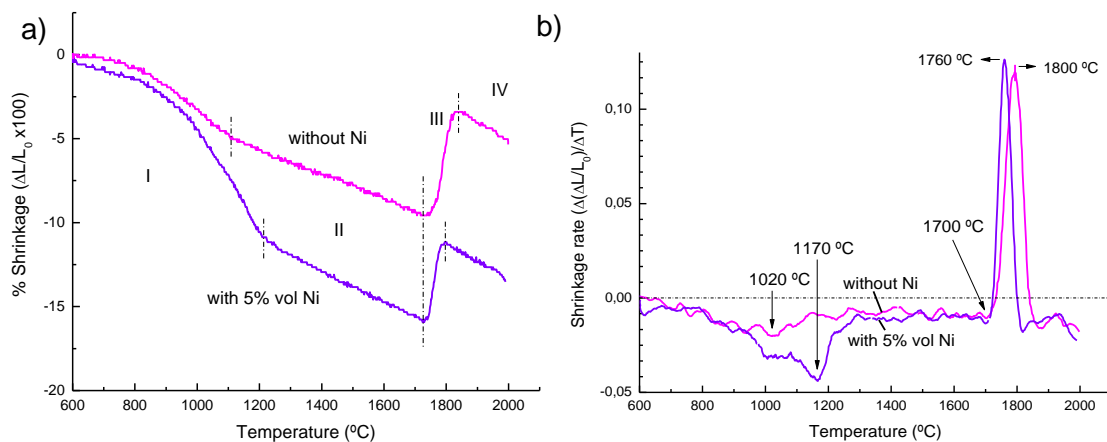
Figure 21- Shrinkage (a) and shrinkage rate (b) of composition 1 (without Ni) and composition 2 (with Ni) in function of the temperature using SPS.

From the XRD analysis of the phases present in both samples sintered at 2000 °C (Figure 22), four observations can be made: (i) the TiCN phase seems to remain stable during heating; (ii) only hBN was detected, meaning that all cBN transformed into hBN and, since there is a volume expansion associated to this transformation, it explains the volume expansion recorded in stage III of the dilatometric curves (Figure 21) [83]; (iii) the Ti_2N phase disappeared from the system and TiB_2 phase was formed, meaning that Ti_2N is not stable in the tested conditions while TiB_2 is, although the respective peaks are smaller in the composition containing Ni; (iv) in composition 2, containing Ni, there is the formation of the Ni_3B phase, falling in the four phase region $BN+Ni_3B+TiCN+TiB_2$ of the phase diagram (Figure 18). It can, then, be concluded that the phases detected by XRD in both compositions are those predicted by the respective phase diagrams in Figure 17 and Figure 18, and the final phase compositions fall in the region of 3 or 4 phases, as expected.
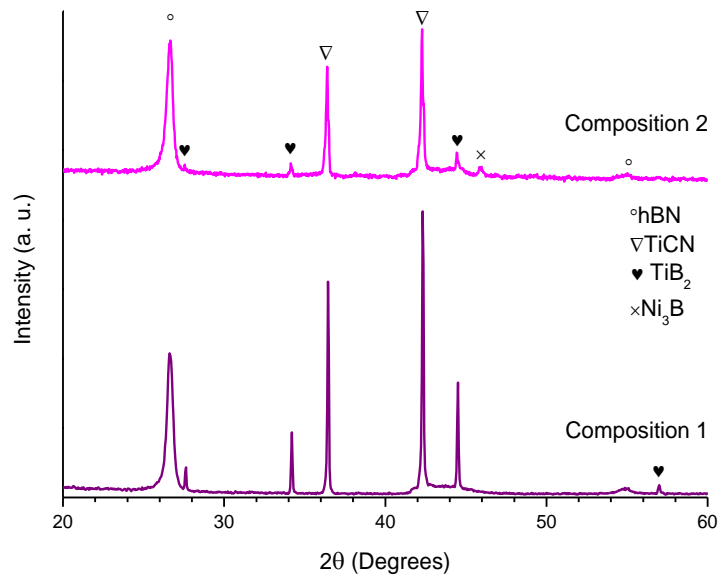
Figure 22- XRD patterns of the sintered composition 1 and composition 2 by SPS.

4.1.5 SPS: effect of temperature variation on cBN-TiCN-Ni compositions

To study the effect of temperature in the shrinkage of composition 2, several SPS heat treatments have been performed between 1400 and 1700ºC (Figure 23), where the cBN phase was expected to be yet predominant. With increasing temperature, the shrinkage increases but the shrinkage rate, after the maximum ~1170 ºC, is progressively decelerated until it reaches zero at 1700 ºC (Figure 23-b), as shown in Figure 21.
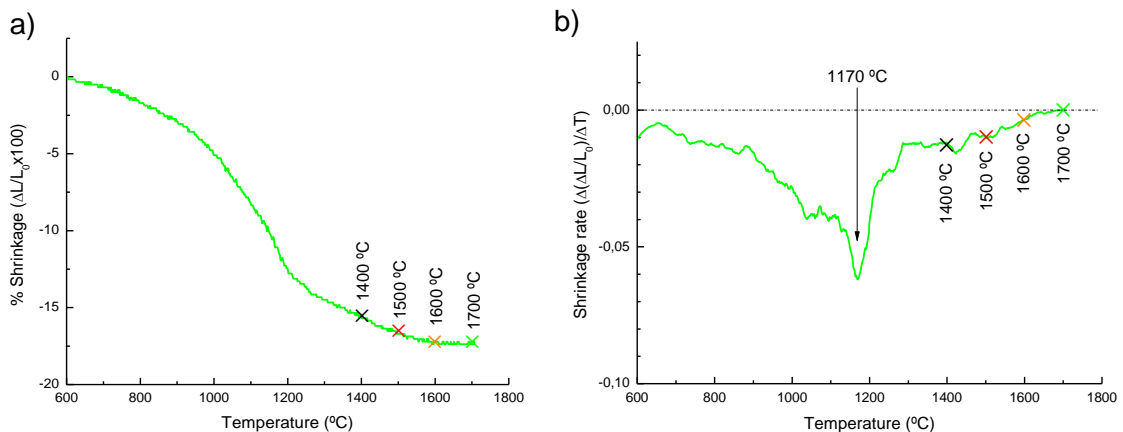
Figure 23- Shrinkage (a) and shrinkage rate (b) in function of temperature of the samples from composition 2, sintered at 1400 – 1700 ºC and 60 MPa.

Figure 24-a shows the apparent density and open porosity of the samples in function of the sintering temperature. Apparent density is decreasing slightly with increase in temperature up to 1600 ºC whereas above that temperature it significantly diminishes. As for open porosity it fluctuates around 16% between 1400 - 1600 ºC but reduces to zero at 1700 ºC. The slight decrease of apparent density with a near constant open porosity between 1400 - 1600ºC is attributed to a small extent of cBN to hBN phase transformation (Figure 24-b), since 10 minutes of holding time were done at those high

temperatures. From 1600 up to 1700ºC, the apparent density declined abruptly with complete elimination of open porosity, which is a consequence of the accelerated phase transformation (Figure 24-b), since the density of hBN (2.2 g/cm³) is lower than that of cBN (3.5 g/cm³), and its volumetric expansion can contribute to the removal of porosity.
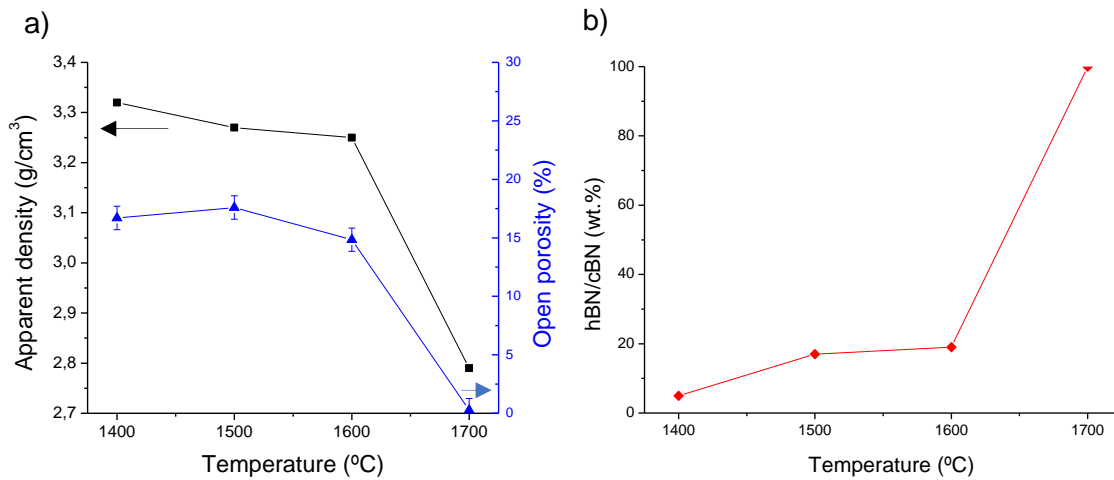
Figure 24- a) Apparent density and open porosity of samples from composition 2 sintered by SPS at temperatures of 1400 – 1700 ºC, and b) the hBN/cBN wt.% amount retrieved from the net area of XRD peaks of hBN and cBN respectively.

A comparison of the XRD profiles in composition 2 for the green powder and after SPS at different temperatures, in

Figure 25, shows that the phase compositions after sintering remains the same as the one sintered at 2000 ºC, Figure 22, and predicted by the phase diagram of Figure 18, as summarized in Table 11. In what concerns the phase transformation of BN from cubic to hexagonal, it is observed in

Figure 25 that, in fact, a small peak of hBN is already identified in the XRD profile of the sample sintered at 1400 ºC which has a small increase up to 1600 ºC, as can be observed in Figure 24-b. In the interval from 1600ºC up to 1700 ºC the transformation proceeds at a higher rate and at 1700ºC the cBN phase is absent, while the formation of an amorphous phase is evident by the higher background of the XRD profile between 42º to 47º interval in Figure 25 (see enlarged magnification profile at the right side).
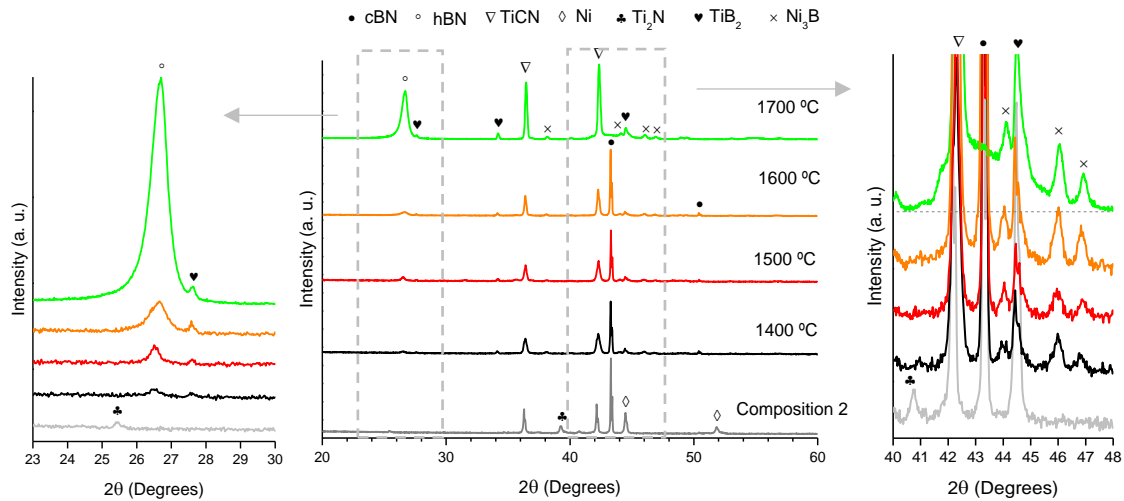
Figure 25- XRD patterns of the composition 2 as-mixed and after SPS at different temperatures (with enlarged magnification profiles between 23-30º on the left and 40-48º on the right).

Table 11- Comparison of initial, predicted and detected phases of composition 2 sintered samples.

Sintering Temperature (ºC)	Predicted phases** (Thermo-Calc)	Detected phases (XRD)	hBN/ cBN (wt%)***
*	-	cBN+ Ti_2N+TiCN+Ni	0
1400		cBN + hBN + TiCN + TiB_2 + Ni_3B	5
1500		cBN + hBN + TiCN + TiB_2 + Ni_3B	17
1600		hBN + cBN + TiCN + TiB_2 + Ni_3B	19
1700	BN + TiCN + TiB_2 + Ni_3B	hBN + TiCN + TiB_2 + Ni_3B + amorphous phase	100
2000		hBN + TiCN + TiB_2 + Ni_3B + amorphous phase	100

*as-prepared composition 2; **Considered below 1000 ºC; ***Based on the net area of XRD peaks of hBN and cBN respectively.

The phases' compositions of the samples sintered at 1500 ºC and 1700 ºC were yet determined using the Rietveld refinement method. The fitting difference plots are shown in Figure 26, with fitting quality parameters in Table 12, and phase compositions given in Table 13. Compared to the nominal phase composition 2 in Table 1, the BN phase percentage after SPS is higher than expected, i.e., it is 58 wt% before sintering and after sintering, where some boron reacts with Ti and Ni to form the phases TiB_2 and Ni_3B, respectively, the calculated percentage is 74 wt% for the 1500 ºC. On the other hand, the phases of TiCN, TiB_2 and Ni_3B are in a lower percentage than expected. According to the calculated results obtained by Thermo-calc software, boron atoms can solubilize on the Ni liquid phase (for instance, 7wt.% at 1700 ºC), which indicates that the BN phase dissolves in the melted Ni phase and dissociates into B and N atoms, with N being removed from the material. During cooling, the dissolved B can react and form Ni_3B phase according to the reaction of Eq. (4).

$$2\,BN + 6\,Ni \rightarrow 2\,Ni_3B + N_2 \tag{3}$$

Additionally, composition 1 did not had Ni to form a liquid phase in the system, but still had the presence of the TiB_2 meaning that some solid-state reactions occurred. Considering that the initial Ti_2N coating dissociated into Ti and N_2 phases, since this one

is not a stable phase in this system, the Ti atoms can react with the B atoms to form TiB_2 following the reaction of Eq. (5).

$$2\ Ti_2N + 8\ BN\ \rightarrow 4\ TiB_2 + 5\ N_2 \qquad (4)$$
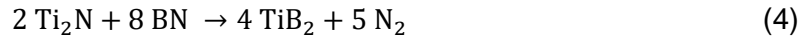
Although some BN had reacted during sintering to form those secondary phases, it was also observed the formation of some amorphous phase at 1700 ºC in

Figure 25, and additionally, in a few experiments it was observed to occur some squeezing of a small amount of material out of the mould, which according to EDS results is mainly constituted by Ni and some Ti. Despite the refereed uncertainty in the values of Table 13, the calculated ratio of hBN/cBN is only ~7 wt% at 1500ºC, whereas only hBN is detected at 1700ºC.

a)   b)
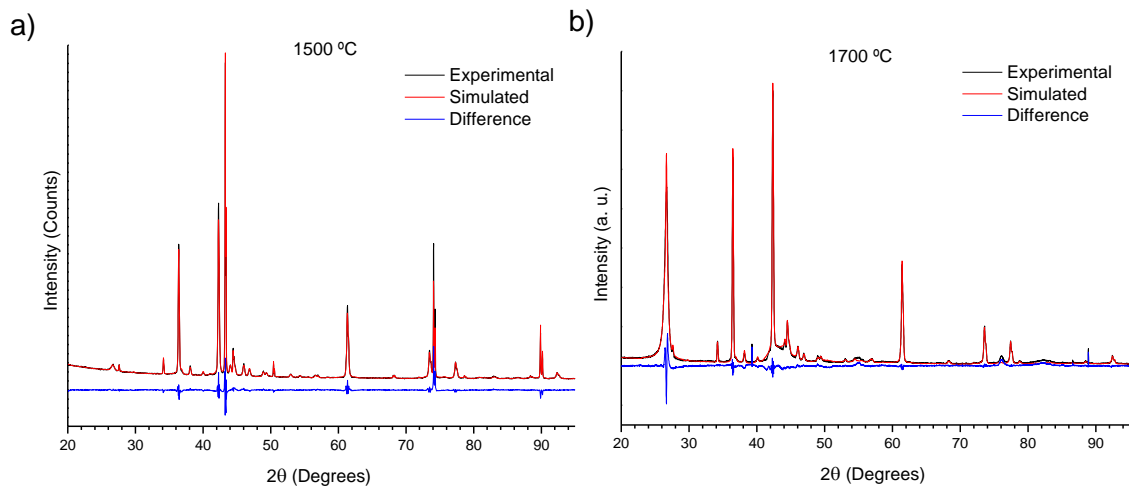
Figure 26- Rietveld refinement results plot for samples of composition 2, sintered at a) 1500 ºC and b) 1700 ºC.

Table 12- Fitting parameters of the Rietveld method performed on sintered samples of composition 2.

Sintering temperature (ºC)	Rwp	Rexp	Rp	χ^2
1500	5.07	1.67	2.98	3.03
1700	14.68	2.88	9.49	5.09

Table 13- Phases' composition and physical characteristics of the composition 2 after SPS.

Phases	1500 ºC (wt %)	1700 ºC* (wt %)
cBN	69	-
hBN	5	69
TiCN	19	24
TiB_2	2	2
Ni_3B	5	5

*Some metallic material (Ni/Ti) exited the mold during sintering.

36

4.1.6 Microstructural characterization

Figure 27-a depicts the microstructure of composition 2 sintered at 1600 °C. The difference between the BN phases is obvious, with the predominant cubic phase exhibiting sharp edges and a planar surface, while the hexagonal one as a rougher appearance, being the grains detached from the matrix. The difference in texture of the two phases has already been observed in other works, where there is indication of hBN forming from the surface of the cBN grains [18,67,114,115]. The Raman spectra performed in random individual BN grains of samples sintered in the 1400 – 1700 °C interval, are shown in Figure 27-b. The spectra, indicates only the presence of the cubic phase at 1056 and 1304 cm^{-1} and the hexagonal at 1367 cm^{-1}, meaning that no metastable BN phase was formed [116]. Although cBN particles could yet be detected by Raman spectroscopy at 1700 °C, Figure 27-b, its amount should be below the detection limit of the XRD technique to not be detected in the diffractogram of

Figure 25.
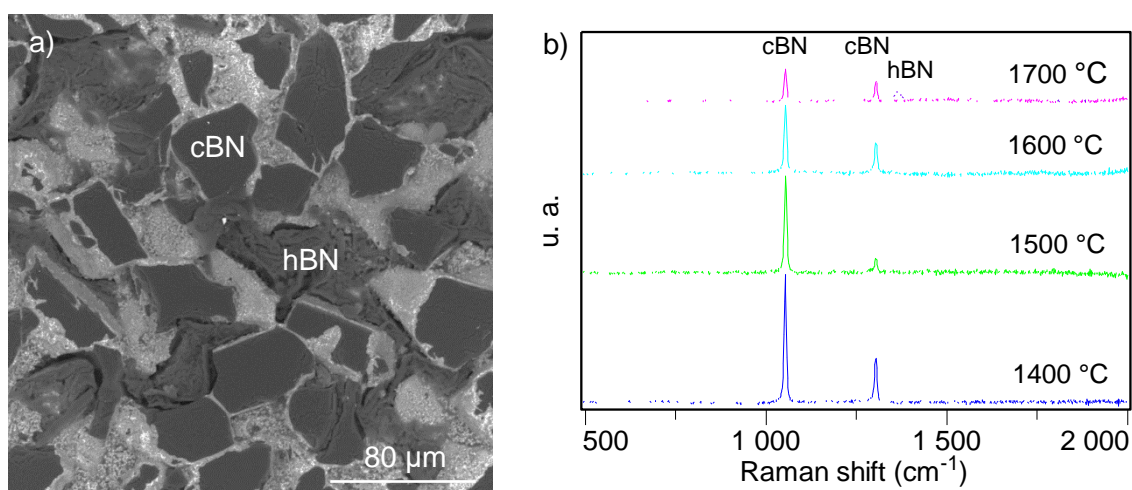
Figure 27- SEM image (a) of sample 2 sintered at 1600 °C, and (b) comparison of the Raman spectrums from individual BN grains of samples sintered at 1400 – to 1700 °C (acquired using the SEM Phenom Pro (G5)).

A comparison of representative microstructures of composition 2 sintered at 1400 -1700 °C is shown in Figure 28, along with an EDS elemental mapping for Ti, N and B. No relevant heterogeneities are found in the SEM images and the BN grains (darker regions) are well distributed in the matrix. Increasing the temperature there was a significant improvement in the wetting of the BN grains and elimination of the matrix porosity which was more evident at 1700°C. The EDS detection of Ti, B and Ni was used to identify the TiCN, BN and Ni phases, respectively. Despite B being a light element, the results align reasonably well with the coarser particles that were previously known to be BN. The binder is mainly constituted by Ti and some Ni, being clear that the spread of Ni is increased with increasing temperature. In the higher magnification of the microstructure at 1700°C and taking also the XRD results of

Figure 25 and respective theoretical densities of the phases in Table *10*, the matrix phases were identified as follows: the brighter white may correspond to Ni_3B, light grey to TiCN, dark grey to TiB_2.
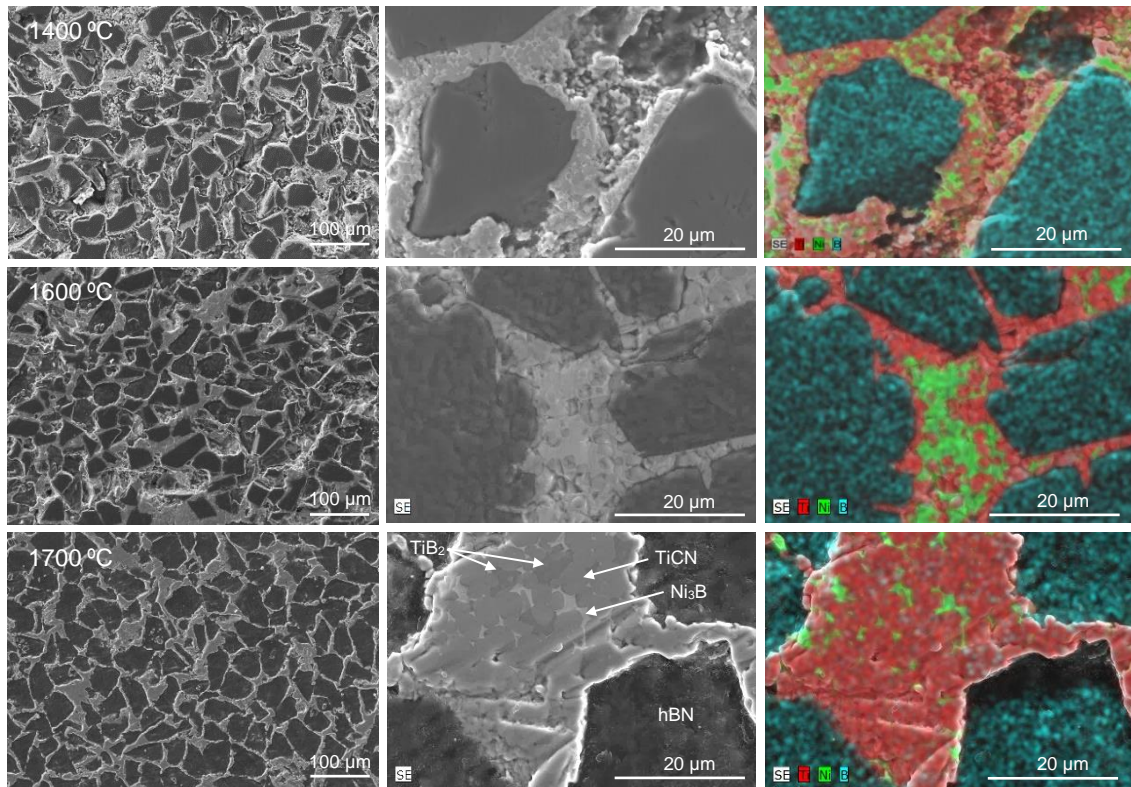
Figure 28- SEM and EDS of the samples from the cBN510-TiCN-Ni composition sintered at 1400 – 1700 ºC.

Although not presented, some mechanical characterizations were performed on composition 2 sintered a 1500 and 1700 ºC, namely Hardness measurements by Vickers Indentation and compressive strength by Diameter Compression (Brazil) Test Specimen. Ultimately, these results were inconclusive due to undefined indentation marks that did not allowed a precise measurement of the hardness, or irrelevant for the work since both composition 2 temperatures of 1500 ºC and 1700 ºC showed the same compression strength value of ~50 MPa, which are too low for any cutting tool application – even lower than the compression strength of hBN (Table 1).

Summarizing, it was observed that the Ni phase assisted in the sintering of the cBN-TiCN based composited, presumably with the formation of a liquid phase, and it possesses chemical reactivity with BN forming the Ni_3B phase. A great densification of the material was only possible at 1700 ºC when it was observed the cBN to hBN phase transformation. While the volume expansion helped removing the porosity inside the composite, it also removed all the cubic phase BN from it which is not the intended. With these results it was decided to decrease the amount of cBN incorporated in the system, and to decrease the particle size of the cBN, both in order to allow the sintering and densification of the PcBN composite with BN in its hard cubic phase.

As a sidenote, the results presented in section 4.1 are also presented in article form (attachment) and awaiting final revision from the co-authors before submitting to ECerS Open Access Journal: Open Ceramics. Additionally, an oral presentation of this section was already done in LVIII Congress of Spanish Glass and Ceramic Society 2022, in Madrid.

4.2 Effect of the initial powder dispersion on the microstructure of cBN-TiCN-Ni based composites sintered by SPS

4.2.1 Initial powders characterization

The cBN, TiCN and mNi powders were used, with initial characteristics indicated in Table 5, with lower particle size for cBN (1-2 µm) and the same TiCN and mNi used previously. While the characteristics of TiCN and mNi powders were already discussed in topic 4.1.1, cBN morphological and structural characteristics are shown in Figure 29 and Figure 30. This powder has an angular shape with sharp edges while displaying a loose behavior between particles (Figure 29). It is in the same range scale of the TiCN and mNi powders having two grain size families around 0,1 and 2 µm respectively, with an average particle size (D_{50}) of 1,5 µm (Figure 30-a). No other phase, besides cubic BN, was detected in the powder (Figure 30-b).
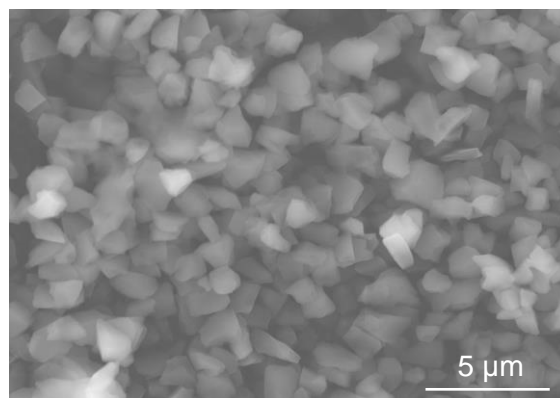
Figure 29- Morphology of the cBN grains (acquired using the SEM Hitachi model SU-4100).
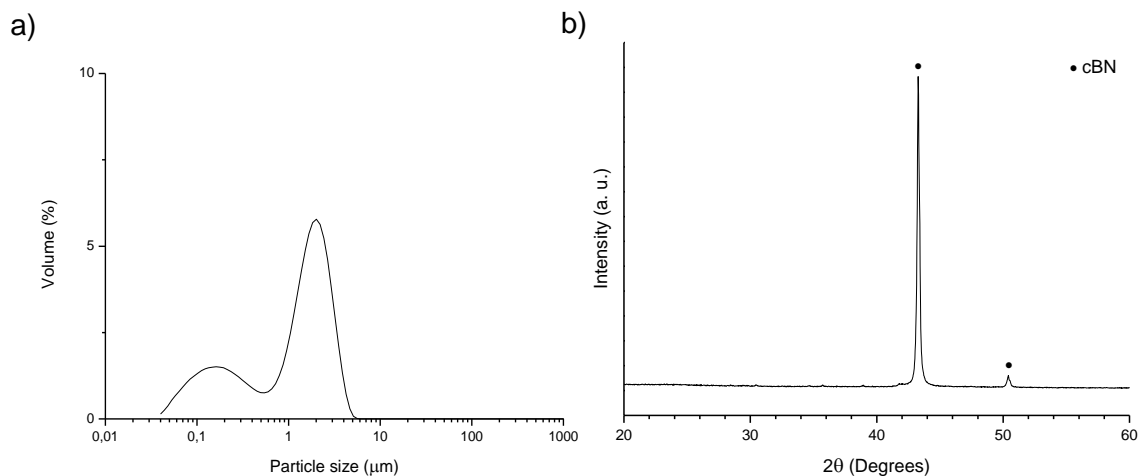
Figure 30- (a) Grain size distribution and (b) XRD pattern of the cBN powder.

4.2.2 Thermodynamic calculations of BN-TiCN phase diagrams with addition of Ni

New thermically stable diagrams were calculated using the constituents BN, Ti, C, N and Ni (If present) in mass amount, with a pressure of 60 MPa, also considering the hBN as the stable phase in all temperature range (Figure 31 and Figure 32). These diagrams differ from the ones determined in section 4.1.2 because the cBN 510 powder used in that study contained a Ti_2N coating of the particles

Based on the phase diagram of Figure 31, the composition 3 of Table 6 was fixed as a base composition with a lower amount of cBN than the previous ones (composition 1 and 2) to facilitate the densification process (represented as a red line). In this case it was not possible to prevent the formation of the graphite phase. When a Ni phase is added to composition 3 (Figure 32), only the phase region identified as η does not show graphite as a stable phase at temperatures lower than ~1000 ºC (other regions such as δ, ε, and θ does not have practical size on the diagram), but it is required to add >11 wt.% of Ni. Since it was not intended to exceed a Ni amount of 10 wt% for the PcBN, it was decided to use that amount (Figure 32, represented as a red line).

According to Figure 31 it is predicted in composition 3 the presence of BN and TiCN and the formation of two new phases: TiB_2 and graphite. With addition of 10 wt% of Ni (Figure 32), it is predicted the same behaviour in relation to the formation of a Ni liquid phase (~1027 ºC) and reaction to form Ni_3B when cooling (see section 4.1.2), but also the formation of graphite and absence of TiB_2.
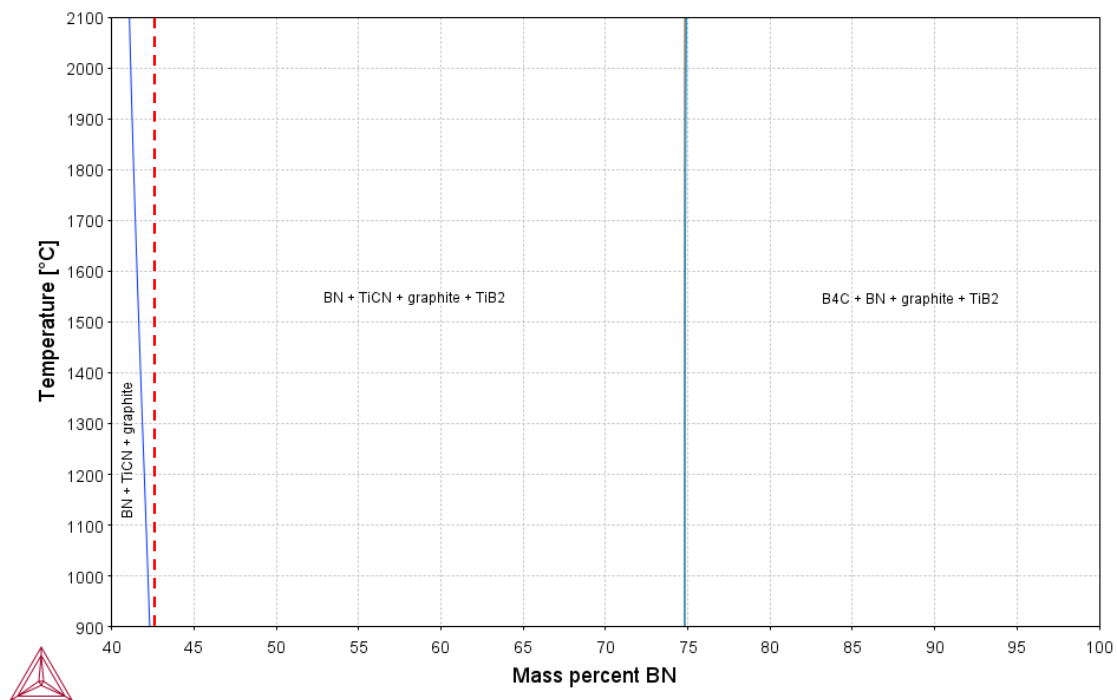
Figure 31- Predicted phase diagram for the BN-TiCN system. The dashed line corresponds to composition 3.
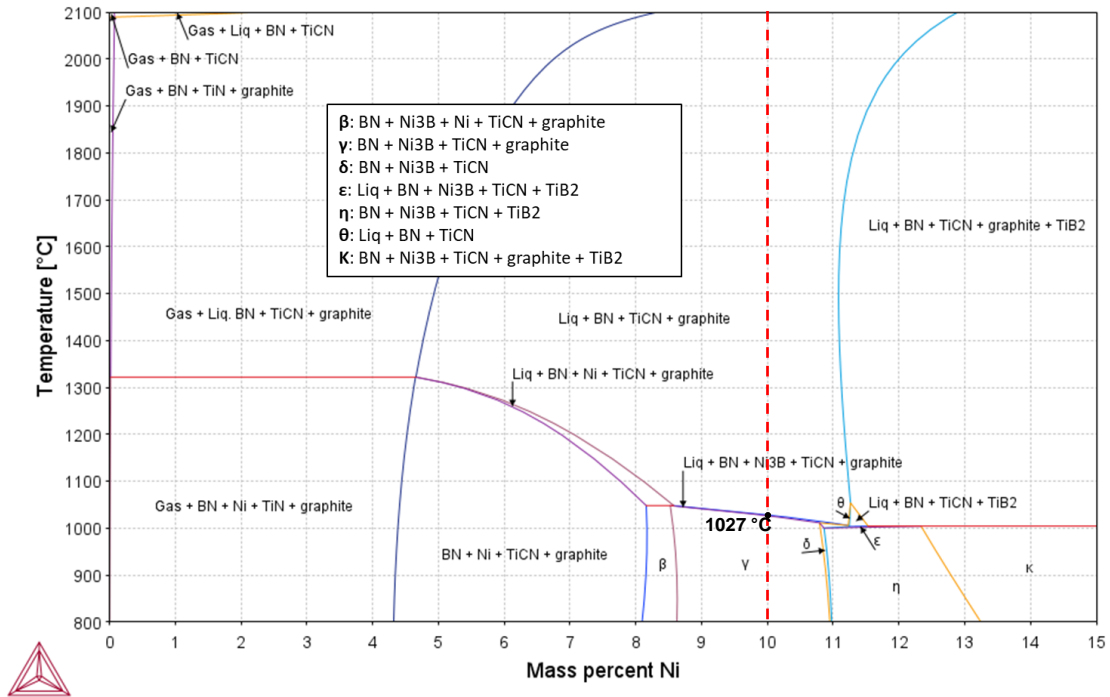
Figure 32- Predicted phase diagram for the BN-TiCN-Ni system. The dashed line corresponds to composition 4.

4.2.3 Colloidal characterization of cBN

To be able to uniformly disperse the various constituents of a mixture in a liquid medium, it is necessary to know the powders behaviour in such medium. The behaviour of TiCN and Ni powders was already studied in previous works concluding that an amount of long Polyethylenimine (long PEI) of 0.5 and 7% respectively is enough, but for cBN it was necessary to perform this characterization [96,97]. Figure 33 shows the variation of Zeta potential of the cBN powder in function of pH and the respective particle size. It is observed that for very acid pH or basic the zeta potential increases and even becoming positive for pH = 2, as for pH around neutral the potential decreases to almost -60mV, while the particle size follows this behaviour, increasing with increasing Zeta potential. Since the particle size varies between 1 – 2 μm, which is the size of this powder in Table 5, it is reasonable to consider that the pH does not significantly affect the powder behaviour. Hence, agglomerates do not form, but powder dispersion doesn't either.
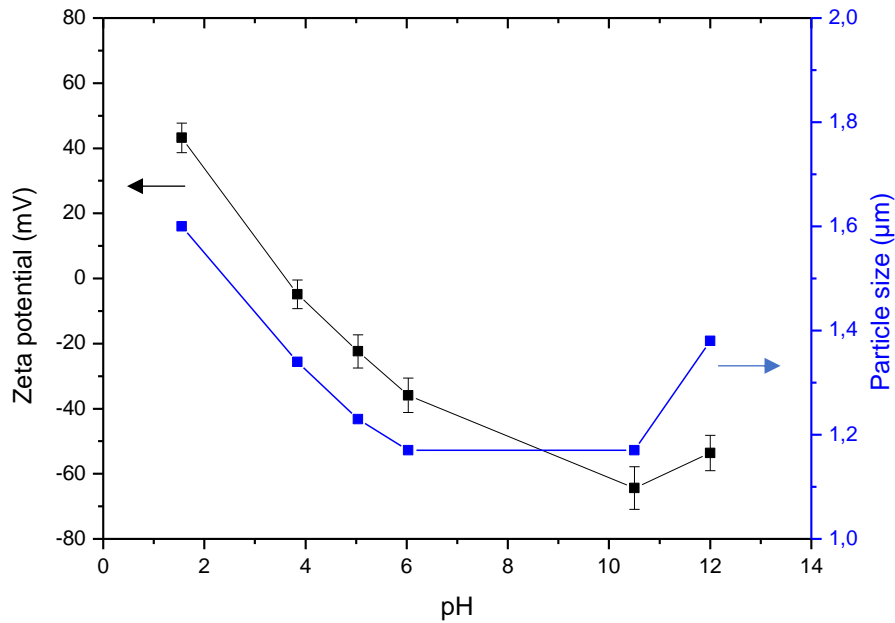
Figure 33- Variation of cBN powder Zeta potential and particle size in function of medium pH.

Since a polymer (polyelectrolyte) is intended to be used as dispersant to prepare the colloid, it was necessary to also characterize the cBN powder behaviour with the dispersant. The pH was maintained around 9, due to Ni dissolving for pH < 8, and for pH > 10 the polymeric chains of the dispersant shrink which decreases its ability to deagglomerate the powders [98]. Results are shown in Figure 34 and Figure 35 for short PEI and long PEI, respectively. Addition of short PEI increases the zeta potential to over 60 mV at 0.5 wt% which is maintained up to 2 wt%, the particle size oscillates around 1.2 μm in size. As for long PEI, the Zeta potential immediately increases to values above 30 mV and maintains stable for all the amounts, with a slightly greater increase at 6 wt.%. The particle size decreases with the added polymer up to 1 wt.% where it reaches its minimum and stays around 1.2 μm. The most indicated dispersant is the one that can reach stable Zeta potential with less amount of polymer added, and for short PEI it is necessary 0.5 wt.%, while for long PEI it is necessary 0.25 wt.% although it can increase the powder dispersion up to 1 wt.%. It was also noted that after preparing the suspensions a pH adjustment was necessary when using short PEI, while no adjustment was necessary for the long PEI.
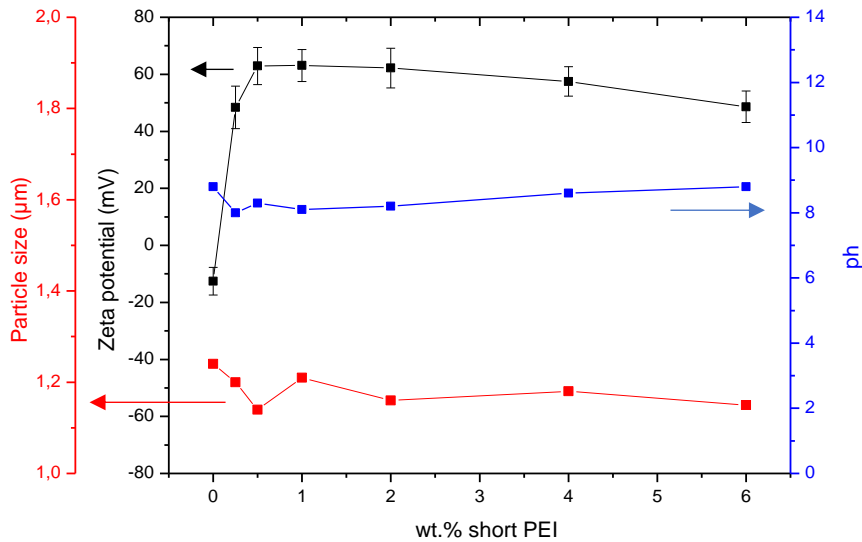
Figure 34- Variation of Zeta potential and particle size in function of short PEI addition to the cBN powder, maintaining a pH around 9.
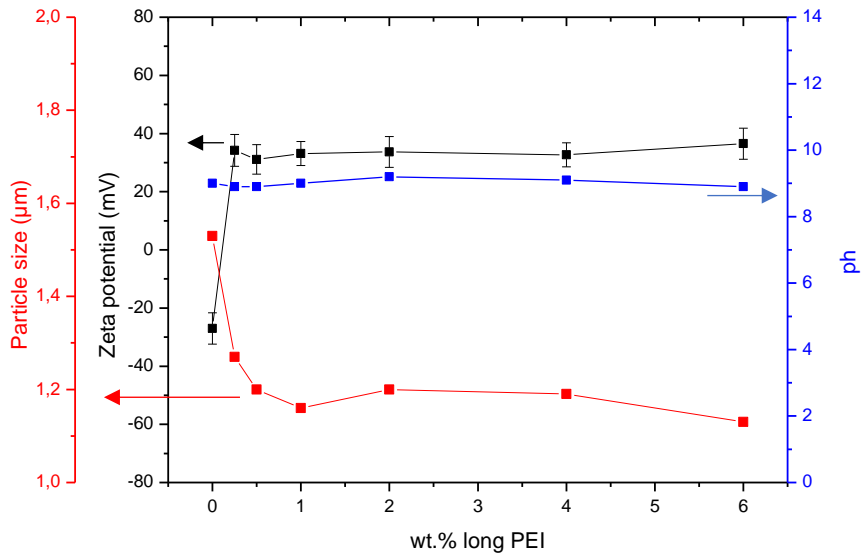
Figure 35- Variation of Zeta potential and particle size in function of long PEI addition to the of cBN powder, maintaining a pH around 9.

4.2.4 Preparation and initial characterization of the compositions

When following the colloidal processing method for the preparation of composition 4 as described in section 3.2.1, both short and long PEI were individually used. During the preparation it was observed that, while mixing the powders with short PEI in the liquid medium, the viscosity of the slurry increased drastically to the point that mechanical mixing would be impeded by further addition of powder. In comparison, with long PEI all the powders were successfully added in the proportionated amounts without changing the viscosity too much, meaning that it was possible to achieve a higher solid concentration on the slurry. For this reason, the use of short PEI was discarded, and long PEI was the dispersant used to prepare both compositions.

Figure 36 shows the morphology of compositions 3 and 4, prepared using the colloidal processing technique. In both cases the distribution of the particles is homogeneous, but none of the constituent's particles are distinguishable from one another, in terms of morphology. The diffractogram in Figure 37 of composition 4 prepared by colloidal processing technique confirms the presence of the already expected phases: cBN, TiCN and Ni.
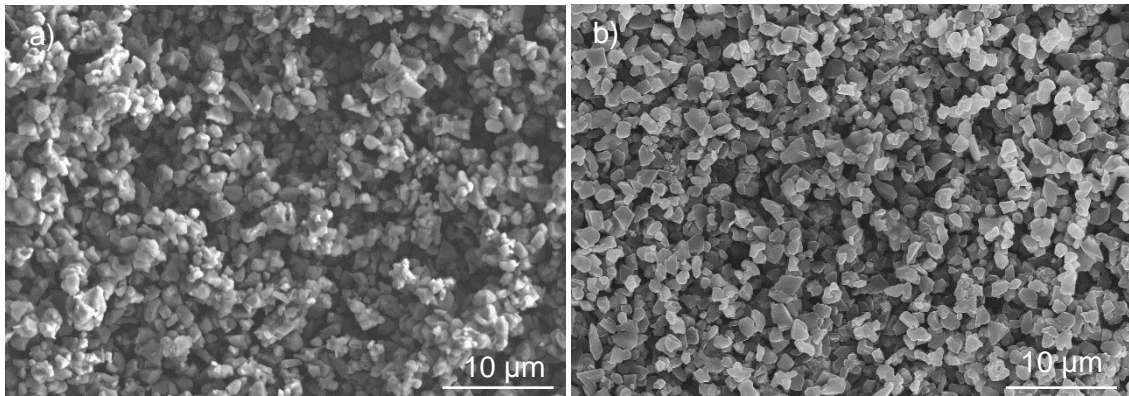
Figure 36- Microstructure of the prepared compositions: a) composition 3 and b) composition 4 prepared by colloidal processing (acquired using the SEM Hitachi model S-4700).
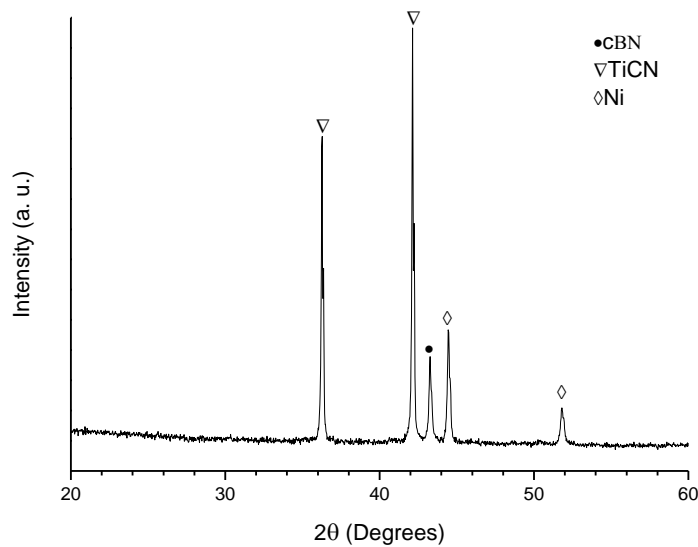
Figure 37- XRD diffractogram of the mixed composition 4 by colloidal processing technique.

4.2.5 SPS: Effect of the Nickel addition

Figure 38 shows the shrinkage and shrinkage rate of composition 3 and 4 prepared by the colloidal processing method, the first without Ni and the other with 5 vol% Ni (10 wt%). In both cases, the same two stages can be identified in the shrinkage curve of Figure 38-a: stage I where a reduced shrinkage up to ~1200 ºC can be observed in both compositions; and stage II where a larger shrinkage occurs after 1200 ºC, being more pronounced in the composition with Ni, and therefore having a higher shrinkage rate. This significantly higher shrinkage rate of the composition with 5 vol% Ni at 1200 ºC is off from the predicted temperature of 1027 ºC for formation of liquid phase (Figure

32). No expansion associated with the BN phase transformation to hexagonal form was observed for temperatures up to 2000 ºC although in the composition without Ni it can be seen a decrease of the shrinkage rate starting from 1700 ºC. Being this the upper limit of the calculated temperature for the transformation to occur, it may suggest that the transformation still occurred but less expressively that what was observed previously (section 4.1.4).

a)

b)
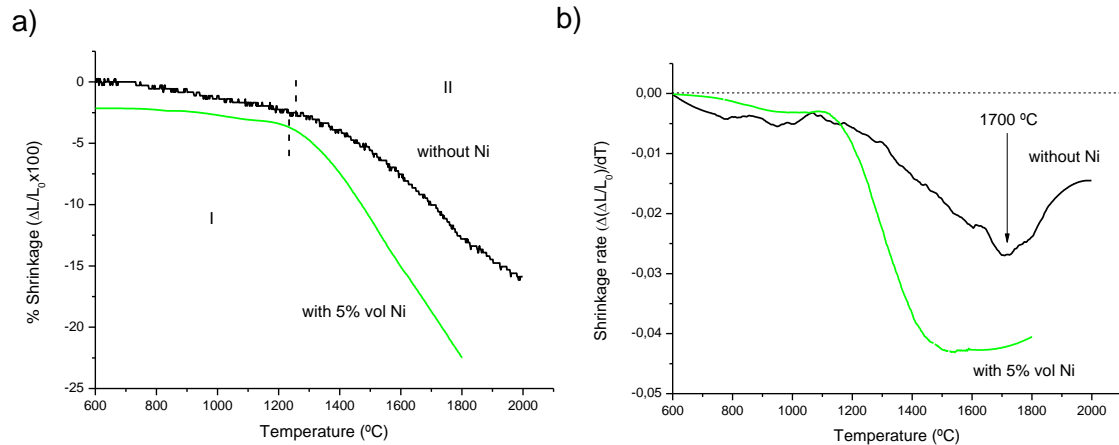
Figure 38- Shrinkage (a) and shrinkage rate (b) of composition 3 (without Ni) and composition 4 (with Ni), both processed by CP, in function of the temperature using SPS.

The XRD patterns of the sintered samples presented in Figure 39, indicates the following statements: (i) as previously observed (section 4.1.4), no significant difference was observed in the TiCN phase; (ii) for both compositions, all predicted phases in Figure 31 and Figure 32 were observed, BN, TiCN and TiB_2 phases for the composition 3 (cBN+TiCN) and BN, TiCN, TiB_2 and Ni_3B for composition 4 (cBN+TiCN+Ni), except graphite which in both cases was not detected; (iii) no cBN was detected at 2000 ºC (composition 3) while a very small peak was detected at 1800 ºC (composition 4). This last one indicates that the BN phase transformation did occur despite not being recorded the associated volume expansion in the dilatometric curves of Figure 38.

Comparing the Powder Diffraction Files of hBN (ICDD 04-015-2797) and graphite (ICDD 04-014-0362) phases, it is indicated that the characteristic most intense peaks of each phase are at a 2θ angle of 26.6º and 26.3 respectively, while the other characteristic peaks have a relative intensity lower than 20% of the main ones. This means that the identification by XRD technique of each phase will be difficult due to mostly being just one peak at that angle. Additionally, the peak at 26.6º is very broad and can hide the graphite phase peak, if existing in small amounts.
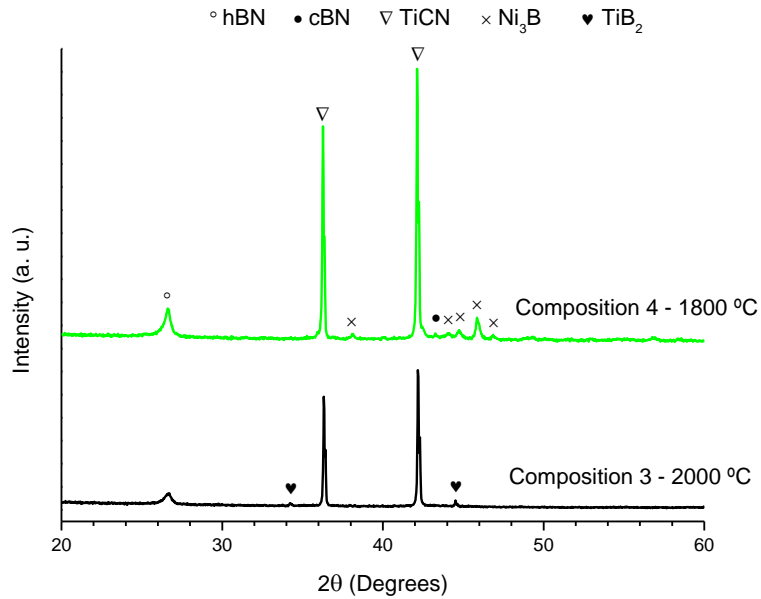
Figure 39- XRD patterns of compositions 3 and 4, both processed by CP method, sintered at 2000 ºC and 1800 ºC by SPS respectively.

4.2.6 SPS: effect of the processing method and temperature variation

Figure 40 shows the shrinkage and shrinkage rate of composition 4, according to the two preparation methods: Ball Milling (BM) or Colloidal Processing (CP). The same two sintering stages are observed (I and II), with the BM method having greater shrinkage in stage I in relation to the CP method and maintaining this stage I up to higher temperature (~1400 ºC) than the CP method (~1200 ºC). As for stage II, both methods have similar sintering behaviour with the BM method achieving a greater shrinkage overall. No apparent expansion was observed.
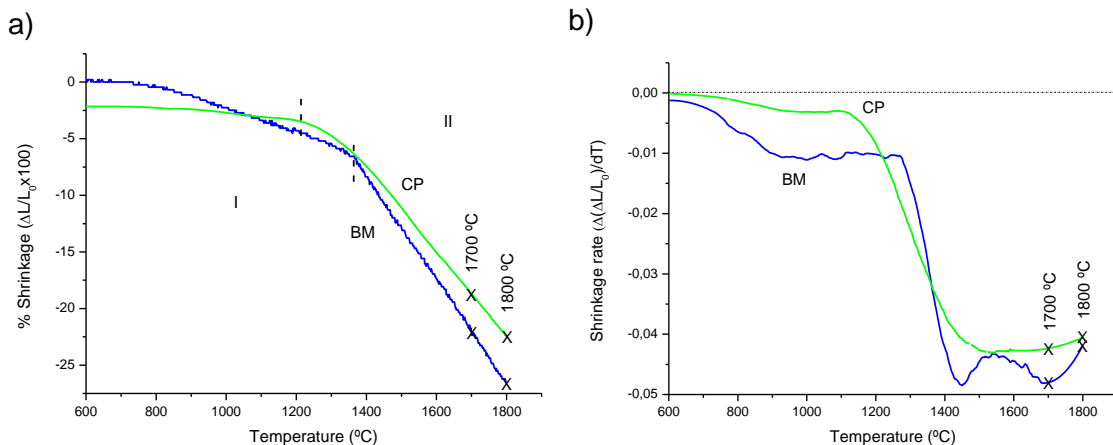
Figure 40- Shrinkage (a) and shrinkage rate (b) of composition 4 samples processed by BM or CP and sintered at 1700 – 1800 ºC by SPS.

The apparent density and open porosity of the samples in function of the sintering temperature are shown in Figure 41. The samples processed by the BM method have greater shrinkage overall and already achieved 0% of open porosity at 1700 ºC, yet continuing to show a considerable shrinkage after 1700 ºC despite not having a

significant change in open porosity when increasing to 1800 ºC, possibly due to the removal of close porosity since its apparent density had a slight increase. As for the samples processed by the CP method, they shown a smaller shrinkage overall, having still 10% of open porosity at 1700 ºC, but achieve 0% when sintered at 1800 ºC coinciding with the same shrinkage and open porosity of the sample by BM at 1700 ºC. A small decrease of apparent density is observed in the sample processed by CP, since the formation of hBN was observed at 1800 ºC in Figure 39, which is probably connected to the decrease in density and the elimination of open porosity with increasing temperature.
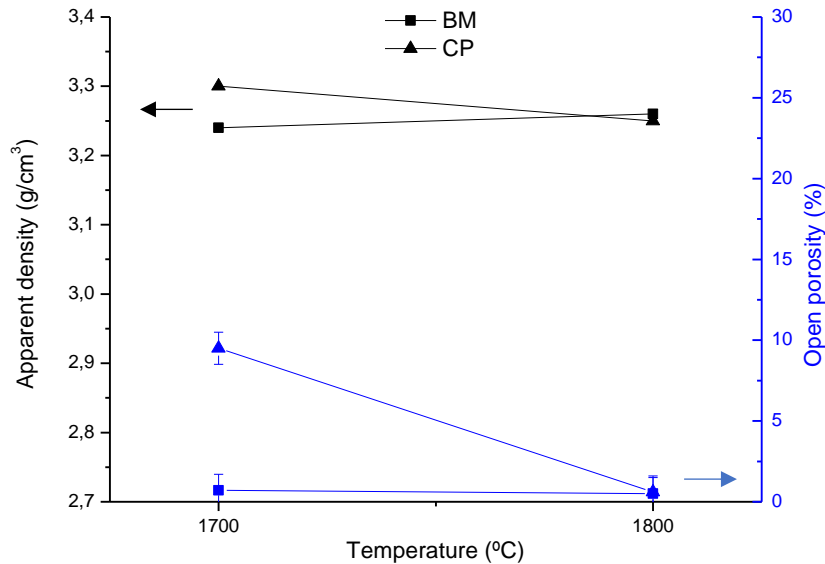
Figure 41- Apparent density and open porosity of the samples from composition 4 where it was variated the processing method (BM and CP) and SPS sintering temperature (1700 – 1800 ºC).

In Figure 42 it is shown the XRD profiles of composition 4 green powder and processed samples (BM and CP) sintered by SPS between 1700 – 1800 ºC. The same phases are identified in the XRD patterns as in Figure 42, being summarized in Table 14 the experimentally detected phases together with the predicted ones in the phase diagrams of Figure 32. As for BN, a significative part of the cubic phase had already transformed into the hexagonal form at 1700 ºC, with a greater extension when increasing to 1800 ºC. Nonetheless, some cubic phase is still detected at 1800 ºC even after 10 minutes of dwell time, meaning that the full transformation threshold was delayed to higher temperatures than the calculated temperature of transformation of 1320 ± 380 ºC. The similarity of the XRD patterns (Figure 42), along with roughly the same hBN phase amounts determined (Table 14), indicates that no significant difference occurred from the processing technique used, either BM or CP, in terms of crystallographic phases.
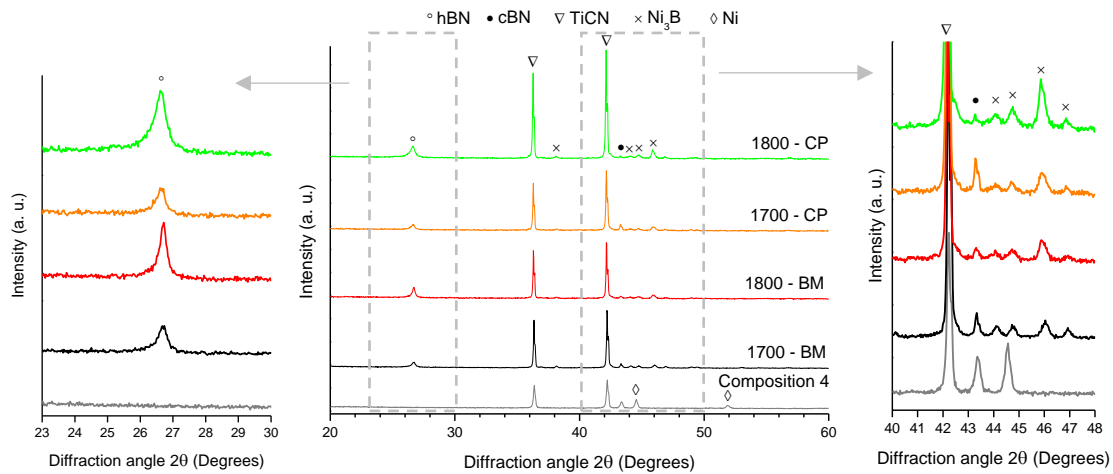
Figure 42- XRD diffractograms of composition 4 as-mixed and sintered by SPS at 1700 – 1800 ºC with ball milling (BM) or colloidal processing (CP) as mixing technique.

Table 14- Comparison of initial, predicted and detected phases of composition 4 sintered samples.

Preparation method and Sintering samples (ºC)	Predicted phases** (Thermo-Calc)	Detected phases (XRD)	Amount hBN phase (%)***
*	-	cBN+TiCN+Ni	0
BM – 1700 ºC	BN+TiCN+Ni$_3$B+graphite	cBN+hBN+TiCN+Ni$_3$B	74
BM – 1800 ºC			91
CP – 1700 ºC			70
CP – 1800 ºC			95

*as-prepared composition 4; **Considered at below 1000 ºC; ***Based on the net area of XRD peaks of hBN and cBN respectively.

4.2.7 Microstructural characterization

To evaluate the capability of the processing methods in dispersing and achieving a homogeneous distribution of the composition's constituents, SEM images of the microstructures are shown in Figure 43. In Figure 43-a (composition 4 by BM) various heterogeneities of the order of 100 µm are observed, while in Figure 43-b the same kind of defects are observed but in smaller regions, around 25 µm. Overall, there were some heterogeneities in the microstructures that the mixing techniques were not capable to eliminate, but the colloidal processing achieved a better uniformity than the ball milling method.

48
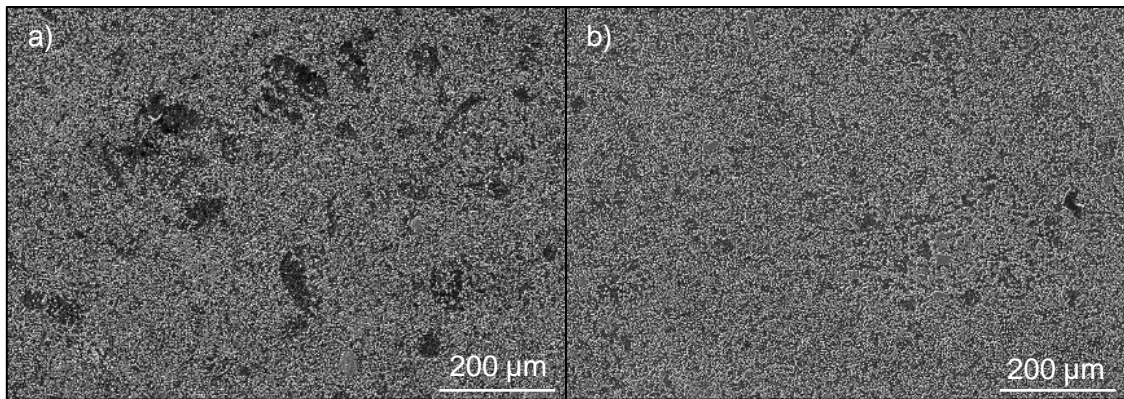
Figure 43- SEM microstructures of composition 4 by (a) BM and (b) CP.

A comparison of the microstructures of all four sintered samples in Figure 44 shows the morphology of the composite's constituents and existing defects. In all samples two different structures can be seen, several white color particles in a dark grey background, which considering the phases detected by XRD in Figure 39 and the effect of the respective phase density (Table 10) on the SEM imaging, can be attributed to TiCN+Ni$_3$B and BN respectively. Besides, 3 types of defects can be identified; (i) dark spots with irregular shape; (ii) white color particles with undefined shape and rough surface; and (iii) slightly larger agglomerates than the general particles size, with a polished surface. The first type of defects (i) is more predominant and have larger size for the samples prepared by BM. A more detailed look (Figure 45) reveals that they consist in absence of material, possibly due to removal of some particle like shape structures (i. e. agglomerated cBN or TiCN particles), while a chemical analysis by EDS revealed the presence of only Ni on this regions (B detected is not representative since this element is to light for an acceptable measurement) The second type of defects (ii), although not shown in Figure 44, is a defect only present in significant amounts on samples prepared by BM. These regions possess a quite significant size (~200 μm in length on Figure 46) and appear to be formed by a phase with higher density than the TiCN (whiter color than the TiCN grains around this one). EDS data from the defect indicates that itis formed by a phase containing Ti and Ni elements, Figure 46. When acquiring EDS maps of the elements (Ti, B, Ni) to see their distribution (Figure 46-c throw d), it did not indicate the presence any of the elements in the defect area. These leads to no conclusion about what exactly are these defects. It is possible than these structures, when removed, leave a hole on the surface resulting in the first type of defect (i). The third type of defects (iii) observed are present in samples prepared by both BM and CP methods, being more predominant in the ones prepared by BM. On a closer look (Figure 45), they consist of grains of TiCN bound together by the Ni$_3$B phase, identified by the detection of Ti and Ni respectively, and the polishing exposed this consolidated zone. Then, these zones are not defects, but places were the binders successfully consolidated the material although it appears that the BN phase was left out.
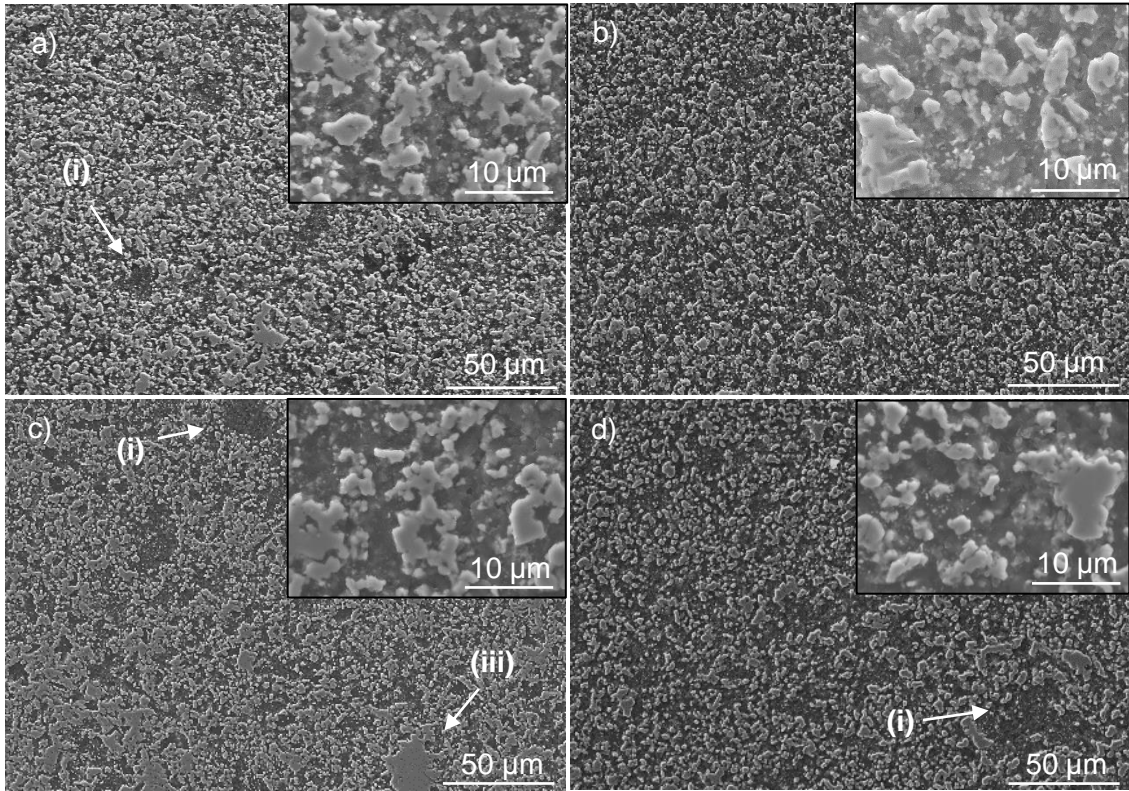
Figure 44- Microstructure morphology of the four sintered samples of composition 4: (a) BM - 1700 ºC, (b) CP – 1700 ºC, (c) BM – 1800 ºC and (d) CP – 1800 ºC.
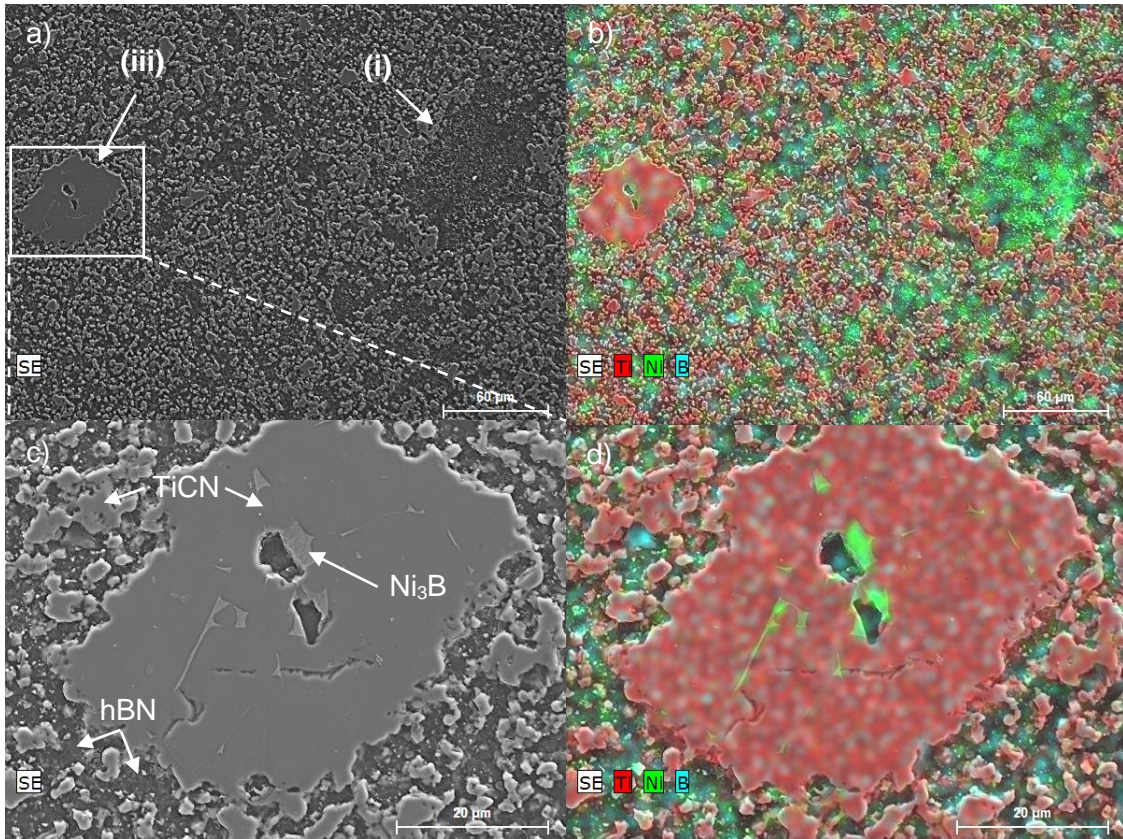
Figure 45- a) SEM imaging of the microstructure of a sample from composition 4 by CP sintered at 1800 ºC and b) EDS mapping of Ti, B and Ni elements, where it was focussed

on (c) another type of defect on its microstructure and its respective d) EDS mapping of Ti, B and Ni elements.
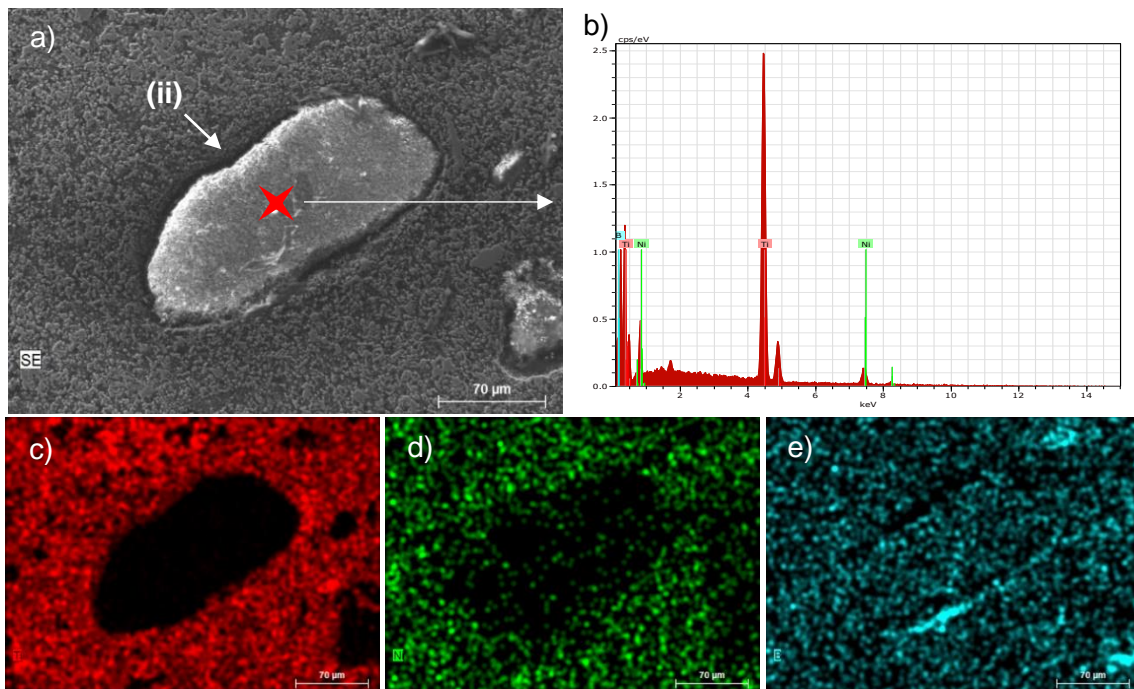
Figure 46- a) SEM imaging of the microstructure of a sample from composition 4 by BM sintered at 1700 ºC, focused on a defect were a (b) EDS measurement was performed on a single point (marked as a red star), and b) EDS mapping of c) Ti, d) Ni and e) B elements.

Summarizing the results, high densifications were also achieved with this composite (39 wt% cBN). Despite still having an extensive BN phase transformation to hexagonal form, a significant amount of cubic phase was still present in the composite even at sintering temperatures of 1800 ºC. The presence of a graphite phase was not possible to confirm due to overlapping peaks with the hBN phase, which is crucial since the phase diagram indicates it as a stable phase and the composite was sintered in a graphite mould. Being a soft phase, the graphite phase is not desirable. In relation to powders homogeneity, both ball milling and colloidal processing here insufficient to achieve a homogeneous distribution, resulting in several defects on the microstructure of the sintered compositions. Nonetheless, the colloidal processing technique reached a more uniform dispersion than the ball milling method.

Chapter 5- Conclusions

In conclusion of this work, being divided in two distinct parts focused on studying the thermal reactivity of cBN-TiCN-Ni composites and the densification of these ones by Spark Plasma Sintering respectively, the following conclusions were summarized.

- **Thermo-calc software as a tool**

The Thermo-calc software proved to be a powerful tool in determining the equilibrium phases of the intended materials systems, since the predicted phases were in line with the experimentally confirmed ones. Nonetheless it possesses some limitations that were faced in this work, namely the impossibility of calculating phase transformations at high pressures and the presence of only BN in the hexagonal form in the database. Such data would be valuable for a deeper understanding of the phase transformation of BN.

- **Thermal reactivity of the system and phases formed**

The Ni phase is expected to form a liquid phase, which is predicted to be capable of dissolving B elements and promoting the formation of other more stable phases, namely Ni_3B. It was verified the instability of the Ti_2N phase in these systems, yet the possibility of formation of graphite could not be confirmed or denied being its formation detrimental for the hardness of the composite.

- **BN phase transformation**

It was not possible to prevent or delay the beginning of BN phase transformation from cubic to hexagonal by SPS with up to 60 MPa, since this one was observed to form as low as 1400 ⁰C, while the majority of the transformation occurred and completely transformed at 1700 ⁰C. Decreasing the grain size of cBN in the composite lead to a delay in the transformation extension, allowing to still be detected cBN at 1800 ⁰C. The morphologic difference between the cBN and hBN phases was observed by SEM imaging. No BN phase other than cubic and hexagonal was observed to form despite the non-equilibrium conditions applied by the SPS technique, but an amorphous phase was detected by XRD at 1700 ⁰C

- **Colloidal characterization of micrometric cBN powder**

The micrometric cBN powder was observed to not agglomerate by changing the pH of the medium, and when interacting with the dispersant (Polyethylenimine) it was shown that 0,5% wt. and 0,25% wt. of short PEI and long PEI respectively is enough to achieve a good dispersion of the ceramic particles.

- **Powders mixing process**

In a comparison between the Ball Milling and the Colloidal Processing method for achieving a uniform dispersion of the powder's particles, the colloidal processing achieved a better distribution by showing less defects in the SEM microstructures but reached slightly lower densifications for the same temperature. In relation of chemical phases, no different between the two was observed.

- **Densification of cBN-TiCN-Ni based composited by SPS**

The addition of Ni aided the sintering of the cBN-TiCN based composite by increasing the total shrinkage during sintering, but it did not make possible the total densification of the composite bellow the 1700 ⁰C, temperature at which most of the phase transformation occurred. Decreasing the particle size of the cBN powder resulted in a delay of complete BN phase transformation to higher temperatures. With the formation of consolidated areas of TiCN+Ni_3B on the microstructure, it was evident that it is

possible to consolidate the cBN-TiCN-Ni composite, although consolidation with the BN particles is still lacking.

Chapter 6- Future work

As future work, there are several routes that can be followed to achieve the main objective of fully densified PcBN with good mechanical properties to be used as a cutting tool. These ones consist in:

- **Improvement of the colloidal mixing**

The colloidal process could be further improved by testing longer mixing times of 2, 4, 6, 8, 10 and 12 h. Had been used 1 hour may not be enough to reach the maximum homogeneity possible by this technique.

- **Decrease the amount of cBN incorporated**

Incorporating less cBN would make possible to sinter the composite at temperatures below the threshold temperature of 1700 ºC, at which the majority of the BN phase transformation occurs.

- **Decrease the cBN powder particle size**

Results suggest that decreasing the cBN particle size leads to a delay in the total phase transformation (for a 57 µm particle size the cBN completely transformed at 1700 ºC, as for a 1,2 µm particle size powder there was still a significant amount of cBN at 1800 ºC). It could be possible that decreasing the particle size even further may give a wider temperature range for sintering the composite retaining the cubic BN phase, although it will pose additional challenges in dispersing since the powder particle will enter in the nanometre range.

- **Investigation of other transient liquid phases**

The densification of PcBN is promoted by addition of phases that can melt and form a liquid phase at sintering temperatures. At the same time, these ones could dissolve some part of the system constituents and precipitate hard phases that would contribute for the hardness of the composite. The formation of soft phases such as hBN or graphite must be avoided.

When a fully consolidated PcBN material with good mechanical properties is finally achieved, the next step should be testing the composite as a cutting piece, evaluating its cutting conditions and tool life against various types of work piece materials.

References

[1] A. Hosseini, H.A. Kishawy, Cutting Tool Materials and Tool Wear, in: J.P. Davim (Ed.), 1st ed., Springer, 2014: pp. 31–56. https://doi.org/10.1007/978-3-662-43902-9_2.

[2] Y. Le Godec, A. Courac, V.L. Solozhenko, High-pressure synthesis of superhard and ultrahard materials, J. Appl. Phys. 126 (2019) 151102. https://doi.org/10.1063/1.5111321.

[3] R. Riedel, Handbook of Ceramic Hard Materials, Wiley, 2000. https://doi.org/10.1002/9783527618217.

[4] G.E. Spriggs, 13 Hard Materials, in: P. Beiss, R. Ruthardt, H. Warlimont (Eds.), Mater. · Powder Metall. Data. Refract. Hard Intermet. Mater., Springer, 2002: p. 193.

[5] S.N. Monteiro, A.L.D. Skury, M.G. De Azevedo, G.S. Bobrovnitchii, Cubic boron nitride competing with diamond as a superhard engineering material - An overview, J. Mater. Res. Technol. 2 (2013) 68–74. https://doi.org/10.1016/j.jmrt.2013.03.004.

[6] T. Taniguchi, M. Akaishi, S. Yamaoka, Sintering of cubic boron nitride without additives at 7.7 GPa and above 2000°C, J. Mater. Res. 14 (1999) 162–169. https://doi.org/10.1557/JMR.1999.0024.

[7] I.D. Marinescu, W.B. Rowe, B. Dimitrov, I. Inasaki, Abrasives and Abrasive Tools, in: Tribol. Abras. Mach. Process., Elsevier, 2004: pp. 369–455. https://doi.org/10.1016/B978-081551490-9.50012-8.

[8] C.A. Harper, HANDBOOK OF CERAMICS, GLASSES, AND DIAMONDS, 2001.

[9] C.J.H. Wort, Applications for superhard and ultra-hard materials, in: Microstruct. Correl. Hard, Superhard, Ultrahard Mater., Springer, Cham, 2016: pp. 25–74. https://doi.org/10.1007/978-3-319-29291-5_2.

[10] J. Zhang, R. Tu, T. Goto, Cubic boron nitride-containing ceramic matrix composites for cutting tools, in: Adv. Ceram. Matrix Compos., Woodhead Publishing, 2014: pp. 570–586. https://doi.org/10.1533/9780857098825.3.570.

[11] ISO - 513, ISO 513- Classification and application of hard cutting materials for metal removal with defined cutting edges — Designation of the main groups and groups of application Classification, 2012. https://www.iso.org/standard/59932.html (accessed August 26, 2021).

[12] M. Ociepa, M. Jenek, E. Feldshtein, On the Wear Comparative Analysis of Cutting Tools Made of Composite Materials Based on Polycrystalline Cubic Boron Nitride when Finish Turning of AISI D2 (EN X153CrMoV12) Steel, J. Superhard Mater. 40 (2018) 396–401. https://doi.org/10.3103/S1063457618060059.

[13] J.A. Arsecularatne, L.C. Zhang, C. Montross, Wear and tool life of tungsten carbide, PCBN and PCD cutting tools, Int. J. Mach. Tools Manuf. 46 (2006) 482–491. https://doi.org/10.1016/j.ijmachtools.2005.07.015.

[14] Palbit S.A, General Catalogue - Metric, (n.d.) 462–498.

[15] R. M'Saoubi, M.P. Johansson, J.M. Andersson, Wear mechanisms of PVD-coated PCBN cutting tools, Wear. 302 (2013) 1219–1229. https://doi.org/10.1016/j.wear.2013.01.074.

[16] V.L. Solozhenko, V.Z. Turkevich, W.B. Holzapfel, Refined Phase Diagram of Boron Nitride, J. Phys. Chem. B. 103 (1999) 2903–2905.

https://doi.org/10.1021/jp984682c.

[17]   P. Klimczyk, P. Wyżga, J. Cyboroń, J. Laszkiewicz-Łukasik, M. Podsiadło, S. Cygan, L. Jaworska, Phase stability and mechanical properties of Al2O3-cBN composites prepared via spark plasma sintering, Diam. Relat. Mater. 104 (2020). https://doi.org/10.1016/j.diamond.2020.107762.

[18]   Y. Yuan, X. Cheng, R. Chang, T. Li, J. Zang, Y. Wang, Y. Yu, J. Lu, X. Xu, Reactive sintering cBN-Ti-Al composites by spark plasma sintering, Diam. Relat. Mater. 69 (2016) 138–143. https://doi.org/10.1016/j.diamond.2016.08.009.

[19]   O. Guillon, J. Gonzalez-Julian, B. Dargatz, T. Kessel, G. Schierning, J. Räthel, M. Herrmann, Field-assisted sintering technology/spark plasma sintering: Mechanisms, materials, and technology developments, Adv. Eng. Mater. 16 (2014) 830–849. https://doi.org/10.1002/adem.201300409.

[20]   P. Cavaliere, B. Sadeghi, A. Shabani, Spark Plasma Sintering: Process Fundamentals, in: Spark Plasma Sinter. Mater., Springer, Cham, 2019: pp. 3–20. https://doi.org/10.1007/978-3-030-05327-7_1.

[21]   S. Rudolph, Boron nitride (BN), Am. Ceram. Soc. Bull. 79 (2000) 50.

[22]   L.F. Dobrzhinetskaya, R. Wirth, J. Yang, I.D. Hutcheon, P.K. Weber, H.W. Green, High-pressure highly reduced nitrides and oxides from chromitite of a Tibetan ophiolite, Proc. Natl. Acad. Sci. U. S. A. 106 (2009) 19233–19238. https://doi.org/10.1073/pnas.0905514106.

[23]   L.F. Dobrzhinetskaya, R. Wirth, J. Yang, H.W. Green, I.D. Hutcheon, P.K. Weber, E.S. Grew, Qingsongite, natural cubic boron nitride: The first boron mineral from the Earth's mantle, Am. Mineral. 99 (2014) 764–772. https://doi.org/10.2138/am.2014.4714.

[24]   N. Izyumskaya, D.O. Demchenko, S. Das, Ü. Özgür, V. Avrutin, H. Morkoç, Recent Development of Boron Nitride towards Electronic Applications, Adv. Electron. Mater. 3 (2017) 1600485. https://doi.org/10.1002/aelm.201600485.

[25]   T. Taniguchi, Materials science research of boron nitride obtained at high pressure and high temperature, J. Ceram. Soc. Japan. 128 (2020) 620–626. https://doi.org/10.2109/jcersj2.20116.

[26]   R. Haubner, M. Wilhelm, R. Weissenbacher, B. Lux, Boron Nitrides — Properties, Synthesis and Applications, in: Springer, Berlin, Heidelberg, 2002: pp. 1–45. https://doi.org/10.1007/3-540-45623-6_1.

[27]   L. Vel, G. Demazeau, J. Etourneau, Cubic boron nitride: synthesis, physicochemical properties and applications, Mater. Sci. Eng. B. 10 (1991) 149–164. https://doi.org/10.1016/0921-5107(91)90121-B.

[28]   J. Huang, Y.T. Zhu, Advances in the synthesis and characterization of boron nitride, Diffus. Defect Data. Pt A Defect Diffus. Forum. 186–187 (2000) 1–32. https://doi.org/10.4028/www.scientific.net/ddf.186-187.1.

[29]   J. Greim, K.A. Schwetz, Boron Carbide, Boron Nitride, and Metal Borides, in: Ullmann's Encycl. Ind. Chem., John Wiley & Sons, Ltd, 2006. https://doi.org/10.1002/14356007.a04_295.pub2.

[30]   A. Mujica, A. Rubio, A. Muñoz, R.J. Needs, High-pressure phases of group-IV, III-V, and II-VI compounds, Rev. Mod. Phys. 75 (2003) 863–912. https://doi.org/10.1103/RevModPhys.75.863.

[31]   Y. Li, Y. Shen, C. Gong, B. Li, H. Huang, K. Ji, Synthesis and characterization of boron nitride powder, in: AIP Conf. Proc., AIP Publishing LLC AIP Publishing, 2018: p. 020007. https://doi.org/10.1063/1.5041102.

[32]   B. Ertug, Powder Preparation, Properties and Industrial Applications of Hexagonal Boron Nitride, in: Sinter. Appl., IntechOpen, 2013. https://doi.org/10.5772/53325.

[33]   M.I. Petrescu, M.G. Balint, Structure and properties modifications in boron nitride. Part I: Direct polymorphic transformations mechanisms, UPB Sci. Bull. Ser. B Chem. Mater. Sci. 69 (2007) 35–42. https://www.researchgate.net/publication/261853742_Structure_and_properties_modifications_in_boron_nitride_Part_I_Direct_polymorphic_transformations_mechanisms (accessed August 26, 2021).

[34]   M. Moret, A. Rousseau, P. Valvin, S. Sharma, L. Souqui, H. Pedersen, H. Högberg, G. Cassabois, J. Li, J.H. Edgar, B. Gil, Rhombohedral and turbostratic boron nitride: X-ray diffraction and photoluminescence signatures, Appl. Phys. Lett. 119 (2021). https://doi.org/10.1063/5.0076424.

[35]   S. Roy, X. Zhang, A.B. Puthirath, A. Meiyazhagan, S. Bhattacharyya, M.M. Rahman, G. Babu, S. Susarla, S.K. Saju, M.K. Tran, L.M. Sassi, M.A.S.R. Saadi, J. Lai, O. Sahin, S.M. Sajadi, B. Dharmarajan, D. Salpekar, N. Chakingal, A. Baburaj, X. Shuai, A. Adumbumkulath, K.A. Miller, J.M. Gayle, A. Ajnsztajn, T. Prasankumar, V.V.J. Harikrishnan, V. Ojha, H. Kannan, A.Z. Khater, Z. Zhu, S.A. Iyengar, P.A. da S. Autreto, E.F. Oliveira, G. Gao, A.G. Birdwell, M.R. Neupane, T.G. Ivanov, J. Taha-Tijerina, R.M. Yadav, S. Arepalli, R. Vajtai, P.M. Ajayan, Structure, Properties and Applications of Two-Dimensional Hexagonal Boron Nitride, Adv. Mater. 33 (2021). https://doi.org/10.1002/adma.202101589.

[36]   A. Janotti, S.H. Wei, D.J. Singh, First-principles study of the stability of BN and C, Phys. Rev. B - Condens. Matter Mater. Phys. 64 (2001). https://doi.org/10.1103/PhysRevB.64.174107.

[37]   Z. Lin, Y. Liu, K.S. Moon, C.P. Wong, Enhanced thermal transport of hexagonal boron nitride filled polymer composite by magnetic field-assisted alignment, in: Proc. - Electron. Components Technol. Conf., 2013: pp. 1692–1696. https://doi.org/10.1109/ECTC.2013.6575801.

[38]   G. Diamond, cBN/cBN micron, (n.d.). https://www.global-diamond.co.jp/en/product/en_cbn.htm (accessed June 3, 2022).

[39]   G. Demazeau, High pressure diamond and cubic boron nitride synthesis, Diam. Relat. Mater. 4 (1995) 284–287. https://doi.org/10.1016/0925-9635(94)05281-6.

[40]   V.L. Solozhenko, O.O. Kurakevych, Y. Le Godec, Creation of nanostuctures by extreme conditions: High-pressure synthesis of ultrahard nanocrystalline cubic boron nitride, Adv. Mater. 24 (2012) 1540–1544. https://doi.org/10.1002/adma.201104361.

[41]   X. Zhang, J. Meng, Recent progress of boron nitrides, in: Ultra-Wide Bandgap Semicond. Mater., Elsevier, 2019: pp. 347–419. https://doi.org/10.1016/b978-0-12-815468-7.00004-4.

[42]   V.L. Solozhenko, D. Häusermann, M. Mezouar, M. Kunz, Equation of state of wurtzitic boron nitride to 66 GPa, Appl. Phys. Lett. 72 (1998) 1691–1693. https://doi.org/10.1063/1.121186.

[43]   S. Alkoy, C. Toy, T. Gönül, A. Tekin, Crystallization behavior and characterization of turbostratic boron nitride, J. Eur. Ceram. Soc. 17 (1997) 1415–1422.

https://doi.org/10.1016/s0955-2219(97)00040-x.

[44]   O.O. Kurakevych, V.L. Solozhenko, High-pressure design of advanced bn-based materials, Molecules. 21 (2016) 1399. https://doi.org/10.3390/molecules21101399.

[45]   S. Gao, B. Li, D. Li, C. Zhang, R. Liu, S. Wang, Micromorphology and structure of pyrolytic boron nitride synthesized by chemical vapor deposition from borazine, Ceram. Int. 44 (2018) 11424–11430. https://doi.org/10.1016/j.ceramint.2018.03.201.

[46]   D.J. Kester, K.S. Ailey, R.F. Davis, Deposition and characterization of boron nitride thin films, Diam. Relat. Mater. 3 (1994) 332–336. https://doi.org/10.1016/0925-9635(94)90181-3.

[47]   C. Cazorla, T. Gould, Polymorphism of bulk boron nitride, Sci. Adv. 5 (2019). https://doi.org/10.1126/sciadv.aau5832.

[48]   S.M. Gilbert, T. Pham, M. Dogan, S. Oh, B. Shevitski, G. Schumm, S. Liu, P. Ercius, S. Aloni, M.L. Cohen, A. Zettl, Alternative stacking sequences in hexagonal boron nitride, 2D Mater. 6 (2019). https://doi.org/10.1088/2053-1583/ab0e24.

[49]   Y. Tian, C. Kou, M. Lu, Y. Yan, D. Zhang, W. Li, X. Cui, S. Zhang, M. Zhang, L. Gao, Superhard monoclinic BN allotrope in M-carbon structure, Phys. Lett. Sect. A Gen. At. Solid State Phys. 384 (2020) 126518. https://doi.org/10.1016/j.physleta.2020.126518.

[50]   K. Doll, J.C. Schön, M. Jansen, Structure prediction based on ab initio simulated annealing for boron nitride, Phys. Rev. B - Condens. Matter Mater. Phys. 78 (2008). https://doi.org/10.1103/PhysRevB.78.144110.

[51]   D. M. P. Mingos, High Performance Non-Oxide Ceramics II, 2002.

[52]   V.L. Solozhenko, D. Andrault, G. Fiquet, M. Mezouar, D.C. Rubie, Synthesis of superhard cubic BC2N, Appl. Phys. Lett. 78 (2001) 1385–1387. https://doi.org/10.1063/1.1337623.

[53]   R.H. Wentorf, Cubic form of boron nitride, J. Chem. Phys. 26 (1957) 956. https://doi.org/10.1063/1.1745964.

[54]   J.H. Edgar, Properties of group III nitrides, INSPEC, Institution of Electrical Engineers, 1994. https://books.google.com/books/about/Properties_of_Group_III_Nitrides.html?hl=pt-PT&id=3bZRAAAAMAAJ (accessed June 1, 2022).

[55]   P. Rogl, Materials science of ternary metal boron nitrides, in: Int. J. Inorg. Mater., Elsevier, 2001: pp. 201–209. https://doi.org/10.1016/S1466-6049(01)00009-5.

[56]   G. Will, G. Nover, J. Von Der Gönna, New experimental results on the phase diagram of boron nitride, J. Solid State Chem. 154 (2000) 280–285. https://doi.org/10.1006/jssc.2000.8850.

[57]   M. Hofmann, H.F.S. Iii, Computational Chemistry, (n.d.).

[58]   L.C. Nistor, G. Van Tendeloo, G. Dinca, Crystallographic aspects related to the high pressure - High temperature phase transformation of boron nitride, Philos. Mag. 85 (2005) 1145–1158. https://doi.org/10.1080/14786430412331325058.

[59]   T. Sekine, T. Kobayashi, H. Nameki, Effects of deviatoric stress and radial strain on the shock-induced diffusionless transformation in boron nitride, J. Appl. Phys.

81 (1997) 527–529. https://doi.org/10.1063/1.364132.

[60] L. Hromadová, R. Martoňák, Pressure-induced structural transitions in BN from ab initio metadynamics, Phys. Rev. B - Condens. Matter Mater. Phys. 84 (2011) 1–7. https://doi.org/10.1103/PhysRevB.84.224108.

[61] J. Von Der Gijnna, H.J. Meurer, G. Nover, T. Peun, D. Schiinbohm, G. Will, In-situ investigations of the reversible in the Li , N-BN catalyst system using synchrotron radiation, 33 (1998).

[62] O.O. Kurakevych, V.L. Solozhenko, High-pressure design of advanced bn-based materials, Molecules. 21 (2016). https://doi.org/10.3390/molecules21101399.

[63] V.L. Solozhenko, High Pressure Scinece and Technology, Proceedings of the Joint XV AIRAPT & XXXIII EHPRG International Conference, in: High Press. Scinece Technol. Proc. Jt. XV AIRAPT XXXIII EHPRG Int. Conf., World Scientific, Singapore, 1996: p. 338.

[64] R.H. Wentorf, Condensed systems at high pressures and temperatures, J. Phys. Chem. 63 (1959) 1934–1940. https://doi.org/10.1021/j150581a033.

[65] V.L. Solozhenko, Determination of the melting parameters of boron nitride, Teplofiz. Vysok. Temp. 29 (1991) 1112–1120.

[66] A. Zerr, G. Serghiou, R. Boehler, No Title, in: Procedings 5rd NIRIM Int. Symp. Adv. Mater., NIRIM, Tsukuba, 1998: p. 5.

[67] H. Sachdev, R. Haubner, H. Nöth, B. Lux, Investigation of the c-BN/h-BN phase transformation at normal pressure, Diam. Relat. Mater. 6 (1997) 286–292. https://doi.org/10.1016/s0925-9635(96)00697-8.

[68] J.T. Cahill, W.L. Du Frane, C.K. Sio, G.C.S. King, J.C. Soderlind, R. Lu, M.A. Worsley, J.D. Kuntz, Transformation of boron nitride from cubic to hexagonal under 1-atm helium, Diam. Relat. Mater. 109 (2020). https://doi.org/10.1016/j.diamond.2020.108078.

[69] V.Z. Turkevich, Phase diagrams and synthesis of cubic boron nitride, J. Phys. Condens. Matter. 14 (2002) 10963–10968. https://doi.org/10.1088/0953-8984/14/44/410.

[70] J. Zhang, R. Tu, T. Goto, Cubic boron nitride- containing ceramic matrix composites for cutting tools, in: I.M. Low (Ed.), Adv. Ceram. Matrix Compos., Woodhead Publishing Limited, 2014: pp. 570–586. https://www.sciencedirect.com/book/9780857091208/advances-in-ceramic-matrix-composites (accessed August 26, 2021).

[71] V. Bushlya, O. Gutnichenko, J. Zhou, P. Avdovic, J.E. Ståhl, Effects of cutting speed when turning age hardened inconel 718 with PCBN tools of binderless and low-CBN grades, Mach. Sci. Technol. 17 (2013) 497–523. https://doi.org/10.1080/10910344.2013.806105.

[72] W. Deng, F. Deng, C. Hao, X. Yang, R. Liu, X. Ma, X. He, H. Wang, Self-bonding mechanism of pure polycrystalline cubic boron nitride under high pressure and temperature, Int. J. Refract. Met. Hard Mater. 86 (2020) 105061. https://doi.org/10.1016/j.ijrmhm.2019.105061.

[73] N. Tan, C.J. Liu, Y.J. Li, Y.W. Dou, H.K. Wang, H. Ma, Z.L. Kou, D.W. He, Characterization of polycrystalline cBN compacts sintered without any additives, EPJ Appl. Phys. 53 (2011). https://doi.org/10.1051/epjap/2010100321.

[74] B.K. Agarwala, B.P. Singh, S.K. Singhal, Synthesis and characterization of polycrystalline sintered compacts of cubic boron nitride, J. Mater. Sci. 21 (1986) 1765–1768.

[75] W.M. Haynes, CRC Handbook of Chemistry and Physics, 97th ed., 2017.

[76] Characteristics Titanium, KOBE STEEL, LTD., (n.d.). https://www.kobelco.co.jp/english/titan/characteristic/index.html (accessed June 1, 2022).

[77] L. Li, Y. Zhao, K. Sun, H. Ji, D. Feng, Z. Li, Composition, microstructure and mechanical properties of cBN-based composites sintered with AlN- Al- Ni binder, Ceram. Int. 44 (2018) 16915–16922. https://doi.org/10.1016/j.ceramint.2018.06.130.

[78] M.P. Bezhenar, S.M. Konoval, S.A. Bozhko, M.G. Loshak, L.I. Aleksandrova, M.I. Zaika, P.A. Nagornyi, H.M. Bilyavina, Physico-mechanical properties of cBN composites produced by a high-pressure reaction sintering of cubic boron nitride and aluminum powders, J. Superhard Mater. 32 (2010) 1–13. https://doi.org/10.3103/S1063457610010016.

[79] J. Angseryd, M. Elfwing, E. Olsson, H.O. Andrén, Detailed microstructure of a cBN based cutting tool material, Int. J. Refract. Met. Hard Mater. 27 (2009) 249–255. https://doi.org/10.1016/j.ijrmhm.2008.09.008.

[80] A. McKie, J. Winzer, I. Sigalas, M. Herrmann, L. Weiler, J. Rödel, N. Can, Mechanical properties of cBN-Al composite materials, Ceram. Int. 37 (2011) 1–8. https://doi.org/10.1016/j.ceramint.2010.07.034.

[81] K. V. Slipchenko, D.A. Stratiichuk, V.Z. Turkevich, N.M. Bilyavyna, V.M. Bushlya, J.E. Ståhl, Sintering of BN Based Composites with ZrC and Al under High Temperatures and Pressures, J. Superhard Mater. 42 (2020) 229–234. https://doi.org/10.3103/S1063457620040103.

[82] D. V. Turkevych, V. Bushlya, J.E. Ståhl, I.A. Petrusha, N.N. Belyavina, V.Z. Turkevich, HP-HT sintering, microstructure, and properties of B6O- and TiC-containing composites based on cBN, J. Superhard Mater. 37 (2015) 143–154. https://doi.org/10.3103/S1063457615030016.

[83] M. Kitiwan, A. Ito, J. Zhang, T. Goto, Densification and mechanical properties of cBN-TiN-TiB2 composites prepared by spark plasma sintering of SiO2-coated cBN powder, J. Eur. Ceram. Soc. 34 (2014) 3619–3626. https://doi.org/10.1016/j.jeurceramsoc.2014.05.018.

[84] M.A. Umer, P.H. Sub, D.J. Lee, H.J. Ryu, S.H. Hong, Polycrystalline cubic boron nitride sintered compacts prepared from nanocrystalline TiN coated cBN powder, Mater. Sci. Eng. A. 552 (2012) 151–156. https://doi.org/10.1016/j.msea.2012.05.024.

[85] O. Fukunaga, The equilibrium phase boundary between hexagonal and cubic boron nitride, Diam. Relat. Mater. 9 (2000) 7–12. https://doi.org/10.1016/S0925-9635(99)00188-0.

[86] H. Sumiya, K. Harano, Y. Ishida, Mechanical properties of nano-polycrystalline cBN synthesized by direct conversion sintering under HPHT, Diam. Relat. Mater. 41 (2014) 14–19. https://doi.org/10.1016/j.diamond.2013.10.014.

[87] Y. Liu, A. Sun, S. Zhong, P. Mo, Y. Wu, Effect of Al[sbnd]Ti content on mechanical properties of in-situ synthesized PcBN composites, Diam. Relat. Mater. 109 (2020) 108068. https://doi.org/10.1016/j.diamond.2020.108068.

[88] Z. Jiang, Q. Jian, Y. Han, Y. Zhu, Z. Li, Performance evaluation of cBN-Ti3AlC2–Al composites fabricated by HTHP method, Ceram. Int. 46 (2020) 24449–24453. https://doi.org/10.1016/j.ceramint.2020.06.228.

[89] H. Ji, Z. Li, K. Sun, Y. Zhu, Assessment of the performance of TiB2 nanoparticles doped cBN-TiN-Al-Co composites by high temperature high pressure sintering, Mater. Chem. Phys. 233 (2019) 46–51. https://doi.org/10.1016/j.matchemphys.2019.05.042.

[90] J. Zhang, R. Tu, T. Goto, Preparation of Ni-cBN composites by spark plasma sintering, J. Japan Soc. Powder Powder Metall. 59 (2012) 410–271. https://doi.org/10.2497/jjspm.59.410.

[91] M. Hotta, T. Goto, Spark plasma sintering of TiN-cubic BN composites, J. Ceram. Soc. Japan. 118 (2010) 137–140. https://doi.org/10.2109/jcersj2.118.137.

[92] J. Zhang, R. Tu, T. Goto, Spark plasma sintering of Al2O3–cBN composites facilitated by Ni nanoparticle precipitation on cBN powder by rotary chemical vapor deposition, J. Eur. Ceram. Soc. 31 (2011) 2083–2087. https://doi.org/10.1016/j.jeurceramsoc.2011.05.019.

[93] J. Zhang, R. Tu, T. Goto, Densification of SiO 2-cBN composites by using Ni nanoparticle and SiO 2 nanolayer coated cBN powder, Ceram. Int. 38 (2012) 4961–4966. https://doi.org/10.1016/j.ceramint.2012.02.090.

[94] B. Wang, Y. Qin, F. Jin, J.F. Yang, K. Ishizaki, Pulse electric current sintering of cubic boron nitride/tungsten carbide-cobalt (cBN/WC-Co) composites: Effect of cBN particle size and volume fraction on their microstructure and properties, Mater. Sci. Eng. A. 607 (2014) 490–497. https://doi.org/10.1016/j.msea.2014.04.029.

[95] J.O. Andersson, T. Helander, L. Höglund, P. Shi, B. Sundman, Thermo-Calc & DICTRA, computational tools for materials science, Calphad Comput. Coupling Phase Diagrams Thermochem. 26 (2002) 273–312. https://doi.org/10.1016/S0364-5916(02)00037-8.

[96] M. Dios, Synthesis, processing and mechanical characterization of Ti(C,N)-based cermets through the combination of colloidal and powder metallurgy techniques, 2017.

[97] E.M. Garcia-Ayala, L. Silvestroni, J. Yus, B. Ferrari, J.Y. Pastor, A.J. Sanchez-Herencia, Colloidal processing and sintering of WC-based ceramics with low Ni content as sintering aid, J. Eur. Ceram. Soc. 41 (2021) 1848–1858. https://doi.org/10.1016/j.jeurceramsoc.2020.10.038.

[98] B. Beverskog, I. Puigdomenech, Revised Pourbaix diagrams for nickel at 25-300°c, Corros. Sci. 39 (1997) 969–980. https://doi.org/10.1016/S0010-938X(97)00002-4.

[99] M. Hosokawa, K. Nogi, M. Naito, T. Yokoyama, Nanoparticle Technology Handbook, 2012. https://doi.org/10.1016/C2010-0-69564-2.

[100] D. Myers, Surfaces, interfaces, and colloids, 1999.

[101] R. Moreno, Colloidal processing of ceramics and composites, Adv. Appl. Ceram. 111 (2012) 246–253. https://doi.org/10.1179/1743676111Y.0000000075.

[102] E. Piacenza, A. Presentato, R.J. Turner, Stability of biogenic metal(loid) nanomaterials related to the colloidal stabilization theory of chemical nanostructures, Crit. Rev. Biotechnol. 38 (2018) 1137–1156.

https://doi.org/10.1080/07388551.2018.1440525.

[103] Water Based Colloidal Processing of Ceramic Laminates A. J. Sánchez-Herencia, 333 (2007) 39–48.

[104] NSM Archive - Boron Nitride (BN) - Optical properties, (n.d.). http://www.ioffe.ru/SVA/NSM/Semicond/BN/optic.html (accessed June 1, 2022).

[105] Spark plasma sintering [SubsTech], (n.d.). http://www.substech.com/dokuwiki/doku.php?id=spark_plasma_sintering&do=recent&DokuWiki=e579a03e5 (accessed June 1, 2022).

[106] C. Gorynski, U. Anselmi-Tamburini, M. Winterer, Controlling current flow in sintering: A facile method coupling flash with spark plasma sintering, Rev. Sci. Instrum. 91 (2020). https://doi.org/10.1063/1.5119059.

[107] S. Gates-Rector, T. Blanton, The Powder Diffraction File: a quality materials characterization database, Powder Diffr. 34 (2019) 352–360. https://doi.org/10.1017/S0885715619000812.

[108] T. Degen, M. Sadki, E. Bron, U. König, G. Nénert, The high score suite, in: Powder Diffr., Cambridge University Press, 2014: pp. S13–S18. https://doi.org/10.1017/S0885715614000840.

[109] R. Young, The Rietveld Metod, Clim. Chang. 2013 - Phys. Sci. Basis. (1993) 293. http://scholar.google.com/scholar?hl=en&btnG=Search&q=intitle:The+Rietveld+Method#1 (accessed June 1, 2022).

[110] ASTM C20-00, Standard Test Methods for Apparent Porosity , Water Absorption , Apparent Specific Gravity , and Bulk Density of Burned Refractory Brick and Shapes by Boiling Water, Am. Soc. Test. Mater. 00 (2015) 1–3. https://doi.org/10.1520/C0020-00R10.2.

[111] E. Benko, J.S. Stanislaw, B. Królicka, A. Wyczesany, T.L. Barr, CBN-TiN, cBN-TiC composites: Chemical equilibria, microstructure and hardness mechanical investigations, Diam. Relat. Mater. 8 (1999) 1838–1846. https://doi.org/10.1016/S0925-9635(99)00131-4.

[112] E. Benko, P. Klimczyk, J. Morgiel, A. Włochowicz, T.L. Barr, Electron microscopy investigations of the cBN-Ti compound composites, in: Mater. Chem. Phys., Elsevier, 2003: pp. 336–340. https://doi.org/10.1016/S0254-0584(03)00016-6.

[113] E. Piskorska, E. Benko, I.N. Demchenko, A. Benko, E. Welter, T.L. Barr, X-ray absorption studies of the c-BN -Ti based composites, (n.d.) 6–7.

[114] J.T. Cahill, W.L. Du Frane, C.K. Sio, G.C.S. King, J.C. Soderlind, R. Lu, M.A. Worsley, J.D. Kuntz, Transformation of boron nitride from cubic to hexagonal under 1-atm helium, Diam. Relat. Mater. 109 (2020) 108078. https://doi.org/10.1016/j.diamond.2020.108078.

[115] B. Hering, A.K. Wolfrum, T. Gestrich, M. Herrmann, Thermal stability of TiN coated cubic boron nitride powder, Materials (Basel). 14 (2021). https://doi.org/10.3390/ma14071642.

[116] L. Yu, B. Gao, Z. Chen, C. Sun, D. Cui, C. Wang, Q. Wang, M. Jiang, In situ FTIR investigation on phase transformations in BN nanoparticles, Chinese Sci. Bull. 50 (2005) 2827–2831. https://doi.org/10.1360/982005-570.

Attachments

Thermal reactivity of cBN-TiCN-Ni based composite sintered by SPS

Ricardo Mineiro[a]; C.M. Fernandes[b;] D. Figueiredo[b]; B. Ferrari[c]; E.L. Silva[a]; A.J. Sanchez-Herencia[c]; A.M.R. Senos[a]

[a]Dep. Materials and Ceramic Engineering/ CICECO, University of Aveiro, 3810-193 Aveiro, Portugal; mineiro@ua.pt; elsilva@ua.pt; anamor@ua.pt

[b]Palbit, Rua das Tílias, 3854-908 Palhal, Branca, Albergaria-a-Velha, Portugal; cfernandes@palbit.pt; dfigueiredo@palbit.pt

[c]Instituto de Cerámica y Vidrio, CSIV, C/ Kelsa 5, 28049, Madrid, Spain; ajsanchez@icv.csic.es; bferrari@icv.csic.es

Abstract

PcBN materials are normally sintered by HPHT techniques resulting in an expensive material. These techniques are used with the purpose of achieving a full densified material while preventing the formation of hexagonal BN with would decrease the hardness of the PcBN. In this regard, the fast-sintering rates of the Spark Plasma Sintering technique may help decrease the extension of the phase transformation in the material and thus minimize the hardness decrease. In this work it was used the Spark Plasma Sintering technique to sinter a cBN-TiCN based composite and studied its sintering behavior, densification, and phase transformation with and without the addition of metallic Ni. A greater densification of the material was achieved with introduction of Ni, but full removal of open porosity was only possible at 1700 ºC, temperature at which theBN phase transformation to hexagonal form completely occurred. On this regard, the Ni phase did not change the phase transformation to lower or higher temperatures but accelerated the phase transformation. Additionally, thermodynamic calculations were used to predict the stable crystallographic phases of the system, and experimentally confirmed by X-ray Diffraction technique.

1.Introduction

Boron nitride (BN) was firstly discovered in nature in 2009 in its cubic form as a few nanometers incrustations in minerals extracted from the earth's crust, but it has been artificially produced for industrial use since the 1950´s [1,2]. BN is a ceramic material known for its thermal and chemical stability, high thermal conductivity, and low electrical conductivity (isolator) [3,4]. There are various known crystallographic structures for BN, but the cubic and hexagonal forms are the only ones that are thermodynamic stable [5,6]. Cubic boron nitride (cBN) is a very hard and wear resistance material, being the second hardest material with industrial application; its hardness is only lower than diamond, nevertheless presents higher resistance to oxidation and decomposition into other phases than diamond [3,7–9].

Some of the major applications of BN are found in cBN based composites, known as polycrystalline cubic boron nitride (PcBN), as tools for machining and polishing of hard materials, like hardened steels and cast irons, where diamond cannot be used because of its reactivity with Fe and other metallic elements (e.g. Co, Mg, Ni, Cr and Ti) inducing the tendency to form carbides [8,10]. PcBN is usually produced by high temperature high pressure (HTHP) techniques using ceramic (e.g TiCN, TiC, TiN) and/or metallic binders (e.g Ti, Al, Ni, Co) [10–12]. The metallic binders tend to react with the boron nitride and form borides and nitrides, which result in a chemical bond between the constituents of the material that is stronger than a pure mechanical one and lead to a better performance and lifetime of the material [13,14]. Additionally, the use of a metallic binder gives other properties to the material, such as electrical conductivity, and allows its metal-joining processing such as brazing the PcBN tips in a WC-Co substrate [15,16].

Due to the high covalent atomic bond of BN, high sintering temperatures (1200-1500 ºC) are required, together with high pressure (4–6 GPa) to achieve the full material densification maintaining the cubic phase in the stability zone [5,10,17]. At normal pressure the transition phase structure from cubic to hexagonal is calculated to occur at 1320 $\pm$ 380 ºC, while experimentally it varies between 900 and 2200 ºC [5,18–20]. This uncertainty is caused by experimental errors and various factors that influence the temperature at which the transformation occurs, as the materials processing (time, temperature, pressure), and the material intrinsic (number of defects, grain size) or extrinsic characteristics (binders – accelerators or retardants – catalysts and impurities like H_2O, B_2O_3 and O_2 [3,21–25]. The presence of hexagonal phase is not desirable, due to its lower Vickers hardness (0,131 GPa when) comparatively with the cubic phase (around 40 – 50 GPa for micrometric grain size), which led to a drastic decrease in hardness of the PcBN [4,26].

The sintering by HPHT techniques allows the application of extremely high pressures and temperatures, as indicated above, but restricts the amount of material sintered and its shape to simple geometries; additionally, the complex and time-consuming process of the shaping parts assembly before sintering and intense conditions used makes it a high-cost material processing [27–29].

Spark Plasma Sintering (SPS), an Electric Field Assisted Sintering (EFAS) technique, uses an intense electric field to heat the system that can reach heating rates as high as 1000 °C/min up to a maximum of 2400 °C and 100-150 MPa of applied pressure [30]. This can decrease the heating time to a minimum and potentially decrease the extension of phenomenon, such as cubic–hexagonal phase transformation of BN [31]. This rapid heating rate, combined with shorter sintering times, result in a larger production rate compared with other sintering techniques, although there are still limitations, like geometry constraints and high-cost equipment [31]. Using the SPS technique, Mettaya et al. [32] studied the effect of SiO_2 coating of cBN particles in the cBN-TiN-TiB$_2$ system, and observed that with an increase of cBN from 0 to 80% vol. the relative density dropped from 96 to 80%, while the hardness remained in the 15 – 25 GPa range; Yuan et al. [28] studied the sinterability of the cBN-Ti-Al system with cBN varying between 40 and 60% vol, and concluded that the 45% cBN + 35% Ti + 20% Al vol. composition sintered at 1400 ºC, achieved the best relative density and hardness, 99% and 14 GPa respectively, maintaining a heating rate of 100 ºC/min and a dwell time of 10 min with 50 MPa of uniaxial pressure; Jianfeng et al. [33] studied the sinterability of the Ni-cBN system varying the cBN amount up to 50% vol and dwell temperature between 900 – 1200 ºC, and observing a decrease of relative density from 99 to 89% when increasing the amount of cBN, while the hardness reached a maximum of 3,5 GPa for the 70% Ni + 30% cBN vol. composition sintered at 1100 ºC.

The major difficulty in sintering PcBN composites is to achieve full densification with low amounts of binder and using less extreme sintering conditions as possible, since less binder results in a higher hardness closer to cBN, but will require an increase of the sintering conditions to more extreme values, while higher temperatures promote the phase transformation of BN from cubic to hexagonal, which drastically reduces the hardness of the material [2,29,34].

The feasibility of SPS as a consolidation technique in high cBN based composites (>70%vol.) will be investigated. For such purpose coarse cBN particles coated with Ti were proportionated with TiCN. In order to increase the sinterability of cBN+TiCN composition the addition of Ni binder was also performed. The thermal reactivity behavior during SPS sintering, in particular the cBN to hBN phase transformation was also investigated.

2.Experimental procedure

The following powders were used: cBN (coated with 17wt% of titanium, D_{50}<44 µm, Hyperion), TiCN (D_{50}<1,65 µm, Treibacher), and Ni (D_{50}<2,2 – 2,6 µm, Ampere). The cBN powder particles are significantly coarser than those of the Ti(C,N) and Ni powders, Figure 1 and Figure 2,

as described in SEM images (Hitachi SU-70 and Hitachi SU-41 respectively). The particles of cBN have an angular shape and are uniformly coated with Ti (Figure 1-b) (energy dispersive spectroscopy, EDS, Bruker Quantax 400). The Ti(C,N) and Ni particles are rounder and agglomerated, as oppose to the cBN ones that are looser (Figure 2). The grain size distribution of the cBNis very uniform, with an average grain size (D_{50}) of 57 µm (laser diffraction analysis, Coulter), Figure 3-a, and are in fact coated with a titanium nitride phase (Ti_2N), Figure 3-b, while no metallic Ti was detected, while BN phase is in the cubic structure cBN,as confirmed by XRD (Figure 3-b) (Panalytical Almelo Netherlands, X´Pert PRO[3] with copper ampoule).
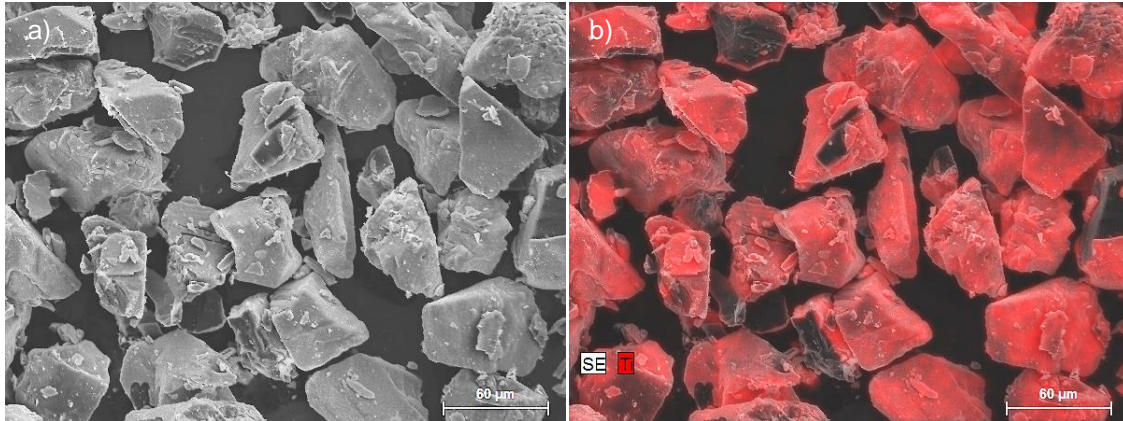

Figure 1- Morphology of the cBN particles by (a) SEM and a (b) EDS of the titanium coating.
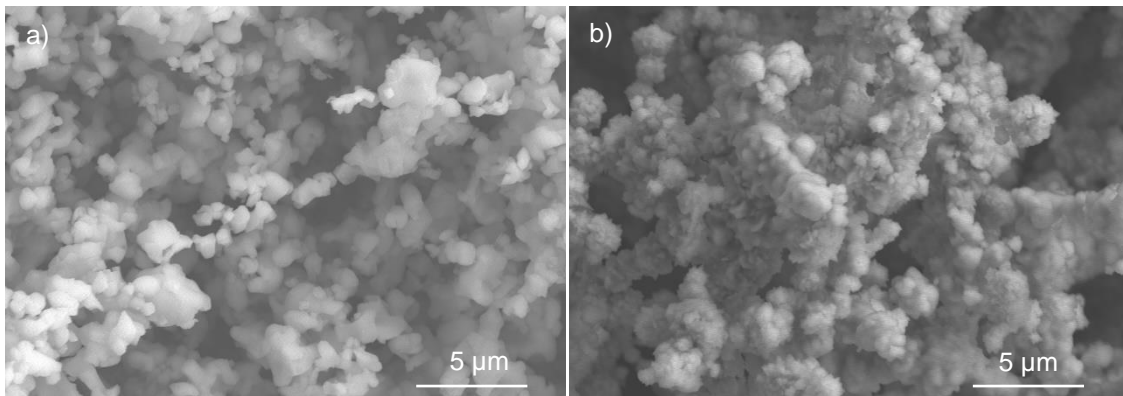

Figure 2- Morphologies of the (a) TiCN and (b) Ni particles.

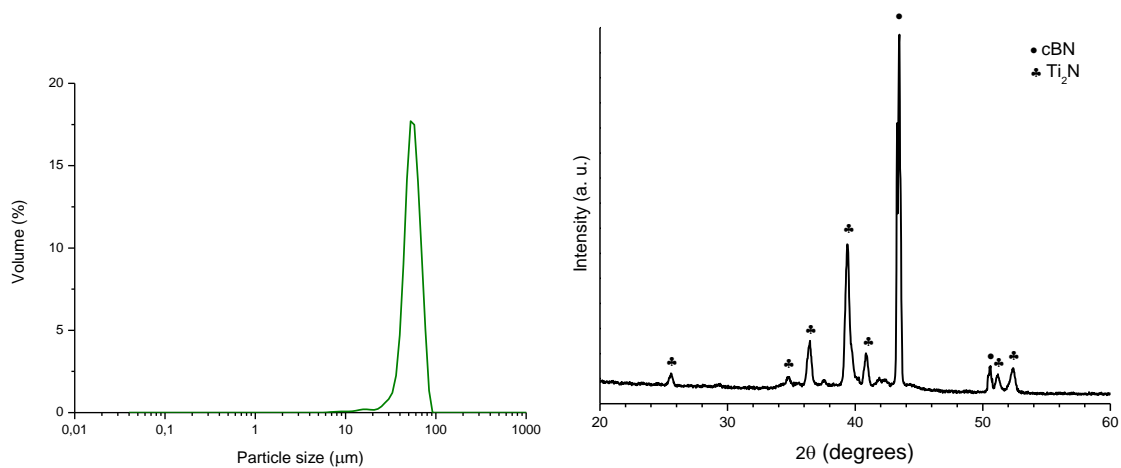a)   b)

Figure 3- (a) Particle size distribution and (b) XRD pattern of the cBN powder.

Thermodynamic calculations for the cBN-Ti(C,N) composition phase diagrams with and without Ni were performed in Thermocalc software using the TCFE11 database. The calculated phase diagrams were used to select the cBN based compositions in terms of their final phases after sintering. These compositions are presented in Table 1.

The powders were mixed in the proportions indicated in Table 1, by mechanical mixture for 90 min, using a 3D powder blender mixer. Two different compositions were prepared, one without Ni and the other with 5 vol.% of Ni (Table 1). The proportionated components for each composition are presented in volume and weight percentages.

Table 1- PcBN compositions with and without Ni.

	Vol. %				Wt. %			
	cBN	Ti$_2$N	Ti(C,N)	Ni	cBN	Ti$_2$N	Ti(C,N)	Ni
Composition 1	73	10	17	-	65	13	22	-
Composition 2	69	10	16	5	58	12	20	10

The two compositions were sintered by SPS, Dr. Sinter SPS-510CE, Fuji Electronic Industrial Co., using graphite punches with 10 mm in diameter. The investigated SPS conditions were applied according to Table 2, and the cooling was done at a rate of 100 ºC/min down to 500 ºC, at point where the equipment was turn off and let the samples cooling naturally inside the chamber. During the sintering process, the punches displacement, vacuum, pressure, and temperature were recorded every second. Taking the recorded punches displacement and temperature in situ, dilatometric curves were represented.

Table 2- SPS conditions applied to each composition.

	Sample	Heating rate (ºC/min)	Pressure (MPa)	temperature (ºC)	dwell time (min)
Composition 1	2000			2000	
Composition 2	1400	100	60	1400	10
	1500			1500	
	1600			1600	
	1700			1700	
	2000			2000	

The microstructure of the sintered samples was analyzed using a Scanning Electron Microscopy (SEM) Hitachi model SU-70 with EDS microanalysis system Bruker Quantax 400 model,

and a Phenom Pro (G5) with a Silicon Drift Detector (SSD) Phenom. As for the structure, it was analyzed by X-Ray Diffraction (XRD) Panalytical (Almelo, Netherlands) model X´Pert PRO[3], and a Bruker D8 Advance, both with Cu ampoule of $\lambda_{Cu\,K\alpha1}$ = 1,54056 Å. The diffractograms used to perform the Rietveld analysis were acquired in a Panalytical (Almelo, Netherlands), model X´Pert PRO[3] and a Panalytical Empyrean diffractometer. Raman Spectroscopy was also performed using a Renishaw InVia Raman Spectroscope with a laser of 514 µm wavelength.

For the Rietveld analysis it was considered the phases given in Table 3, along with theoretical densities given in the ICCD PDF files for each phase.

Table 3- Theoretical densities, retrieved from the respective ICDD PDF file, for each considered phase used in Rietveld analysis.

Phase	Theoretical density (g/cm^3)	ICDD PDF file
cBN	3,5	04-008-4847
hBN	2,3	04-013-1175
TiCN	3,5	04-011-9013
TiB$_2$	4,5	04-010-8470
Ni$_3$B	8,2	04-003-1948

The apparent density and open porosity were determined by the Archimedes' method, following the standard ASTM C20-00 [35].

3. Results and discussion

3.1 Thermodynamic calculations of the cBN-Ti(C,N) phase diagrams with addition of Ni

The system of both compositions was defined using the constituents BN, Ti, C, N and Ni (If present) in mass amount, with a pressure of 60 MPa. Due to the limitation in the TCFE11 database, where only the hexagonal phase was included, the calculations were done considering a stable hBN in all the temperature range.

The phases diagrams obtained from the thermodynamic calculations of the BN-Ti(C,N) and BN-Ti(C,N)-Ni systems are shown in Figure 4 and Figure 5 respectively. It was used a temperature scale of 800 to 2100 ºC, although it is generally accepted that equilibrium conditions are only attained for temperatures higher than 1000ºC. Based on the phase diagrams in Figure 4 and 5, the respective compositions 1 and 2, Table 1, were chosen to be inside regions where no graphite is formed at ~1000ºC (represented as red lines).

According to Figure 4 and Figure 5, and considering the initial phases of the powders used, it is expected that the TiB$_2$ phase will form and become stable in the system, while the Ti$_2$N phase, detected in the XRD diffractogram of the cBN powder, Figure 3-b, will disappear from the system, since is not indicated as stable. The formation of a TiB$_2$ phase for these types of systems was already predicted and experimentally confirmed by existing works [36–38]. With the addition of Ni, it is predicted to form a liquid phase at 967 ºC which will be present up to 1736 ºC, and when cooled will lead to the formation of a stable Ni$_3$B phase. The formation of this phase indicates that metallic Ni will react with BN.
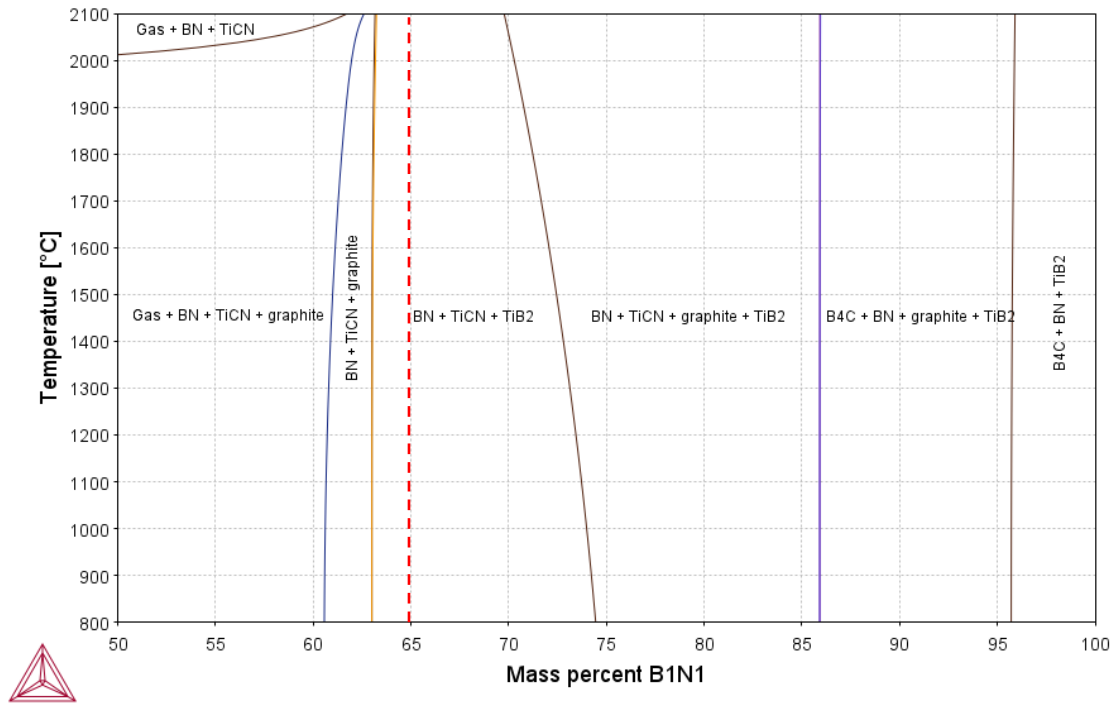
Figure 4- Predicted phases diagram for the BN-Ti(C,N) system. The dashed line corresponds to composition 1.
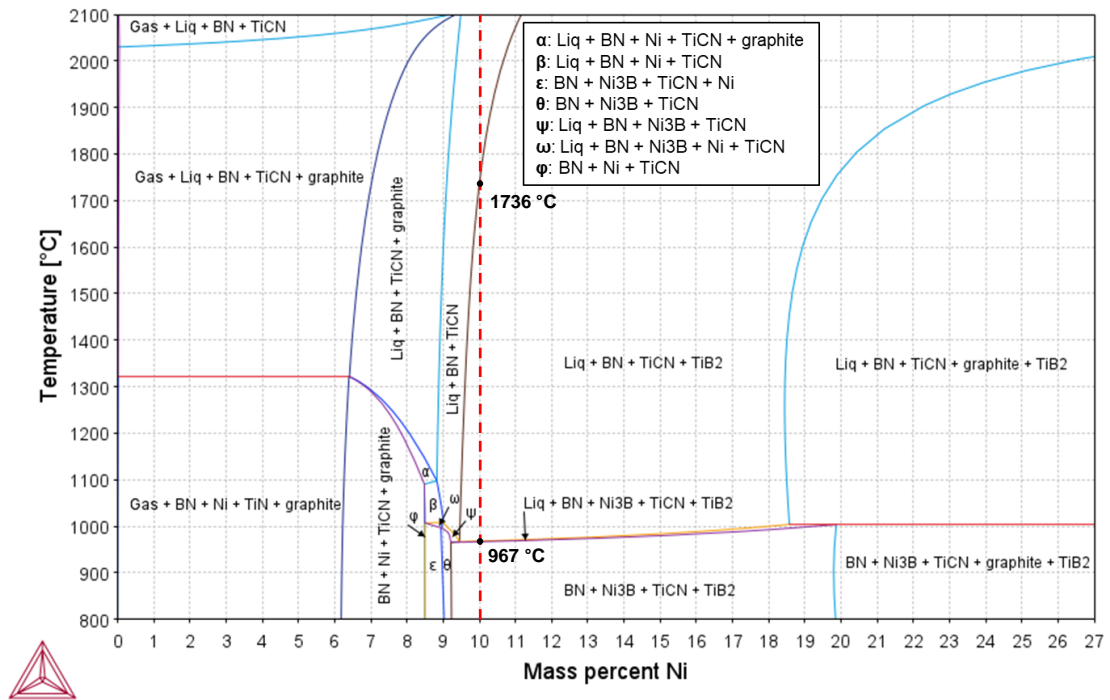

Figure 5- Predicted phases diagram for the BN-Ti(C,N)-Ni system. The dashed line corresponds to composition 2.

3.2. Initial characterization of the compositions

In Figure 6 are showed the morphology of compositions 1 and 2 after mixing. The cBN particles are easily distinguishable from the Ti(C,N) ones in composition 1, due to the much larger size. As for composition 2 it is not possible to distinguish between the Ti(C,N) and Ni particles, as the mean particle size is similar. In both cases, no clear heterogeneities are observed. An XRD analysis of the composition 2 is showed in Figure 7, indicating the presence of the cBN, Ti(C,N), Ni and Ti_2N phases. As shown above, the cBN and Ti_2N phases come from the cBN powder (Figure 3-b).
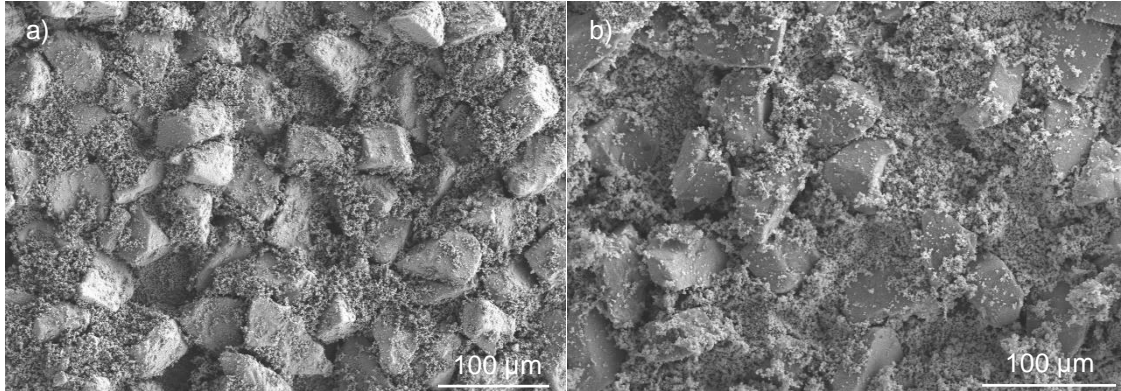

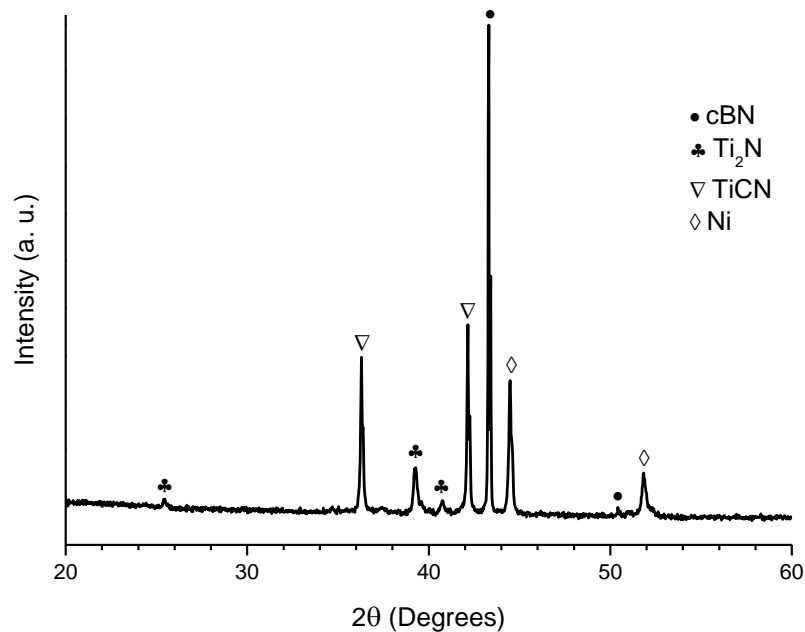Figure 6- Microstructure of the two prepared compositions: a) composition 1 and b) composition 2.

Figure 7- XRD pattern of the composition 2.

3.3 SPS: Effect of nickel addition

The sintering behavior performed with dilatometric analysis during the SPS heating stage is shown in Figure 8 for the two PcBN compositions. In Figure 8-a it is plotted the shrinkage vs temperature for both compositions and in Figure 8-b the respective shrinkage rate curve. Different stages can be observed from the beginning of the densification process, ~600ºC up to 2000ºC. For both compositions, an initial faster shrinkage stage, stage I, is observed, originating a maximum of

the shrinkage rate at ~1020ºC for composition 1 and in the case of composition 2, with Ni, this stage extends up to higher temperature, presenting a higher maximum shrinkage rate at ~1170ºC. Interesting to note that in this stage, the shrinkage rate of composition 2 became larger than that of composition 1 when T approaches 1000ºC, in close agreement with the appearance of the liquid phase at ~967ºC predicted in the phase diagram, Figure 5. In stage II, for T> ~1300ºC, both compositions present equivalent and reduced shrinkage rates up to ~1700 ºC. Above that temperature, a sudden expansion is observed in stage III, resulting in relevant peaks in the shrinkage rate at ~1800ºC and ~1760ºC for composition 1 and composition 2, respectively, which should be associated to the phase transformation cBN-hBN. The starting transformation temperature of ~1700ºC in this work is on the upper limit range of calculated temperatures (1320 $\pm$ 380 ºC) in the literature for the cubic to the hexagonal BN form transformation, but it should also be noted that the SPS conditions are far from equilibrium conditions [18]. The addition of Ni, as reported in the literature, slightly fasten the transformation and resulted in a larger shrinkage, as observed in Figure 8 [22,39]. After the expansion stage III, there is yet a final stage IV where the shrinkage rate is near constant and similar to that of stage II, for both compositions.
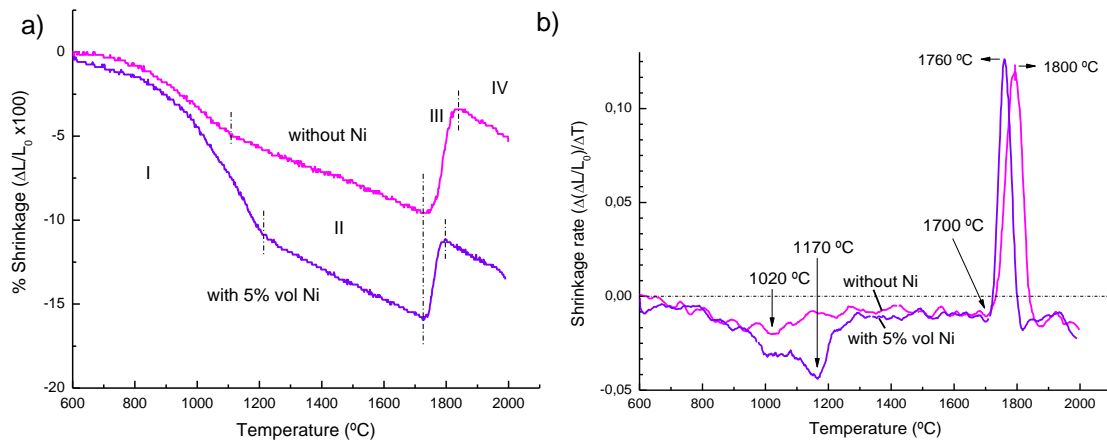

Figure 8- Shrinkage (a) and shrinkage rate (b) of composition 1 (without Ni) and composition 2 (with Ni) in function of the temperature using SPS.

From the XRD analysis of the phases present in both samples sintered at 2000 ºC, Figure 9, four observations can be made: (i) the Ti(C,N) phase seems to remain stable during heating; (ii) only hBN was detected, meaning that all cBN was transformed into hBN and, since there is a volume expansion associated to this transformation, it explains the relevant expansion recorded in the stage III of the dilatometric curves in Figure 8 [32]; (iii) the Ti_2N phase disappeared from the system and TiB_2 phase was formed, meaning that Ti_2N is not stable in the tested conditions while TiB_2 is, although the respective peaks are smaller in the composition containing Ni; (iv) in composition 2, containing Ni, there is the formation of Ni_3B phase, falling in the four phase region $BN+Ni_3B+Ti(C,N)+TiB_2$ of the phase diagram, Figure 5. It can, then, be concluded that the XRD detected phases in both compositions are just those predicted by the respective phase diagrams in Figures 4 and 5, and the final phase compositions just fall in the region of 3 or 4 phases, as expected.
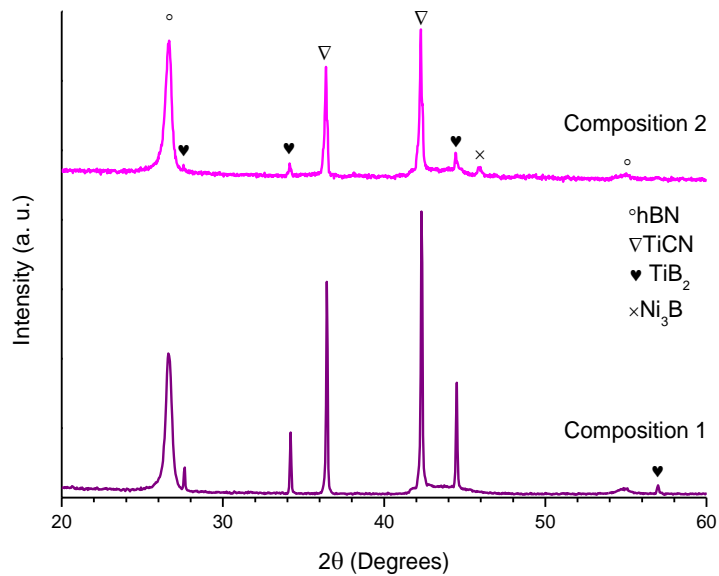
Figure 9- XRD patterns of the sintered composition 1 and composition 2 by SPS.

3.4. SPS: Effect of temperature variation

To study the effect of temperature in the shrinkage of composition 2 before the cBN-hBN transformation, several SPS heat treatments have been performed between 1400 and 1700ºC (Figure 10). With increasing temperature, the shrinkage increases but the shrinkage rate, after the maximum ~1170ºC, is progressively decelerated until it reaches zero at 1700 ºC (Figure 10b). This temperature corresponds to the beginning of the phase transformation as shown in Figure 8.
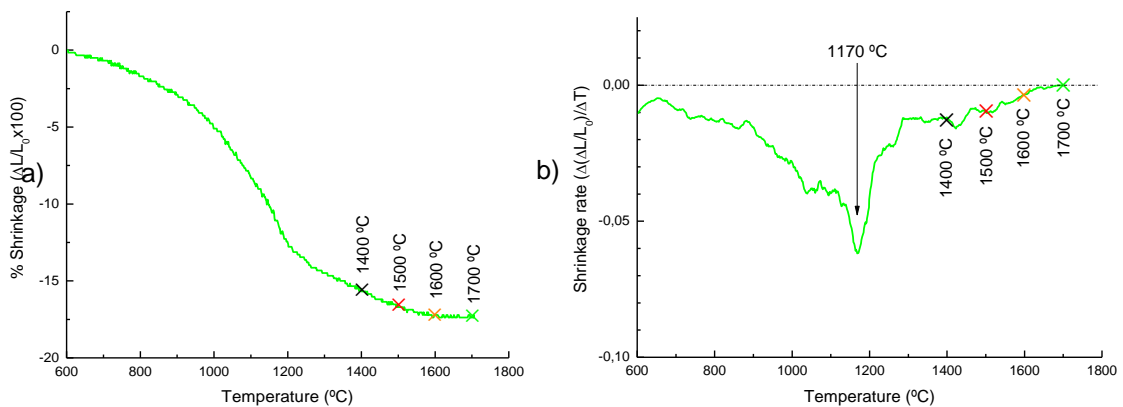

Figure 10- Shrinkage (a) and shrinkage rate (b) in function of temperature of the samples from composition 2, sintered at 1400 – 1700 ºC and 60 MPa.

Figure 11 shows the apparent density and open porosity of the samples in function of the sintering temperature. Apparent density is decreasing slightly with increase in temperature up to 1600 ºC where above that it greatly diminishes. As for open porosity it fluctuates around 16% between 1400- 1600 ºC but reduces to zero at 1700 ºC. Although it was expected a gradual increasing of apparent density and decreasing of open porosity with the increase of temperature this is not the case and the slight decrease of apparent density with a near constant open porosity between 1400-1600ºC may be already attributed to a small extent of cBN to hBN phase transformation, since 10 minutes of holding time were done at those high temperatures. From 1600 up to 1700ºC, the huge reduction of the apparent density with total elimination of the open pores is a consequence of the accelerated phase transformation, since the density of hBN (2,2 g/cm^3) is

79

lower than that of cBN (3,5 g/cm^3), and its volumetric expansion can contribute to the removal of porosity [4,6].
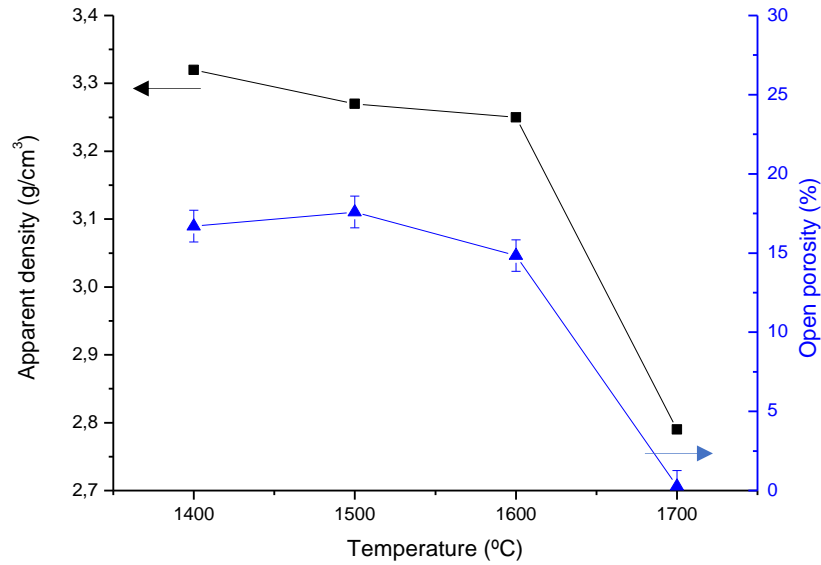

Figure 11- Apparent density and open porosity of samples from composition 2 sintered by SPS at temperatures of 1400 – 1700 ºC.

A comparison of the XRD profiles in composition 2 for the green powder and after SPS at different temperatures, in Figure 12, shows that the detected phases after sintering are the same as the one sintered at 2000 ºC, Figure 9 and predicted by the phase diagram of Figure 5, as summarized in Table 4. In what concerns the phase transformation of BN from cubic to hexagonal, it is observed in Figure 12 that, in fact, a small peak of hBN is already identified in the XRD profile of the sample sintered at 1400 ºC which has a small increase up to 1600 ºC. This means that in this range of temperatures the transformation is slow, as already stated from the data of Figure 11. In the interval from 1600ºC up to 1700 ºC the transformation proceeds at a higher rate and at 1700ºC the cBN phase is no more detected, while is observed to form an amorphous phase between 42º to 47º interval.
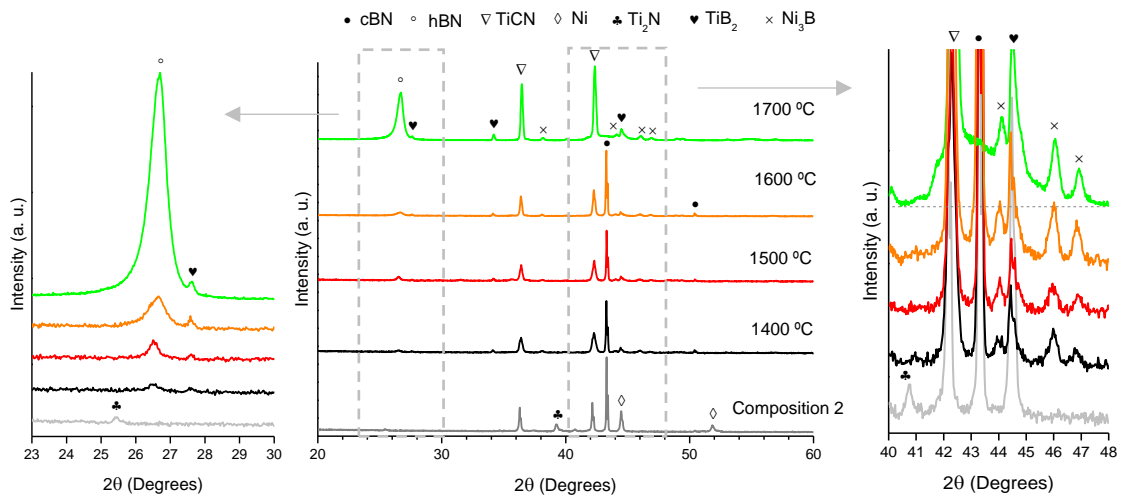

Figure 12- XRD patterns of the composition 2 as-mixed and after SPS at different temperatures.

Table 4- Comparison of predicted and detected phases of composition 2.

Sintering Temperature (ºC)	Predicted phases** (Thermo-Calc)	Detected phases (XRD)	Amount hBN phase (%)***

*	-	cBN+ Ti$_2$N+TiCN+Ni	0
1400		cBN + hBN + TiCN + TiB$_2$ + Ni$_3$B	5
1500		cBN + hBN + TiCN + TiB$_2$ + Ni$_3$B	17
1600	BN + TiCN + TiB$_2$ + Ni$_3$B	hBN + cBN + TiCN + TiB$_2$ + Ni$_3$B	19
1700		hBN + TiCN + TiB$_2$ + Ni$_3$B + amorphous phase	100
2000		hBN + TiCN + TiB$_2$ + Ni$_3$B + amorphous phase	100

*as-prepared composition 2; **Considered at below 1000 ºC; ***Based on the net area of XRD peaks of hBN and cBN respectively.

The phase compositions of the samples sintered at 1500 ºC and 1700 ºC were yet determined using the Rietveld refinement method. The fitting difference plots are shown in Figure 13, with fitting quality parameters in Table 5, and phase compositions given in Table 6. Compared to the nominal phase of composition 2 in Table 1, the BN phase percentage after SPS is higher than expected, i.e., it is 69 vol% before sintering and after sintering, where some boron reacts with Ti and Ni to form the phases TiB2 and Ni3B, respectively, the calculated percentage is ~84 vol%. On the other hand, the phases of TiCN, TiB$_2$ and Ni$_3$B are in a lower percentage than expected. According to the calculated results obtained by Thermocalc software, boron atoms have high solubility on the Ni liquid phase (i. e. 7wt.% at 1700 ºC), with indicate that the BN phase dissolves in the melted Ni phase and dissociate into B and N atoms, with N being lost from the material since no new solid phase containing N atoms is observed. When cooled, there is enough B dissolved to react and form Ni$_3$B phase according to the reaction of Equation 1.

$$2\, BN + 6\, Ni \rightarrow 2\, Ni_3B + N_2 \qquad\qquad \text{Equation 1}$$

Additionally, Ti atoms are also indicated to have high solubility on the Ni liquid phase, (i. e. 12wt.% at 1700 ºC). Considering that the initial Ti$_2$N coating dissociated into Ti and Ni$_2$ phases, since this one is not a stable phase in this system, the Ti would dissolve in the liquid Ni phase and when cooled reacts with the B dissolved forming TiB$_2$ following the reaction of Equation 2.

$$2\, Ti_2N + 8\, BN \rightarrow 4\, TiB_2 + 5\, N_2 \qquad\qquad \text{Equation 2}$$

Besides other reactions that may occur in this system during sintering, in the x-ray Powder Diffraction technique, lighter elements like Boron and Nitrogen tend to emit more signal into the detector than the heavier atoms like Ti and Ni which results in a under quantification of the Rietveldt calculation of phases containing these last elements in relation to phases composed of lighter atoms, as BN. Besides, in some experiments squeezing of a small amount of material out of the mould which is mainly constituted by Ni and some TiCN can occur and some amorphous phase can be formed, as for instances at 1700 ºC in Figure 12. Despite the refereed uncertainty in the values of Table 5, the calculated values point to a ratio of hBN/cBN of only ~10 vol% at 1500ºC, whereas only hBN is detected at 1700ºC.
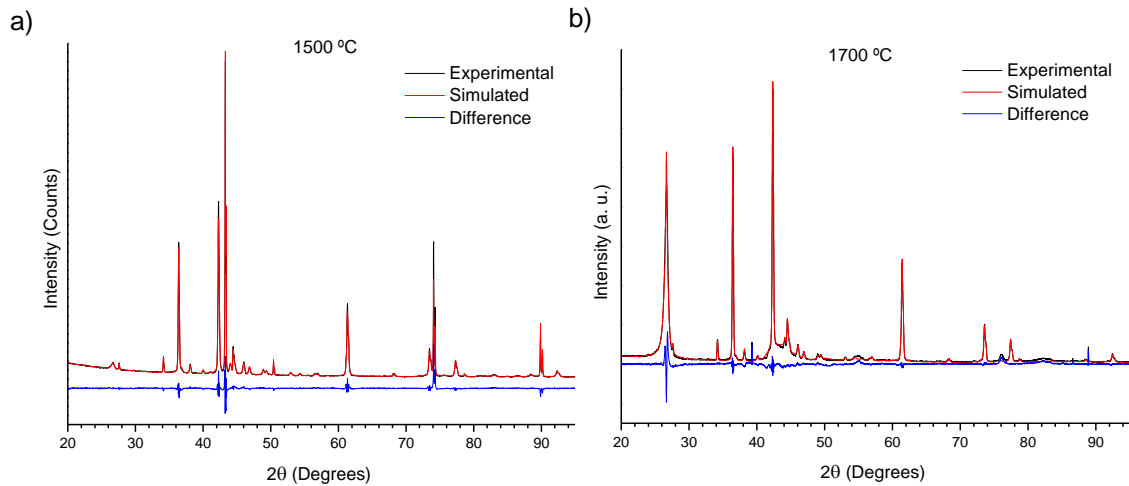
Figure 13- Rietveld refinement results plot for samples of composition 2, sintered at a) 1500 ⁰C and b) 1700 ⁰C.

Table 5- Fitting parameters of the Rietveld method performed on sintered samples of composition 2.

Sintering temperature (⁰C)	Rwp	Rexp	Rp	χ^2
1500	5,07	1,67	2,98	3,03
1700	14,68	2,88	9,49	5,09

Table 6- Phases' composition and physical characteristics of the composition 2 after SPS.

Phases	1500 ⁰C (vol. %)	1700 ⁰C* (vol. %)
cBN	75	-
hBN	8	84
TiCN	14	13
TiB$_2$	2	1
Ni$_3$B	2	2

*Some material (Ni+TiCN) exited the mold during sintering

3.5 Microstructural characterization

In Figure 14-a it is shown the microstructure of the sample sintered at 1600 ⁰C. It is clearly distinguishable the difference between the BN phases, where the cubic one has sharp edges and a planar surface, while the hexagonal one as a rougher appearance, being the grains detached from the matrix. The difference in texture of the two phases has already been observed in other works, where it is indicated that the hBN starts forming from the surface of the cBN grains [21,25,28,40]. The Raman spectroscopy spectra performed in random individual BN grains of samples sintered in the 1400 – 1700 ⁰C interval, are shown in Figure 14-b. The spectra, indicate the presence of only cubic (1056 and 1304 cm^{-1}) and hexagonal (1367 cm^{-1}) phases by detection of each Raman characteristic frequencies, meaning that no metastable BN phase was formed [41]. Although cBN particles could yet be detected by Raman spectroscopy at 1700 ⁰C, Figure 14-b, its amount should be below the detection limit of the XRD technique to be not detected in the diffractogram of Figure 12.
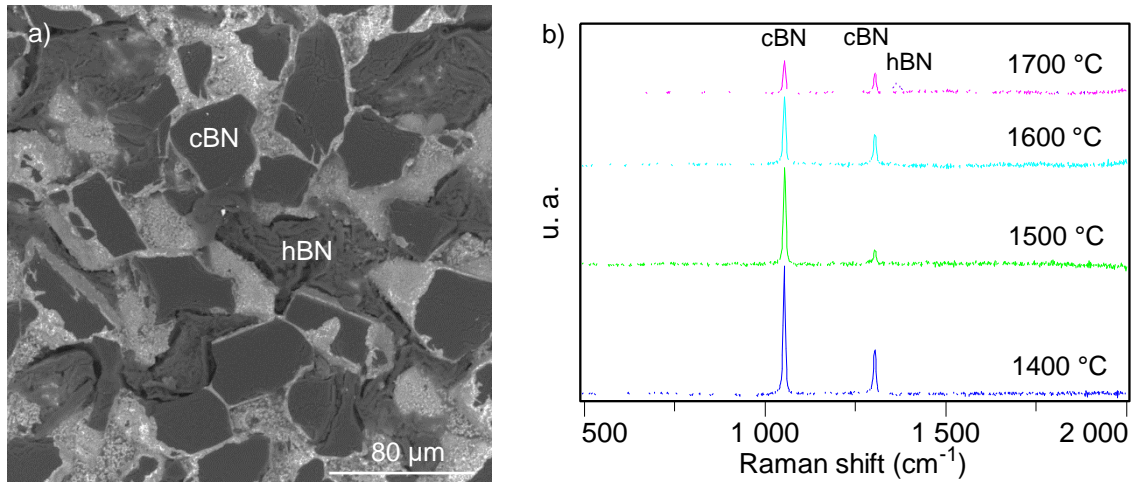
Figure 14- SEM image (a) of sample 2 sintered at 1600 ºC, and (b) comparison of the Raman spectrums from individual BN grains of samples sintered at 1400 – to 1700 ºC.

A microstructure comparison from the samples sintered at 1400 – 1700 ºC is shown in Figure 15, along with an EDS elemental mapping for Ti, N and B. No relevant heterogeneities are found in the SEM images, meaning it was obtained a good distribution of the powders from the mechanical mixture. The microstructure of 1400 ºC sample show some discontinuities of BN grains, indicating a low adhesion of the grains to the matrix, and the presence of some porosity in the matrix. The EDS detection of Ti, B and Ni was used to identify the TiCN, BN and Ni particles, respectively. Despite B being a light element, which causes a great degree of uncertainty about its mapping, the results align reasonably well with the coarser particles that were previously known to be BN. The binder is composed of TiCN and Ni, where for sample 1400 ºC the Ni phase appears to still process high viscosity during sintering and is not well spread around the BN grains, while at temperatures of 1600 ºC and 1700ºC there was a significant improvement in the spreading of that viscous phase.

In a closer observation of the microstructure of sample sintered at 1700 ºC, and considering the phases detected in the XRD profile of Figure 12 and the elemental distribution of the EDS mapping in Figure 15, each phase observed in SEM image of Figure 15 at 1700 ºC can be identified as follows: the brighter white may correspond to Ni_3B, light grey to TiCN, dark grey to TiB_2, and the darkest one to BN.
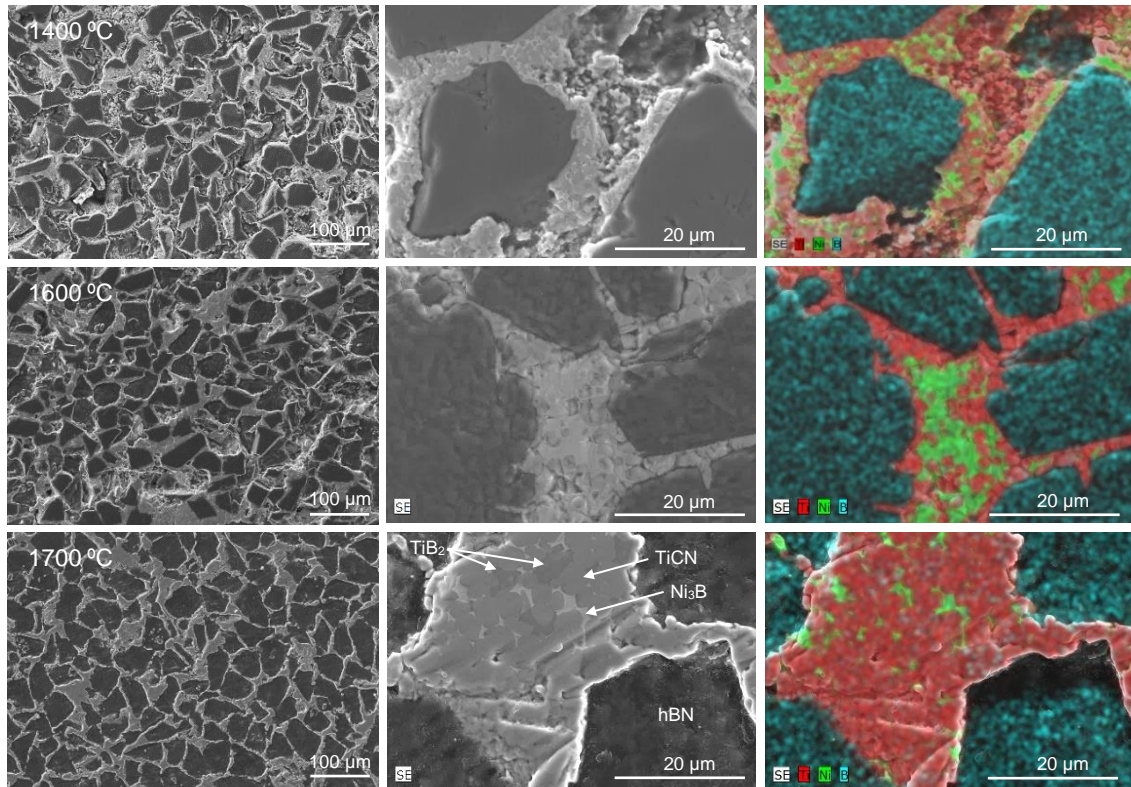
Figure 15- SEM and EDX of the samples from the cBN510-Ti(C,N)-Ni composition sintered at 1400 – 1700 ºC.

4.Conclusion

In this work it was studied the sintering of a cBN-TiCN based composite with addition of Ni, and its effect on the sintering behavior, densification, microstructure, and structural phases. The addition of Ni increased the shrinkage rate of the material, but it was only possible obtain great densification at the temperature of 1700 ºC where it was observed the BN transformation to hexagonal form, with indicates that no benefit was obtained by employing fast heating rates to sinter the material. The BN phase transformation was verified to occur even at temperatures as low as 1400 ºC but the majority occur at 1700 ºC, resulting in the near complete removal of the cubic form from the system. The Ni phase did not change the phase transformation to lower or higher temperatures but accelerated the phase transformation. It was experimentally confirmed the formation of the crystallographic phases predicted to form by thermodynamic calculations in these systems: BN, TiCN, TiB$_2$ and Ni$_3$B, demonstration the utility of using these tools in materials study.

References

[1]   L.F. Dobrzhinetskaya, R. Wirth, J. Yang, H.W. Green, I.D. Hutcheon, P.K. Weber, E.S. Grew, Qingsongite, natural cubic boron nitride: The first boron mineral from the Earth's mantle, Am. Mineral. 99 (2014) 764–772. https://doi.org/10.2138/am.2014.4714.

[2]   S. Rudolph, Boron nitride (BN), Am. Ceram. Soc. Bull. 79 (2000) 50.

[3]   L. Vel, G. Demazeau, J. Etourneau, Cubic boron nitride: synthesis, physicochemical properties and applications, Mater. Sci. Eng. B. 10 (1991) 149–164. https://doi.org/10.1016/0921-5107(91)90121-B.

[4] M.I. Petrescu, M.G. Balint, Structure and properties modifications in boron nitride. Part I: Direct polymorphic transformations mechanisms, UPB Sci. Bull. Ser. B Chem. Mater. Sci. 69 (2007) 35–42. https://www.researchgate.net/publication/261853742_Structure_and_properties_modificatio ns_in_boron_nitride_Part_I_Direct_polymorphic_transformations_mechanisms (accessed August 26, 2021).

[5] V.L. Solozhenko, V.Z. Turkevich, W.B. Holzapfel, Refined Phase Diagram of Boron Nitride, J. Phys. Chem. B. 103 (1999) 2903–2905. https://doi.org/10.1021/jp984682c.

[6] N. Izyumskaya, D.O. Demchenko, S. Das, Ü. Özgür, V. Avrutin, H. Morkoç, Recent Development of Boron Nitride towards Electronic Applications, Adv. Electron. Mater. 3 (2017) 1600485. https://doi.org/10.1002/aelm.201600485.

[7] Y. Le Godec, A. Courac, V.L. Solozhenko, High-pressure synthesis of superhard and ultrahard materials, J. Appl. Phys. 126 (2019) 151102. https://doi.org/10.1063/1.5111321.

[8] G.E. Spriggs, 13.5 Properties of diamond and cubic boron nitride, in: Powder Metall. Data. Refract. Hard Intermet. Mater., Springer-Verlag, 2005: pp. 118–139. https://doi.org/10.1007/10858641_7.

[9] S.N. Monteiro, A.L.D. Skury, M.G. De Azevedo, G.S. Bobrovnitchii, Cubic boron nitride competing with diamond as a superhard engineering material - An overview, J. Mater. Res. Technol. 2 (2013) 68–74. https://doi.org/10.1016/j.jmrt.2013.03.004.

[10] C.J.H. Wort, Applications for superhard and ultra-hard materials, in: Microstruct. Correl. Hard, Superhard, Ultrahard Mater., Springer, Cham, 2016: pp. 25–74. https://doi.org/10.1007/978-3-319-29291-5_2.

[11] R. Riedel, Handbook of Ceramic Hard Materials, Wiley, 2000. https://doi.org/10.1002/9783527618217.

[12] K. V. Slipchenko, D.A. Stratiichuk, V.Z. Turkevich, N.M. Bilyavyna, V.M. Bushlya, J.E. Ståhl, Sintering of BN Based Composites with ZrC and Al under High Temperatures and Pressures, J. Superhard Mater. 42 (2020) 229–234. https://doi.org/10.3103/S1063457620040103.

[13] Y. Fan, J. Fan, C. Wang, Detailing interfacial reaction layer products between cubic boron nitride and Cu-Sn-Ti active filler metal, J. Mater. Sci. Technol. 68 (2021) 35–39. https://doi.org/10.1016/j.jmst.2020.08.014.

[14] L. Li, Y. Zhao, K. Sun, H. Ji, D. Feng, Z. Li, Composition, microstructure and mechanical properties of cBN-based composites sintered with AlN- Al- Ni binder, Ceram. Int. 44 (2018) 16915–16922. https://doi.org/10.1016/j.ceramint.2018.06.130.

[15] Y. Jia, Electrode material effect on electrical discharge machining PcBN cutting tool processing, Adv. Mater. Res. 399–401 (2012) 1667–1671. https://doi.org/10.4028/www.scientific.net/AMR.399-401.1667.

[16] M.W. Cook, P.K. Bossom, Trends and recent developments in the material manufacture and cutting tool application of polycrystalline diamond and polycrystalline cubic boron nitride, Int. J. Refract. Met. Hard Mater. 18 (2000) 147–152. https://doi.org/10.1016/S0263-4368(00)00015-9.

[17] A. McKie, J. Winzer, I. Sigalas, M. Herrmann, L. Weiler, J. Rödel, N. Can, Mechanical properties of cBN-Al composite materials, Ceram. Int. 37 (2011) 1–8. https://doi.org/10.1016/j.ceramint.2010.07.034.

[18] G. Will, G. Nover, J. Von Der Gönna, New experimental results on the phase diagram of boron nitride, J. Solid State Chem. 154 (2000) 280–285. https://doi.org/10.1006/jssc.2000.8850.

[19] D. M. P. Mingos, High Performance Non-Oxide Ceramics II, 2002.

[20] J.H. Edgar, Properties of group III nitrides, INSPEC, Institution of Electrical Engineers, 1994. https://books.google.com/books/about/Properties_of_Group_III_Nitrides.html?hl=pt-PT&id=3bZRAAAAMAAJ (accessed June 1, 2022).

[21] H. Sachdev, R. Haubner, H. Nöth, B. Lux, Investigation of the c-BN/h-BN phase transformation at normal pressure, Diam. Relat. Mater. 6 (1997) 286–292. https://doi.org/10.1016/s0925-9635(96)00697-8.

[22] J. Zhang, R. Tu, T. Goto, Cubic boron nitride- containing ceramic matrix composites for cutting tools, in: I.M. Low (Ed.), Adv. Ceram. Matrix Compos., Woodhead Publishing Limited, 2014: pp. 570–586. https://www.sciencedirect.com/book/9780857091208/advances-in-ceramic-matrix-composites (accessed August 26, 2021).

[23] T. Sekine, T. Kobayashi, H. Nameki, Effects of deviatoric stress and radial strain on the shock-induced diffusionless transformation in boron nitride, J. Appl. Phys. 81 (1997) 527–529. https://doi.org/10.1063/1.364132.

[24] J. Huang, Y.T. Zhu, Advances in the synthesis and characterization of boron nitride, Diffus. Defect Data. Pt A Defect Diffus. Forum. 186–187 (2000) 1–32. https://doi.org/10.4028/www.scientific.net/ddf.186-187.1.

[25] J.T. Cahill, W.L. Du Frane, C.K. Sio, G.C.S. King, J.C. Soderlind, R. Lu, M.A. Worsley, J.D. Kuntz, Transformation of boron nitride from cubic to hexagonal under 1-atm helium, Diam. Relat. Mater. 109 (2020) 108078. https://doi.org/10.1016/j.diamond.2020.108078.

[26] V.L. Solozhenko, O.O. Kurakevych, Y. Le Godec, Creation of nanostuctures by extreme conditions: High-pressure synthesis of ultrahard nanocrystalline cubic boron nitride, Adv. Mater. 24 (2012) 1540–1544. https://doi.org/10.1002/adma.201104361.

[27] N. Tan, C.J. Liu, Y.J. Li, Y.W. Dou, H.K. Wang, H. Ma, Z.L. Kou, D.W. He, Characterization of polycrystalline cBN compacts sintered without any additives, EPJ Appl. Phys. 53 (2011). https://doi.org/10.1051/epjap/2010100321.

[28] Y. Yuan, X. Cheng, R. Chang, T. Li, J. Zang, Y. Wang, Y. Yu, J. Lu, X. Xu, Reactive sintering cBN-Ti-Al composites by spark plasma sintering, Diam. Relat. Mater. 69 (2016) 138–143. https://doi.org/10.1016/j.diamond.2016.08.009.

[29] P. Klimczyk, P. Wyżga, J. Cyboroń, J. Laszkiewicz-Łukasik, M. Podsiadło, S. Cygan, L. Jaworska, Phase stability and mechanical properties of Al2O3-cBN composites prepared via spark plasma sintering, Diam. Relat. Mater. 104 (2020). https://doi.org/10.1016/j.diamond.2020.107762.

[30] O. Guillon, J. Gonzalez-Julian, B. Dargatz, T. Kessel, G. Schierning, J. Räthel, M. Herrmann, Field-assisted sintering technology/spark plasma sintering: Mechanisms, materials, and technology developments, Adv. Eng. Mater. 16 (2014) 830–849. https://doi.org/10.1002/adem.201300409.

[31] P. Cavaliere, B. Sadeghi, A. Shabani, Spark Plasma Sintering: Process Fundamentals, in: Spark Plasma Sinter. Mater., Springer, Cham, 2019: pp. 3–20. https://doi.org/10.1007/978-3-030-05327-7_1.

[32] M. Kitiwan, A. Ito, J. Zhang, T. Goto, Densification and mechanical properties of cBN-TiN-TiB2 composites prepared by spark plasma sintering of SiO2-coated cBN powder, J. Eur. Ceram. Soc. 34 (2014) 3619–3626. https://doi.org/10.1016/j.jeurceramsoc.2014.05.018.

[33] J. Zhang, R. Tu, T. Goto, Preparation of Ni-cBN composites by spark plasma sintering, J. Japan Soc. Powder Powder Metall. 59 (2012) 410–271. https://doi.org/10.2497/jjspm.59.410.

[34] M.A. Umer, P.H. Sub, D.J. Lee, H.J. Ryu, S.H. Hong, Polycrystalline cubic boron nitride sintered compacts prepared from nanocrystalline TiN coated cBN powder, Mater. Sci. Eng. A. 552 (2012) 151–156. https://doi.org/10.1016/j.msea.2012.05.024.

[35] ASTM C20-00, Standard Test Methods for Apparent Porosity , Water Absorption , Apparent Specific Gravity , and Bulk Density of Burned Refractory Brick and Shapes by Boiling Water, Am. Soc. Test. Mater. 00 (2015) 1–3. https://doi.org/10.1520/C0020-00R10.2.

[36] E. Benko, J.S. Stanislaw, B. Królicka, A. Wyczesany, T.L. Barr, CBN-TiN, cBN-TiC composites: Chemical equilibria, microstructure and hardness mechanical investigations, Diam. Relat. Mater. 8 (1999) 1838–1846. https://doi.org/10.1016/S0925-9635(99)00131-4.

[37] E. Benko, P. Klimczyk, J. Morgiel, A. Włochowicz, T.L. Barr, Electron microscopy investigations of the cBN-Ti compound composites, in: Mater. Chem. Phys., Elsevier, 2003: pp. 336–340. https://doi.org/10.1016/S0254-0584(03)00016-6.

[38] E. Piskorska, E. Benko, I.N. Demchenko, A. Benko, E. Welter, T.L. Barr, X-ray absorption studies of the c-BN -Ti based composites, (n.d.) 6–7.

[39] J. Zhang, R. Tu, T. Goto, Preparation of SiAlON-cBN composites using Ni nanoparticle precipitated cBN powders, Key Eng. Mater. 508 (2012) 17–20. https://doi.org/10.4028/www.scientific.net/KEM.508.17.

[40] B. Hering, A.K. Wolfrum, T. Gestrich, M. Herrmann, Thermal stability of TiN coated cubic boron nitride powder, Materials (Basel). 14 (2021). https://doi.org/10.3390/ma14071642.

[41] L. Yu, B. Gao, Z. Chen, C. Sun, D. Cui, C. Wang, Q. Wang, M. Jiang, In situ FTIR investigation on phase transformations in BN nanoparticles, Chinese Sci. Bull. 50 (2005) 2827–2831. https://doi.org/10.1360/982005-570.

Acknowledgments

Attachments

In Figure 16 is shown the individual shrinkage and shrinkage rate curves of composition 2 sintered at 1400, 1500 and 1600 ºC. In all three cases the behavior is the same, variating the total shrinkage in function of increasing temperature.

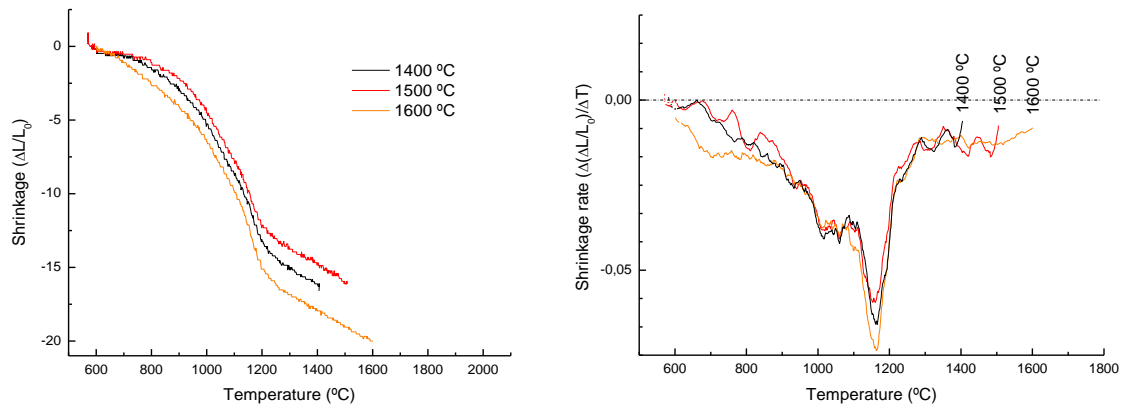a)   b)

Figure 16- Shrinkage (a) and shrinkage rate (b) of the samples from composition 2 sintered at 1400 – 1600 ºC and 60 MPa in function of temperature during heating stage.